LI-ION BATTERY MATERIALS THEORY AND COMPUTATION TO GUIDE AND INTERPRET EXPERIMENTS

by

Marc M. E. Cormier

Submitted in partial fulfillment of the requirements
for the degree of Doctor of Philosophy

at

Dalhousie University
Halifax, Nova Scotia
September 2022

This thesis is dedicated to my parents, Marcel and Lise, whose unconditional love and support allowed me to return to academic studies.

Table of Contents

List of Tables

List of Figures

Abstract

Li-ion batteries are enabling electrification; cell energy densities, lifetimes and cost render grid energy storage solutions and personal and commercial electric modes of transportation economically and practically feasible. However, exponential market growth demands cheaper, longer lasting, more energy dense, and safer Li-ion cells. The work presented in this thesis rests at the intersection of theory, computation, and experiment; properties of Li-ion battery positive electrode materials were computed from first-principles and compared to experimental results, phenomenological equations were fit to measurement, and software was developed to analyze experimental data.

The first part of this thesis shows that within the GGA+U formalism, the calculated structural, electronic, and electrochemical properties of relevant materials for state-of-the-art positive electrodes, depend on the choice of U to a greater extent than previously recognized. In some cases, an incorrect electronic structure is predicted. These findings suggest that U should be chosen with care, and in some cases the GGA+U formalism may not be appropriate.

The second part of this thesis demonstrates how individual substituents influence electrochemical and thermal properties of Ni-rich positive electrode materials. Furthermore, a reinvented approach for Li chemical diffusion measurements, bridging theory and measurement, is developed and used to show how omitting Co altogether from Ni-rich positive electrode materials worsens rate capability. These results highlight intrinsic challenges in Li-ion battery material optimization and offer practical considerations for designing high energy-density positive electrode materials.

The final part of this thesis presents analysis software developed for experimental data. Two software suites were developed; the first enables automated yet interactive analyses of Li chemical diffusion measurements, providing users with export and fitting flexibility, and the second provides a user-interface for exploring data collected from different cyclers and automatically fitting differential capacity curves to reference data. These tools have saved many days of otherwise manual analysis.

List of Abbreviations and Symbols Used

$\%\mathrm{Ni_{Li}}$	Percentage of Ni atoms in the Li layers.
fcc	Face-centered cubic.
D_c	Li chemical diffusion coefficient.
E_{XC}	Exchange and correlation energy.
G_p	Gibbs free energy of the positive electrode material.
IR	Current times resistance; Ohmic-type contribution to voltage.
I	Electric current.
R_{eff}	Effective internal resistance of the electrochemical cell.
U	Parameter value in GGA+U in eV.
V	Voltage.
Z_I	Nuclear charge.
Γ	Gamma point, $\mathbf{k} = (0, 0, 0)$.
Ψ	Many electron wavefunction.
ϵ_{XC}	Exchange and correlation energy density.
$\hat{H}$	The Hamiltonian.
$\mathbf{k}$	Wavevector.
$\mathbf{r}$	Position vector in 3-dimensional real-space.
μ_B	Bohr magneton.
μ_p	Chemical potential of Li in the positive electrode material.
μ_{Li}	Chemical potential of Li in Li metal.
ψ	Single electron wavefunction.
ε_f	Fermi level.
dQ/dV	Differential capacity.
dV/dQ	Differential voltage.

eV	Electron-volt.
e	Electron charge.
k_B	Boltzmann constant.
m	Magnetic moment.
$n(\mathbf{r})$	Electron charge density.
a.u.	Atommic units.
AMID	Atlung method for intercalant diffusion.
API	Application programming interface.
B86a	Exchange and correlation functional of Becke.
COHP	Crystal orbital Hamilton population.
DC	Discharge capacity.
DFT	Density Functional Theory.
DOS	Density of states.
EIS	Electrochemical impedance spectroscopy.
FLAPW	Full-potential linearized augmented plane-waves.
FM	Ferromagnetic.
GGA	Generalized Gradient Approximation.
GITT	Galvanostatic intermittent titration technique.
GUI	Graphical user interface.
HS	High-spin.
IRC	Irreversible capacity.
LCAO	Linear combination of atomic orbitals.
LCO	$LiCoO_2$.
LDA	Local Density Approximation.
LMO	$LiMn_2O_4$.
LNO	$LiNiO_2$.
LS	Low-spin.
LSDA	Local Spin-Density Approximation.
NCA	$LiNi_{1-x-y}Co_xAl_yO_2$.

NMC	$LiNi_{1-x-y}Mn_xCo_yO_2$.
OCV	Open-circuit voltage.
PAW	Projector augmented-waves.
PBE	Exchange and correlation functional of Perdew, Burke, and Ernzerhof.
PC	Polycrystalline.
pCOHP	Projected crystal orbital Hamilton population.
pDOS	Projected density of states.
QMC	Quantum Monte Carlo.
RPA	Random Phase Approximation.
SC	Single crystalline.
SCAN	Strongly Constrained and Appropriately-Normed.
SEI	Solid-electrolyte interphase.
SEM	Scanning Electron Miscroscope.
TM	transition metal.
TMO	Transition metal oxide.
TSH	Tetrahedral site hop.
UEG	Uniform electron gas.
UHPC	Ultra-high precision coulometry.
VASP	Vienna Ab-initio Simulation Package.
XRD	X-ray diffraction.

Acknowledgements

There are a number of people who either made this thesis possible, or facilitated it. To all of them I express my sincere gratitude.

To my wife, Hannah, whose love, patience, and support helped keep my spirits up while writing, and to my son, Amos, whose smile and laughter can turn anyone's day around.

To my advisor, Prof. Jeff Dahn, from whom I have learned incredibly, and will no doubt continue to learn from for a long time. Thank you in particular for taking me on as a student. Roughneck turned physicist; full circle from oil and gas to Li-ion batteries. I owe that to you.

To my committee members for their time and feedback.

To the entire department of Physics and Atmospheric Science, where I had the privilege of having many mentors and friends. It has been a long road since undergraduate studies, one filled with memories that will forever be cherished.

Last but certainly not least, to all collaborators, you made this thesis and other research possible. Dr. Hongyang Li, Dr. Ning Zhang, Dr. Aaron Liu, Dr. Nutthaphon Phattharasupakun, Yulong Liu, Eniko Zsoldos, Mitch Ball, and Erin Lyle all contributed, in one way or another, to the research presented in this thesis. Dr. David Hall and Eric Logan were experimental collaborators for research that was not presented in this thesis, but to whom I am also grateful. Laurent Molino and John Corsten both contributed as undergraduate students. I learned a great deal from being a mentor, so thank you for your patience and hard work.

Chapter 1

Introduction

Li-ion cells are everywhere; in obvious places like phones, computers, and now homes and cars, but also in perhaps unexpected places like medical devices and automated tools used in space. Li-ion cells constitute a high density energy storage system enabling the rapid emergence of techno-economic systems that are changing the world; from storing renewable energy in remote locations and mitigating blackouts to helping the world heal from a deadly addiction to fossil fuels by transitioning to electric modes of transportation. To deny the importance of Li-ion cells is to deny natural selection in Darwin's theory of evolution.

Despite already widespread adoption and a rich history, the need to improve Li-ion cells is pressing: low-cost, non-toxic, long-lasting, and safe Li-ion cells are needed to expedite adoption in global markets. The work presented in this thesis uses theory and computation within the context of experimental measurements to inform the design of Li-ion cell positive electrode materials. Chapter 2 provides the necessary electrochemical background to understand how Li-ion cells operate. Chapter 3 covers the theoretical basis of density functional theory (DFT) — the computational formalism used in Chapters 4 and 5. Results are then divided into three parts: Chapter 4 aims to provide a better understanding of particular approximations made within the computational formalism most commonly used for Li-ion cell positive electrode materials; Chapter 5 demonstrates challenges in Li-ion cell positive electrode optimizations, wherein dispensing of Co is the subject; and Chapter 6 provides an overview of software that was developed to enable and expedite analysis of experimental data. Lastly, Chapter 7 offers a summary of Chapters 4, 5, and 6 and discusses potential avenues for future work.

The advent of density functional theory (DFT) as a first-principles computational method created an explosion of possibilities in computational physics, chemistry, and materials science. The study of positive electrode materials for Li-ion batteries has

certainly benefited from that momentum. However, first-principles computations in general require approximations. In Li-ion cells, positive electrode materials often contain transition metals (TM) with partially filled $3d$ electron shells which require special treatment. The most computationally efficient way to treat TM $3d$ electrons is with the GGA+U method, but at the expense of the arbitrary choice of the parameter U. Material properties can be sensitive to the choice of U, and without appropriate motivation, results may be questionable. Chapter 4 presents a detailed analysis of structural, electronic, and electrochemical properties for three representative Li-ion cell positive electrode materials: $LiNiO_2$ (LNO), $LiCoO_2$ (LCO), and $LiMn_2O_4$ (LMO), in both their lithiated and de-lithiated states. Changes to the electronic structures are directly correlated to structural and electrochemical changes. Results suggests that the choice of U for Ni in LNO may not be so sensitive, however, the electronic structure of LMO is sensitive to the choice of U. It is further suggested that GGA+U may not be appropriate at all for Co in layered oxides. The hope is that the results of Chapter 4 will heighten awareness on the choice of U, and the GGA+U method in general, especially as it applies to TM-containing oxides.

Optimizing Li-ion cell positive electrode materials is not simply a search for the most energy-dense, safest, and longest-lasting material; material cost and sourcing stability are perhaps even more important factors. Any particular Li-ion cell application necessitates cross-examination of each aforementioned factors so that the best-suited material can be chosen. For example, grid-energy storage is generally not size-constrained, thus does not require high energy density cells, but has very large capacity, thus requires cells with excellent thermal stability. On the other hand, long-range electric vehicles require high energy density Li-ion cells due to the constrained volume into which the battery pack can fit. The challenge, however, is that altering the composition of Li-ion cell positive electrode materials to optimize for one factor, can inadvertently influence another.

Chapter 5 demonstrates this point by considering the role of Co in Ni-rich layered oxide positive electrode materials. Eliminating Co would reduce and stabilize costs in these materials. Computation, theory, and experiment are paired to offer atomistic, phenomenological, and experimental interpretations on the role of Co. First,

computational results are used to interpret electrochemical and thermal stability measurements, suggesting that Co brings little-to-no-benefit in Ni-rich positive electrode materials. Second, the Atlung Method for Intercalant Diffusion (AMID) is developed to measure Li-ion chemical diffusion, which is used to investigate how the presence of Co influences Li kinetics. In this case, Co is found to be beneficial. The opposing conclusions within this Chapter highlight material optimization difficulties in Li-ion cells.

Chapter 6 describes software that was developed to address specific challenges with experimental data. The first of the two components, called the AMID application programming interface (API), was critical to the development of the AMID by enabling analysis of measured data in minutes instead of hours. The second component began as a flexible data file parser with functions to address specific challenges in visualizing certain experimental data, but evolved to be the back-bone of a new tool to analyze degradation in Li-ion cells. Both of these software components are the result of an attempt to, as a computationalist, be helpful in an experimental group. They illustrate that even without a clear end goal, doing our best will lead to good things.

Hopefully this thesis primarily inspires the joining of forces between computation and experiment. Working closely to many talented researchers was a privilege and the most rewarding part of the work. Any reader is encouraged to seek out collaborators, in one way or another.

Chapter 2

Li-ion cells

Fundamentally, all Li-ion cells are constructed the same way, but can be packaged differently. The essential ingredients of Li-ion cells can be divided into two categories: active and inactive materials. The active materials participate in electrochemical reactions that store or deliver energy; they are the positive and negative electrodes. The inactive materials do not participate in electrochemical reactions but without them the cell would not function. The electrolyte allows Li ions to be tranferred between the two electrodes; the binder holds electrode particles together and facilitates the mechanical application of the electrode slurry onto current collectors (aluminum and copper for positive and negative electrodes, respectively); the conductive agent carries electrons from the electrode particles to the current collectors and is necessary because not all electrode particles are in contact with the current collectors; the separator is a porous solid membrane open to the electrolyte but physically separates the positive and negative electrode to prevent internal short circuit. Material optimization for both active and inactive materials is possible, but this thesis examines fundamental aspects of positive electrode materials.

2.1 Cell construction

Figure 2.1 depicts the basic construction of a Li-ion cell. In modern cells, the positive electrode is composed of a transition metal (TM)-containing oxide or phosphate host structure with intercalating Li ions. Primary particles with a single crystalline orientation can be agglomerated into secondary particles — a polycrystalline (PC) material, or can be separated from other primary particles — a single crystalline (SC) material. The scanning electron microscope (SEM) image in Figure 2.1 shows a PC material. Within the positive electrode, Li atoms occupy the center of the green octahedra, TM atoms occupy the center of the grey octahedra, and O atoms are represented by red spheres.

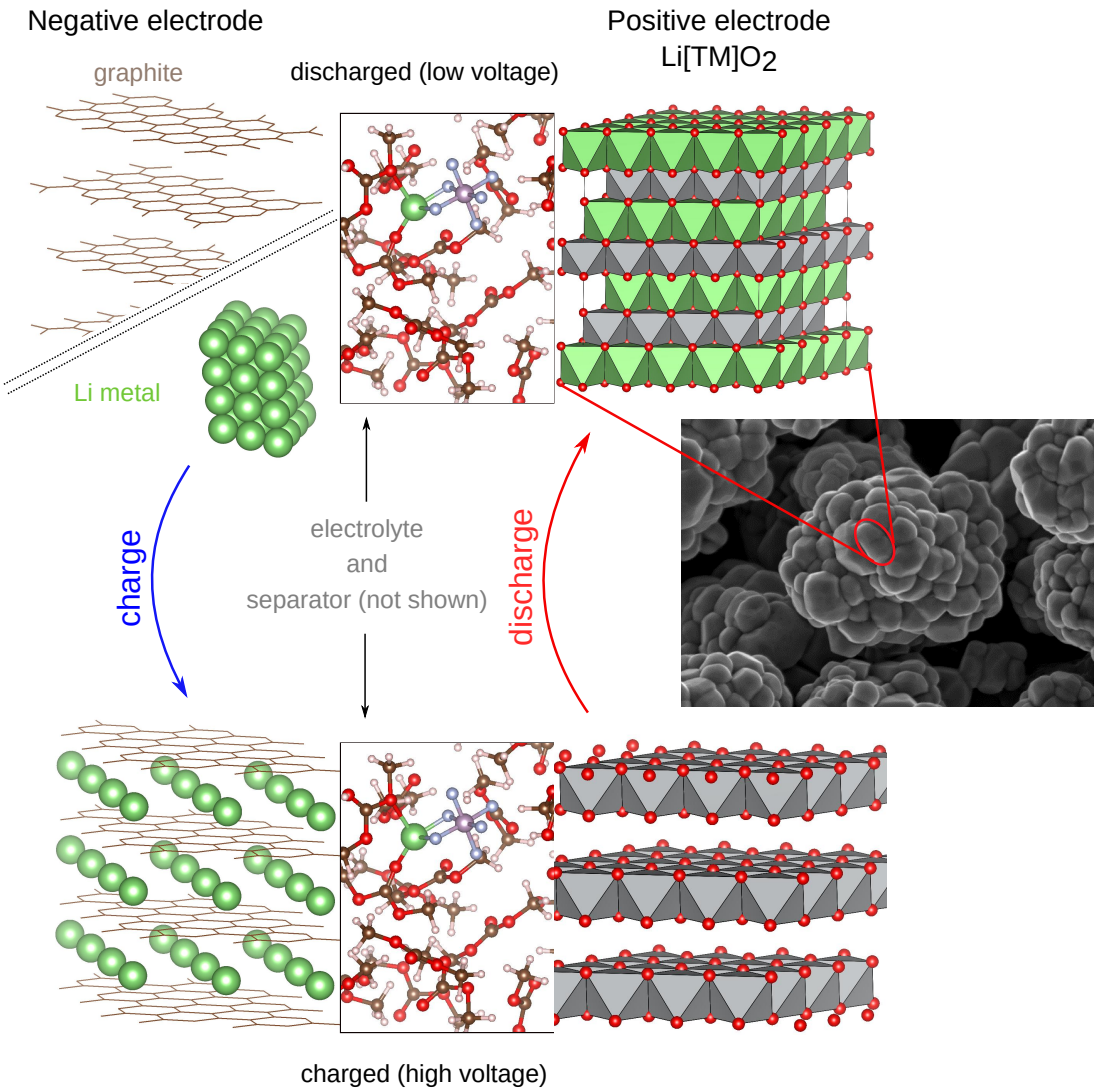

Figure 2.1: Depiction of a Li-ion or Li metal cell. The scanning electron microscope image of a typical TM oxide positive electrode material shows larger secondary particles composed of smaller primary particles that are single crystals. The layered structures on the right hand side correspond to the positive electrode material; the electrolyte is depicted in the center; and the negative electrode — graphite and Li metal, is depicted on the left hand side. Li atoms are represented by green spheres or occupy the center of the green octahedra, TM atoms occupy the center of the grey octahedra, O atoms are represented by red spheres, C atoms by brown spheres or occupy the vertices of hexagons, and H by beige spheres. The separator is omitted from the electrolyte depiction.

Some common positive electrode chemistries include $LiFePO_4$, $LiCoO_2$ (LCO), $LiNi_{1-x-y}Mn_xCo_yO_2$ (NMC), and $LiNi_{1-x-y}Co_xAl_yO_2$ (NCA). All of these materials are synthesized fully lithiated so that Li ions are removed during charge, storing energy, and re-inserted during discharge, delivering energy. In the ideal case, a fully charged positive electrode material would have no remaining Li, while a fully discharged material would be completely filled with Li.

By far the most common negative electrode is graphite due to its low voltage and its ease of passivation by reduced electrolyte species on its surface, forming the so-called solid-electrolyte interphase (SEI). [74, 84, 52, 87] Li-metal and "anode-free" cells are also possible, where the graphite negative electrode is either replaced by Li metal or is simply removed, leaving the copper current collector as the negative electrode. In both of these cases, Li is plated and stripped at the negative side during charge and discharge, respectively. Li metal cells, also referred to as "half-cells", are commonly used in materials development projects because they are easier to build in a laboratory setting compared to Li-ion cells with graphite negative electrodes. In Figure 2.1, C atoms occupy sites at the vertices of each hexagon. Li atoms in Li metal are represented by green spheres.

The electrolyte is generally composed of a mixture of organic carbonates (it is common to combine linear and cyclic carbonates such as ethylene carbonate — cyclic, and dimethyl carbonate — linear) and a Li salt, such as lithium hexafluorophosphate ($LiPF_6$), for example. The electrolyte is ionically conductive, enabling Li transport between electrodes, but electrically insulating, forcing electrons through an external circuit to maintain charge balance between electrodes as Li ions are transferred. The depiction of Figure 2.1 shows an $LiPF_6$ salt molecule (Li: green, P: light purple, F: light blue) coordinated within dimethyl carbonate (O: red, C: brown, H: beige).

2.2 Electrochemical fundamentals

Interestingly, Li-ion cells deliver energy by operating in fine thermodynamic balance; energy is required to remove Li ions from the positive electrode material, leaving a structure that is less thermodynamically stable than its fully lithiated counterpart. The energy required to remove Li ions from the positive electrode material is determined by both its structure and composition. The potential difference (voltage)

between the positive and negative electrodes in a Li-ion cell arises due to the different Li chemical potentials (energies) in each electrode. For example, Li ions are more tightly bound in LCO compared to graphite, thus they experience a difference in Li chemical potentials between the electrodes which leads to a potential difference, or voltage. The voltage for a half-cell (Li metal negative electrode) is given by $V = (\mu_{Li} - \mu_p)/e$, where μ_{Li} is the chemical potential of Li in Li metal, which is constant, μ_p is the chemical potential of Li in the positive electrode, and e is the electron charge. This expression is specific to the case of one electron electrochemical reactions, such as with Li, but in general there could be more than one electron involved per intercalant, in which case the denominator would be ne, where n is the number of electrons involved in the electrochemical reaction.

The Li chemical potential is a result of thermodynamics; the change in Gibbs free energy (thermodynamic potential) of the positive electrode, G_p, with respect to the change in Li concentration gives the chemical potential: $dG_p/dn = \mu_p$. In this way, the voltage of an electrochemical cell can be understood as the result of a change in thermodynamic potential which includes internal energy, entropic, and vibrational contributions. For a half cell, the potential versus composition curve corresponds to the Gibbs free energy landscape of Li in the positive electrode as the Li content changes. The number of Li ions extracted per gram of material from the positive electrode at a particular voltage is the specific capacity; amount of charge (mAh) per unit mass (g). Figure 2.2 (a) shows the voltage versus specific capacity curve as Li is extracted from $LiNiO_2$ in a half cell. The charge curve is shown in blue, the discharge curve in red, and the equilibrium curve is shown by a black dotted line. The voltage separation between the charge and discharge curves is $\Delta V = 2IR_{eff}$, where I is the current through the external circuit and R_{eff} is the effective internal resistance of the cell. The equilibrium curve can only be reached in the limit of infinitely slow current or zero resistance which are both electrochemically impossible. The equilibrium curve shown is not the "true" curve; the discharge curve achieves less capacity that the charge curve due to inaccessible Li, which skews the voltage average and smoothes out the equilibrium curve. The 'true" equilibrium curve should have much sharper features. The inevitable effects of dynamics will be discussed shortly.

The shape of a voltage-composition curve indicates thermodynamic characteristics of the electrode material as Li ions and electrons are removed or inserted. For example, a well-defined voltage plateau, where the voltage remains constant as the Li content changes, generally indicates two-phase coexistence; constant voltage corresponds to constant Li chemical potential, μ_p, which in turns means constant dG_p/dn. A constant change in Gibbs free energy means a thermodynamic reaction where the initial and final states each remain the same as the inital state is converted to the final state; a phase transition. Conversely, regions of the voltage-composition curve that have a constant slope generally correspond to solid solutions where there is no well-defined structure in the Li sub-lattice within the electrode material so the voltage increases incrementally as Li ions are removed or inserted. Features in voltage-composition curves are more clearly seen by plotting the differential capacity — the inverse derivative, dQ/dV, versus voltage. Figure 2.2 (b) shows dQ/dV versus voltage for the charge and discharge ($-dQ/dV$) curves of panel (a). Each plateau in the voltage-composition curve shows up as peaks in dQ/dV. This is a useful tool for comparing changes in electrochemical behaviour between different materials.

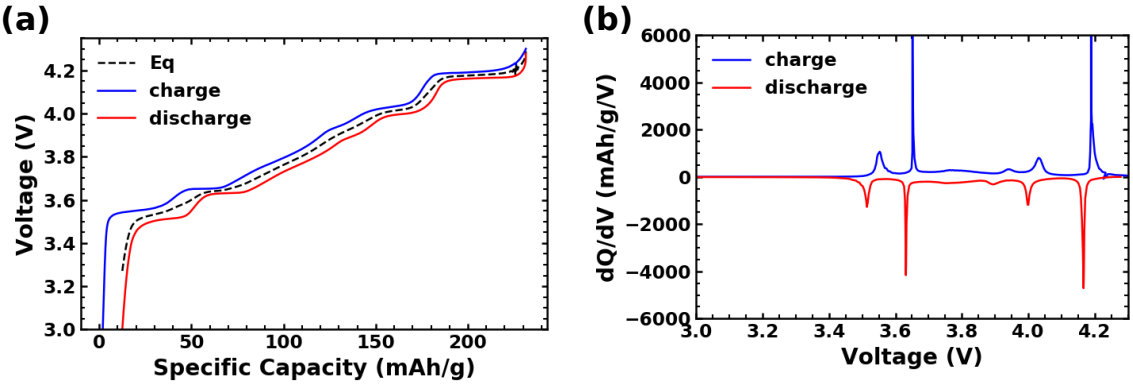

Figure 2.2: (a) Example voltage-composition charge (blue), discharge (red) and equilibrium (black dashed) curves for $LiNiO_2$. (b) Corresponding differential capacity (dQ/dV) curves for the charge (blue) and discharge (red) parts of the cycle. Note that $-dQ/dV$ is plotted for the discharge.

To get from one electrode to the other, Li ions must travel through the electrolyte. The potential difference between electrodes drives reactions at the surface of electrode particles; during charge for example, Li ions are extracted from the surface

of positive electrode particles into the electrolyte while Li ions from the electrolyte are inserted at the surface of negative electrode particles (or deposited on the surface of Li metal). The result is a Li concentration gradient within the electrolyte, with a larger concentration of Li ions at the positive electrode and a smaller one at the negative electrode, that drives Li diffusion from one electrode to the other. Importantly, it is the Li concentration at the surface of electrode particles that determines the voltage; concentration gradients within electrode particles develop when a cell is charged or discharged sufficiently fast. In this regard, dynamic aspects of intercalants in electrode materials are also important.

Figure 2.3 illustrates how concentration gradients develop within electrode particles and how the amount of Li inserted or extracted — the capacity — is affected by faster discharge or charge. Panel (a) depicts the surface of a primary positive electrode particle. The precise structure of the surface is actively discussed in the literature, thus the depiction here is merely for the purpose of illustration. A single Li ion (the electrolyte is not shown) is shown (green sphere) to be inserted at the surface of a particle. The SEM image shows agglomerated primary particles with the surface of a single particle emphasized. Here, red spheres represent O atoms, TM atoms occupy the center of the grey octahedra, and Li atoms occupy the center of the green octahedra. If the ability for Li atoms to diffuse within the lattice is limited compared to the rate at which they are inserted at the particle surfaces, a concentration gradient will develop between the surface and the center of the particles. Figure 2.3 (b) shows the relative concentration of Li as a function of the distance from the center of a spherical particle for a slower discharge (dotted lines) and a faster discharge (solid lines). Curves shifted upwards from each other correspond to later times after the discharge began from a fully de-lithiated material. This graph has been modified from Atlung *et* al. [5]. Each pair of solid and dashed curves correspond to the same mean concentration. The faster discharge always has a larger surface concentration for the same mean concentration because Li lattice diffusion is limited. The faster discharge reaches the maximum surface concentration with only 70 percent of its available capacity while the slower discharge has less than 80 percent surface concentration for the same net capacity. It is clear that the apparent capacity of a material will be influenced by the current at which it is charged or discharged.

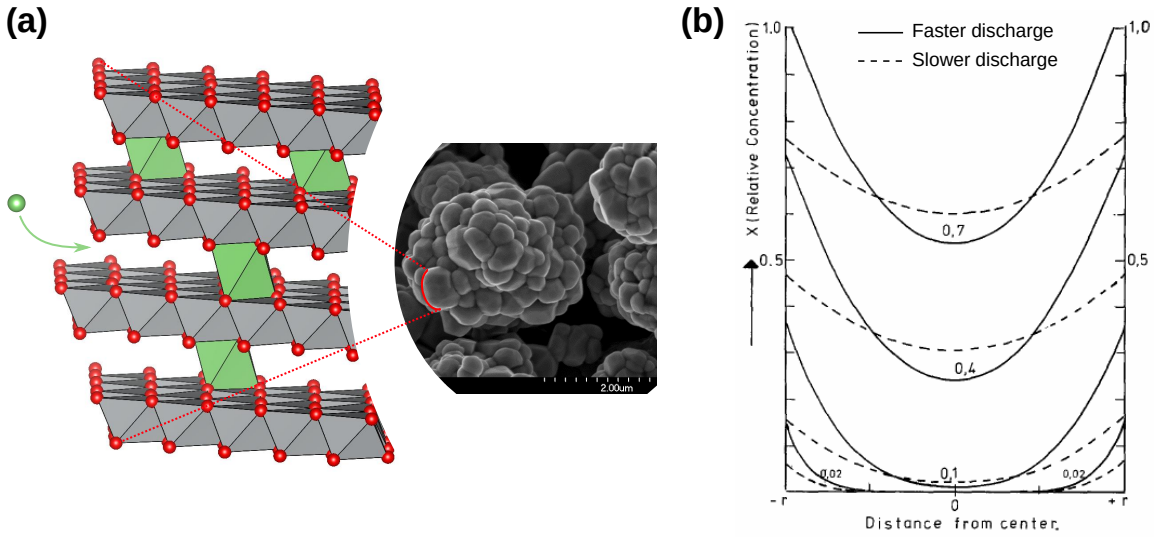

Figure 2.3: (a) Depiction of a Li ion (green sphere) being inserted at the surface of a positive electrode primary particle where other Li atoms occupy the center of the green octahedra, TM atoms occupy the center of the grey octahedra, and O atoms are represented by red spheres. The SEM image shows agglomerated primary particles with the surface of a single particle expanded in the depiction. (b) The relative Li concentration as a function of the radial distance from the center of a spherical particle. The solid curves show behaviour for a faster discharge and the dotted curve for a slower discharge. Each pair of solid and dashed curves is labelled by the mean Li concentration. This graph was modified from Atlung *et* al. [5]

The observed features of an electrochemical reaction within a Li-ion cell are due to both thermodynamics and dynamics. The thermodynamic properties of electrode materials determine the equilibrium voltage, the general features of the voltage-composition curves, and potential decomposition pathways, while dynamic properties determine how the voltage-composition curve responds to different currents. Understanding both thermodynamics and dynamics is thus important.

Chapter 4 investigates limitations of a particular formalism, GGA+U, for computations of positive electrode thermodynamics. Chapter 5 aims to answer the question "Is Co is dispensible in Ni-rich positive electrode materials" by considering changes in both thermodynamics and dynamics.

Chapter 3

Theory and computational formalism

3.1 First principles atomistic computations: Density Functional Theory

"First principles" in this case means from the fundamental laws of physics. On the atomic scale, all materials are composed of electrons and nuclei (protons and neutrons). All material properties are due to the way in which electrons interact with each other in the field of nuclei. The nature of these interactions is quantum mechanical, thus "first principles" computations involve determining properties of materials directly from the theory of quantum mechanics and Coulomb's Law.

In the absence of time-dependent processes, such as scattering for example, the general problem is to solve Schroedinger's time-independent equation for a system of N electrons in the field of M nuclei. Generally, since nuclei are at least two thousand times heavier than electrons, the electronic response to motion of nuclei will be nearly instantaneous and the solution to Schroedinger's equation can be decoupled from nuclear motion. This is called the Born-Oppenheimer [14] approximation and reduces the problem to solving:

$$\hat{H}\Psi(\mathbf{r}_1, ...\mathbf{r}_N) = E\Psi(\mathbf{r}_1, ...\mathbf{r}_N) \tag{3.1}$$

where $\hat{H}$ is the Hamiltonian describing all electron-nuclei and electron-electron interactions, $\Psi(\mathbf{r}_1, ..\mathbf{r}_N)$ is the many electron wavefunction so that $\mathbf{r}_i$ denotes the spatial coordinates of the electrons, and E is the total ground state electronic energy of the

N electrons in the field of M nuclei. The Hamiltonian, in atomic units (a.u.) is:

$$\begin{aligned}\hat{H} &= \hat{T} + \hat{V} + \hat{U} \\ &= -\sum_{i}^{N} \frac{1}{2}\nabla^2 - \sum_{i}^{N}\sum_{I}^{M} \frac{Z_I}{|\mathbf{r}_I - \mathbf{r}|} + \frac{1}{2}\sum_{i}^{N}\sum_{j}^{N} \frac{1}{|\mathbf{r}_i - \mathbf{r}_j|} \\ &= -\sum_{i}^{N} \frac{1}{2}\nabla^2 + \sum_{i}^{N} V_i + \frac{1}{2}\sum_{i}^{N}\sum_{j}^{N} \frac{1}{|\mathbf{r}_i - \mathbf{r}_j|}\end{aligned} \tag{3.2}$$

$\hat{T}$ corresponds to the kinetic energy of the electrons, $\hat{V}$ to the electron-nuclei interaction — thus $V_i = -\sum_I^M Z_I/|\mathbf{r}_I - \mathbf{r}_i|$, where Z_I is the nuclear charge, is the potential experienced by each electron due to the field of all nuclei, and $\hat{U}$ to the electron-electron interaction. Since equation 3.1 is an eigenvalue equation, the ground-state energy, E, is obtained from the expectation value of $\hat{H}$ which is given by the inner product:

$$\langle\Psi|\hat{H}|\Psi\rangle = \langle\Psi|\hat{T}|\Psi\rangle + \langle\Psi|\hat{V}|\Psi\rangle + \langle\Psi|\hat{U}|\Psi\rangle \tag{3.3}$$

To evaluate each of the three terms on the right-hand side of equation 3.3, they can be projected into real space and evaluated as integrals over spatial coordinates. In particular, the second term can be written explicitly in terms of the electron density, $n(\mathbf{r})$:

$$\begin{aligned}\langle\Psi|\hat{V}|\Psi\rangle &= \int \Psi^*(\mathbf{r}_1, ..., \mathbf{r}_N) V(\mathbf{r}_i) \Psi(\mathbf{r}_1, ..., \mathbf{r}_N) d\mathbf{r}_1 ... d\mathbf{r}_N \\ &= \int V(\mathbf{r}_i) \Psi^2(\mathbf{r}_1, ...\mathbf{r}_N) d\mathbf{r}_1 ... d\mathbf{r}_N \\ &= \int V(\mathbf{r}_i) n(\mathbf{r}_i) d\mathbf{r}_i \\ &= V_{nuc}[n]\end{aligned} \tag{3.4}$$

Since equation 3.4 is written in terms of the many-electron wavefunction, the choice of the $N-1$ coordinates over which the integral is performed is not important; the same density, $n(\mathbf{r})$ is recovered. Thus, $V(\mathbf{r}_i) \equiv V(\mathbf{r})$ is the spatially dependent nuclear potential.

Conversely, the kinetic energy and electron-electron interaction terms cannot be written explicitly in terms of the density. However, the Hartree energy associated

with the classical mutual electron repulsion can be written in terms of the density:

$$J[n] = \frac{1}{2}\int \frac{n(\mathbf{r})n(\mathbf{r}')}{|\mathbf{r}-\mathbf{r}'|}d\mathbf{r}d\mathbf{r}' \tag{3.5}$$

Thus the electron-electron interaction energy can be split into classical electrostatic repulsion and quantum mechanical exchange and correlation:

$$\langle\Psi|\hat{U}|\Psi\rangle = U = J[n] + U_{XC} \tag{3.6}$$

where U is total electron-electron interaction energy. U_{XC} is the exchange and correlation energy, and is always negative; the fermionic nature of electrons requires wavefunctions to be anti-symmetric which induces a spatial separation between same-spin electrons, thereby reducing the electrostatic repulsion. The electrostatic energy can be reduced further if opposite spin electrons remain spatially separated, however this requires increased localization which increases the kinetic energy. To conceptualize this point, we recall that the kinetic energy of a quantum particle in a 1-D infinite potential well is proportional to k^2, where the wavenumber, k, is inversely proportional to the size of the well. This means that a narrower well leads to smaller wavelengths, or larger wavenumbers, and greater kinetic energy. The contribution to the electron interaction energy due to the anti-symmetry of the wavefunction is called the exchange energy, and the further reduction in energy due to increased localization is due to electron correlation. There is no known general expression for the exchange and correlation potential. Thus far, the total ground state energy can be written as:

$$\langle\Psi|\hat{H}|\Psi\rangle = V_{nuc}[n] + J[n] + \langle\Psi|\hat{T}|\Psi\rangle + U_{XC} \tag{3.7}$$

The ability to evaluate the ground state energy 3.7 for general systems is due to Hohenberg-Kohn and Kohn-Sham theories. Since the Hamiltonian, $\hat{H}$, is determined from the external potential, V, which for molecular or solid systems is due to the arrangement of nuclei, but could also be due to a static electric or magnetic field, it is clear that the electron density for a fixed number of electrons is a functional of the external potential, V (i.e.,V determines $n(\mathbf{r})$). Hohenberg and Kohn [38] proved that this mapping is one-to-one and onto (reversible), showing that for a given electron

density $n(\mathbf{r})$, the external potential could be uniquely determined, in theory. This also means that all other terms in the Hamiltonian must be functionals of the density. And since the electronic energy is obtained from the expectation value of the Hamiltonian, it too must be a unique functional of the electron density:

$$E[n] = V_{nuc}[n] + T[n] + J[n] + U_{XC}[n] \tag{3.8}$$

Thus, the task of determining the ground state energy of an electron-ion system is transformed from determining wavefunctions and evaluating expectation values to minimizing variations in the energy with respect to variations in electron density (i.e., finding n such that $\delta E/\delta n = 0$). Of course the trouble now is that there are no analytic expressions for $T[n]$ and $U_{XC}[n]$, so these must be approximated somewhow.

Kohn and Sham [42] then showed that a system of interacting electrons with density $n(\mathbf{r})$ could be mapped onto a fictitious system of non-interacting electrons with the same density. Since the energy was shown to be a unique functional of the density, the ground state energy of the interacting system must be identical to the ground state energy of the non-interacting system. The problem is then to solve the system of equations:

$$-\frac{1}{2}\nabla^2\psi_i + V_0\psi_i = \varepsilon_i\psi_i \tag{3.9}$$

where ψ_i are wavefunctions of non-interacting electrons and V_0 is an effective potential that is generated by the field of nuclei and all other electrons. Since the interacting and non-interacting systems share the same density we have:

$$\int \Psi^*(\mathbf{r}_1, ..., \mathbf{r}_N)\Psi(\mathbf{r}_1, ..., \mathbf{r}_N)d\mathbf{r}_2...d\mathbf{r}_N = n(\mathbf{r}) = \sum_i^N \psi_i^*(\mathbf{r})\psi_i(\mathbf{r}) \tag{3.10}$$

where Ψ is the many electron wavefunction of the interacting system. The kinetic energy of the non-interacting system is then:

$$T_0 = -\frac{1}{2}\sum_i^N \int \psi_i^*(\mathbf{r})\nabla^2\psi_i(\mathbf{r})d\mathbf{r} \tag{3.11}$$

The electronic energy of the Kohn-Sham wavefunctions can be written as:

$$E[n] = V_{nuc}[n] + J[n] + T_0[n] + E_{XC}[n] \tag{3.12}$$

where in this case, $E_{XC}[n] = (T[n] - T_0[n]) + (U[n] - J[n])$ represents the difference in kinetic and electron-electron interaction energies between the fictitious non-interacting system of electrons and the real interacting one. In this way, E_{XC} is the only functional that must be approximated and model systems can be used to motivate such approximations.

The Kohn-Sham effective potential, V_0, has contributions from the field of nuclei, V_{nuc}, the electrostatic (classical) electron repulsion, V_H, and the electron exchange and correlation. The latter is obtained from the functional derivative of the exchange and correlation energy with respect to the electron density:

$$V_0 = V_{nuc} + V_H + \frac{\delta E_{XC}}{\delta n} \tag{3.13}$$

Since the Kohn-Sham wavefunctions are determined from the effective potential, and the effective potential depends on the Kohn-Sham wavefunctions, the set of Kohn-Sham equations must be solved self-consistently. The procedure is generally to guess trial electron wavefunctions, such as atomic orbitals for example, which generates the effective potential, V_0, which in turn is used to obtain new wavefunctions and compute a charge density. The latter density will not be the same as the trial density unless it corresponded to the ground state density (i.e, $\delta E/\delta n = 0$). The density is then updated using some numerical method and the procedure is repeated until the effective potential generates wavefunctions with electron density that is the same as the density from which is was determined (numerically the same means "to within some specified threshold"). There now exist many methods for converging to the ground state density self-consistently. [64]

A simple way to approximate E_{XC} would be to suppose that it only depends on the electron density at each point in space - a local density approximation (LDA). The total contribution of such an approximate E_{XC} would then be the spatial integral:

$$E_{XC}[n] = \int n(\mathbf{r})\epsilon_{XC}[n]d\mathbf{r} \tag{3.14}$$

where ϵ_{XC} is an exchange and correlation energy density. An expression of this form is convenient as various functional forms can easily be substituted for ϵ_{XC}. The most common local density approximation uses the exchange and correlation energy density of the uniform electron gas (UEG). The exchange part can be determined exactly as an analytic function of the density, but the correlation part must be parametrized. It has become common practice to split the exchange and correlation energy into its exchange component and correlation component.

It can be shown that the exchange energy density of the UEG is:

$$\epsilon_X = -\frac{3}{2}\left(\frac{3n}{4\pi}\right)^{1/3} \tag{3.15}$$

Thus, the exchange energy in a local density approximation becomes:

$$E_X^{LDA} = -\frac{3}{4}\left(\frac{3}{\pi}\right)^{1/3}\int n(\mathbf{r})^{4/3}d\mathbf{r} \tag{3.16}$$

And in the case of spin-polarized systems, each spin component is treated separately in a local spin-density approximation (LSDA):

$$E_X^{LSDA} = -\frac{3}{2}\left(\frac{3}{4\pi}\right)^{1/3}\sum_\sigma\int n_\sigma(\mathbf{r})^{4/3}d\mathbf{r} \tag{3.17}$$

where the sum is over both spin components, σ.

The corresponding correlation energy density of the UEG, ϵ_C, does not have an analytical expression, thus it is typically parametrized from more sophisticated numerical methods such as Quantum Monte-Carlo (QMC).

The LSDA typically works well in metals where valence electrons are delocalized and behave similarly to the UEG. In real chemical systems, electrons can behave very differently from the UEG leading to significant spatial variations in electron density. One can simply think of H bonding in water as an example of non-uniform electron charge distribution. Indeed, the shortcomings of local approximations to the exchange and correlation energy for water and ice has been the subject of considerable research. [28] Another example, which pertains to this thesis, is in solids containing partially filled d shells. In this case, electrons are typically highly correlated, rendering local

approximations questionable, and leads to increased electron localization, leading to variations in electron charge density that cause the LSDA to fail (in fact, GGA's, discussed below, also fail and other methods are needed). To account for non-uniform electron charge density, improvements to the LSDA are needed. In what follows, all mentions of the LDA or LSDA refer the form shown in equations 3.16 or 3.17.

3.1.1 Generalized Gradient Approximation (GGA)

In order to improve on the LDA exchange and correlation energy functional, since charge densities are not generally uniform, perhaps the simplest suggestion would be to add some dependence on the charge density gradient. Such functional forms compose a class of exchange and correlation functionals called generalized gradient approximations (GGA):

$$E_{XC}^{GGA} = \sum_{\sigma} \int n(\mathbf{r}) \epsilon_{XC}(n_\sigma, \nabla n_\sigma) d\mathbf{r} \tag{3.18}$$

It is important to realize that GGAs are still local approximations because the contribution to the total exchange and correlation energy depends only on the density and density gradient at each point in space individually. Generally, GGAs are written as an enhancement, F_X, over the LSDA. Treating exchange and correlation separately, and writing only the exchange part for simplicity:

$$E_{X}^{GGA} = -C_X \sum_{\sigma} \int n_\sigma(\mathbf{r})^{4/3} F_X(n_\sigma, \nabla n_\sigma) d\mathbf{r} \tag{3.19}$$

where $C_X = \frac{3}{2}\left(\frac{3}{4\pi}\right)^{1/3}$, is the coefficient from the UEG exchange. This way, if $F_X = 1 + f(n_\sigma, \nabla n_\sigma)$, and f is constructed in such way as to vanish when n_σ is uniform, the exact exchange of the UEG is recovered in the appropriate limit.

In 1986, Becke proposed the B86a exchange and correlation functional [7], which was re-introduced in 1996 by Perdew, Burke, and Ernzerhof (PBE), [67] with only small differences in the constants β and γ, appearing in equation 3.20. In B86a, β and γ were fit to atomic exchange energies while in PBE they were chosen to satisfy a set of constraints. Defining the dimensionless density gradient, $\chi_\sigma = |\nabla n_\sigma| / n_\sigma^{4/3}$,

the B86a and PBE functionals can both be written in the form:

$$E_X^{B86a/PBE} = E_X^{LSDA} - \sum_\sigma \frac{\beta}{C_X} \int n_\sigma^{4/3} \frac{\chi_\sigma^2}{1+\gamma\chi_\sigma^2} d\mathbf{r} \tag{3.20}$$

In plane-wave codes, the PBE functional is typically used over B86a for some reason — perhaps because it has been implemented more widely. Nevertheless, it is important to realize that GGA's which are constructed as enhancements to the LSDA remain local approximations. Despite providing more accurate descriptions of variations in charge density, GGA's still suffer from delocalization errors so that materials with highly correlated electrons are poorly described. There are several ways to improve on GGA's, but here the focus will be on GGA+U and SCAN, to maintain pertinence with the thesis. Other methods include hybrid functionals, the Random Phase Approximation (RPA), and Quantum Monte Carlo (QMC).

GGA's also provide poor descriptions of long-range, non-bonding interactions, and PBE tends to fail in the limit of large charge density gradients. The formulation of local exchange and correlation energy functionals can sometimes lead to dispersion-type interactions. These details are not provided in this thesis, but are well explained in Ref. [9]. The subject of adding dispersion corrections to the total Kohn-Sham energy has been well studied and several methods are available. The computations performed in Chapter 4 employ the method of Grimme *et* al. [31] with Becke-Johnson damping. [8, 10]

3.1.2 GGA+U

Probably the simplest, and definitely the fastest, way to improve on the LSDA or GGA's to better account for localized electrons is the LSDA+U or GGA+U method. The general idea is to add to the LSDA or GGA energy a term which penalizes partial occupancies of electron states. There exists several flavours of +U; the one of Dudarev [26] is employed in this thesis. The general form is:

$$E_{XC}^{GGA+U} = E_{XC}^{GGA} + \frac{U-J}{2} \sum_\sigma \left[\left(\sum_m n_{m,m}^\sigma \right) - \left(\sum_{m,m'} n_{m,m'}^\sigma n_{m',m}^\sigma \right) \right] \tag{3.21}$$

where n^σ is the on-site occupation matrix and the summations inside the square brackets are performed over the m orbitals — the five $3d$ orbitals, for example. The term inside the square brakets vanishes when $n = n^2$, corresponding to an idempotent occupancy matrix, meaning that its eigenvalues — the occupancies of each $3d$ orbital, for example, are either 0 or 1. With the form 3.21, the screened Coulomb electron-electron repulsion, U, and the exchange parameter, J, do not enter separately, thus this implementation requires only a single parameter: the difference $U - J$. In this construction, J is effectively set to 0 and U is chosen. The effect of the penalty term on the right hand side of equation 3.21 is to force delocalized electron states with partial occupancies in, for example, $3d$ orbitals, to occupy a single $3d$ orbital, increasing localization and reducing electron-electron repulsion.

The choice of U, or $U - J$ in Dudarev's approach, is arbitrary, thus this method is generally referred to as empirical. In some cases the magnitude of U can be motivated, or can be parametrized with experimental data, but there are fundamental limits with GGA+U as a true first-principles method. Chapter 4 aims to shed some light on the application of GGA+U for Li-containing TM oxides used in Li-ion batteries.

3.1.3 SCAN+rVV10

Another approach to improve on GGA's has been to include second order terms in the energy functional. Terms that involve the electron density are zeroth order, those that include density gradients are first order, thus second order terms involve the Laplacian, which corresponds to the electron kinetic energy, τ. Exchange and correlation energy functionals that include second order terms are generally referred to as meta-GGA's. Thus, meta-GGA exchange and correlation energy functionals have the general form:

$$E_{XC} = \int \epsilon_{XC}(n, \nabla n, \tau) d\mathbf{r} \tag{3.22}$$

where $\tau = \frac{1}{2}\sum_{occ} |\nabla \psi_i|^2$, is the kinetic energy density. There exist many meta-GGA's, but in 2016, the Strongly Constrained and Appropriately-Normed (SCAN) meta-GGA functional [77] was shown to be well suited for diversely bonded systems [76], including $3d$ transition metal complexes.

SCAN still employs the enhancement factor approach, such as equation 3.19, to the LSDA so that in the limit of highly delocalized electrons, the exact exchange of

the UEG is recovered. The main ideas behind SCAN are 1) to impose constraints to the enhancement factor — these can be thought of as phenomenological limits, and 2) to impose norms, or parametrizations, to idealized systems. This second part is not entirely novel, since the LSDA uses the UEG as a norm. SCAN however uses five norms: i) the UEG, ii) jellium surface energy; the boundary of a positively charged slab and the UEG — an idealized metal surface, iii) the H atom, iv) the He atom and compressed Ar_2 (non-bonded Van der Waals "molecule"), and v) the $Z \to \infty$ limit of the two-electron ion. All five of these norms represent limits where the electronic behaviour is "known".

SCAN is still constructed locally and thus will not capture long-range non-bonding interactions. In the spirit of dispersion corrections for the LSDA and GGA's, SCAN+rVV10 was developed. [65] It was demonstrated to yield good interlayer binding energies and distances for a variety of layered materials. Computations in this thesis consistently employ the SCAN+rVV10 merely due to the fact that layered structures are considered.

3.2 Bloch's Theorem and Plane-waves

In order to solve the Kohn-Sham equations, a basis set must be chosen. The functions within the basis set are the building blocks of the electronic wavefunctions. A complete basis set allows, in theory, one to represent any wavefunction as a linear combination of some of its elements. Solutions to the Kohn-Sham equations for periodic structures can be obtained more efficiently if plane-waves are used as basis functions. This is due to Bloch's theorem, which states that in a periodic structure, each energy eigenstate wavefunction can be written in terms of the periodicity of the lattice. The precise form of the wavefunctions consists of a plane wave and a cell periodic function:

$$\psi_j(\mathbf{r}) = \exp(i\mathbf{k} \cdot \mathbf{r}) f_j(\mathbf{r}) \tag{3.23}$$

where for each electron wavefunction, the functions f_i have the same periodicity as the lattice: $f_j(\mathbf{r}) = f_j(\mathbf{r} + \mathbf{R_l})$, with R_l a lattice vector. In equation 3.23, $\mathbf{k}$ is a wavevector, the set of which that is required will be discussed in Section 3.3. Since the functions f_j have the same periodicity as the lattice, they can be expanded in

terms of plane waves whose wavevectors, $\mathbf{G}_l$, belong to the reciprocal lattice:

$$f_j(\mathbf{r}) = \sum_l c_{j,l} \exp(i\mathbf{G}_l \cdot \mathbf{r}) \tag{3.24}$$

where the $c_{j,l}$ are expansion coefficients. Substituting 3.24 into 3.23 demonstrates that the wavefunctions of electrons in a periodic structure can be expressed as a linear combination of plane-waves:

$$\psi_j(\mathbf{r}) = \sum_l c_{j,l} \exp(i(\mathbf{k} + \mathbf{G}_l) \cdot \mathbf{r}) \tag{3.25}$$

Equation 3.25 represents a discreet plane-wave spectrum. As a consequence, it is possible that an infinite number of plane-wave coefficients would be needed to describe an electronic state exactly. In practice, the set of plane-waves must be truncated to a finite number. Since the kinetic energy associated with a plane-wave with wavevector $(\mathbf{k} + \mathbf{G})$ is proportional to $|\mathbf{k} + \mathbf{G}|^2$, it can be argued that those plane-waves with very large $\mathbf{G}$'s should not contribute as much to the wavefunction. In fact, plane-waves with large wavevectors have short wavelengths, meaning they oscillate rapidly which physically does not represent well valence electrons sufficiently far from nuclei; a point discussed in section 3.4. In practice, the number of plane-wave coefficients are limited based on a maximum allowable plane-wave kinetic energy with corresponding reciprocal lattice vector, $\mathbf{G}_{max}$; this is called the plane-wave energy cut-off.

3.3 k-points

The symmetries of a periodic structure determine the set of **k**-points that make up the electronic wavefunctions according to Bloch's Theorem. These **k**-points are uniquely defined in the first Brillouin zone — the reciprocal primitive cell. For an infinite solid, the Brillouin zone is continuous thus contains an infinite number of **k**-points. But the wavefunction expansion for two **k**-points very close to together will have nearly the same energy. It is thus possible to approximate the wavefunction of an infinite periodic structure using a finite set of **k**-points. By computing the total energy with an increasingly dense set of **k**-points, a desirable precision threshold can be achieved. This procedure is always done in practice to ensure computational precision.

3.4 Pseudopotentials and Projector-augmented Waves

Plane-waves are well suited for computational descriptions of electron wavefunctions with sufficiently small kinetic energies. This corresponds to regions of space where wavefunctions do not have a large degree of curvature. With increasing atomic number, valence electrons contain more radial nodes near the atomic nucleus, and p, d, and f orbitals each contain more angular nodes. Thus, the number of plane-wave coefficients needed to precisely describe rapidly oscillating wavefunctions near nuclei quickly becomes intractable with heavier atoms. Tightly bound core electrons also require a large number of plane-wave coefficients since their orbitals are more compressed in heavier atoms, leading to greater kinetic energy. In order to maintain computational tractability, atomic wavefunctions are typically "pseudized". This generally means that some electrons are treated as core electrons and are "frozen", while the remaining electrons are deemed as valence and have modified wavefunctions that contain no radial nodes. With this construction, only electrons deemed as valence are included in the Kohn-Sham equations. It is important to realize that in pseudopotential terminology, core and valence do not necessarily refer to the conventional concepts, rather to the electrons that are "frozen" and those that are "pseudized", respectively. Figure 3.1 shows a sketch of how valence electron wavefunctions and the resulting nucleic potential are modified within a cut-off radius r_c. This sketch was re-created from Ref. [64]. It shows the true wavefunction of a valence electron with four radial nodes with the pseudo-wavefunction identical outside of a cut-off radius, r_c, but with no radial nodes within. The resulting pseudopotential is much softer that the true potential.

Though figure 3.1 demonstrates loosely the general idea, there are several approaches for constructing pseudopotentials. Hamann *et* al. first introduced norm-conserving pseudopotentials in 1979. [33] Then, in 1990, Vanderbilt introduced ultra-soft pseudopotentials. [83] Four years later, Blöchl bridged the ultra-soft method with the existing full-potential linearized augmented plane-wave (FLAPW) all-electron method in what was called projector augmented-waves (PAW). [12] The PAW method has since been implemented in most plane-wave DFT codes and is likely the most popular choice for "pseudized" wavefunctions. The PAW method differs significantly from the norm-conserving and ultra-soft methods in its construction which makes

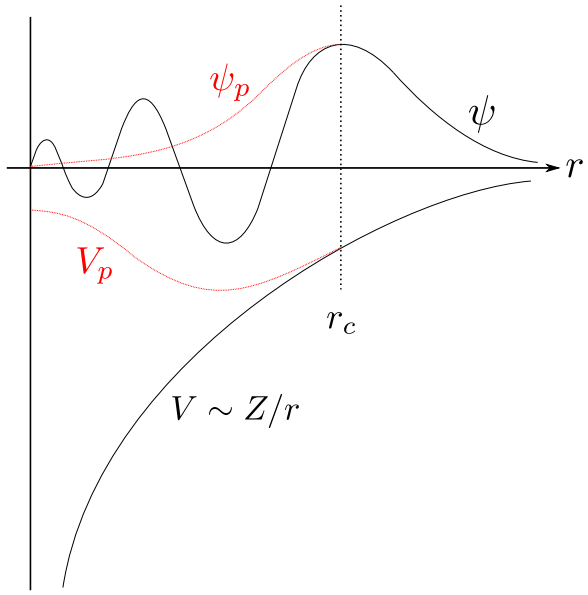

Figure 3.1: Sketch of a pseudo-wavefunction and pseudopotential. The red lines show pseudo quantitites within a cut-off radial distance from an atomic center, r_c. The real and pseudo- wavefunctions, ψ and ψ_p, and potentials, V and V_p, are identical beyond r_c. The wavefunction and nuclear potential are plotted on the same vertical axis in arbitrary units for the purpose of illustration.

PAW datasets more transferable and efficient, particularly for large atoms. All computations presented in this thesis employed PAW datasets.

3.5 Projected Density of States

The density of states (DOS) is the energy spectrum of the system so that integrating the DOS yields the electron population at a given energy. The total DOS for a periodic system is independent of the choice of basis set, insofar as the energies are not dependent on it. However, the total DOS does not provide contributions from the different components of the system. For computations on periodic structures that take advantage of Bloch's Theorem and use plane-wave basis functions, the contribution to the total DOS from each atomic site is not obvious; plane-waves are defined by the periodicity of the lattice and not by atomic wavefunctions. To gain insight into how individual atoms contribute to the overall energy spectrum, the DOS can be decomposed into contributions from each atomic site. This task is not possible to do directly from plane-waves, thus a change of basis is needed so that electron states

are represented by functions centered on each atomic site. The most natural way to do that is to project the plane-waves onto atomic orbitals (spherical harmonics). For example, if a computation involved O atoms with a PAW dataset that treated the $2p$ electrons as valence, $2p$ basis functions centered on each O site could be used in the plane-wave projection. Often, to provide a more complete projection, additional atomic orbitals are also used in the projection; in the previous example, $3s$ spherical harmonics could be included. For an arbitrary unit cell, the result is a contribution to the total energy spectrum from each atomic basis function centered on each atomic site. These quantities are referred to as projected densities of states (pDOS).

Generally, default projection schemes within plane-wave DFT programs provide spherical harmonics decomposition from plane-waves only within a sphere of fixed radius. Even though it is possible to adjust the size of the spheres, it is not possible to include all of the electron charge without double counting. A more general approach was implemented in the Local-Orbital Basis Suite Towards Electronic-Structure Reconstruction (LOBSTER) program, [56] where the projection from plane-waves to atom-centered spherical harmonics is done in a flexible manner with the attempt to include all of the electron charge without double-counting. In the case of systems with more complex interactions, LOBSTER allows specification of additional basis functions so that the projection can be more complete. For example, in the case of Ni in NiO_2, by including $4p$ basis functions in addition to the $3d$ and $4s$ functions, all of the electron charge to within ~ 1 % is included in the projection.

3.6 Crystal Orbital Hamilton Population

With contributions to the total band structure energy from each atomic site, an analysis of pair-wise orbital interaction seems plausible. Indeed, in early electronic structure computations where local orbitals were used as basis functions, the crystal orbital overlap population (COOP) was developed. [37, 39] The COOP is a decomposition of the DOS by number of electrons; the integrated COOP up to the Fermi level yields a number of electrons analogous to a bond order, i.e., the difference between the numbers of bonding and anti-bonding electrons. It is computed from the off-diagonal elements of the overlap matrix between basis functions centered on neighbouring atomic sites. Omitting the spin dependence for notation simplicity, the projection of

each one-electron (Kohn-Sham) orbital onto basis functions can be written as:

$$|\psi_j\rangle = \sum_{RL} c_{RL,j} \, |\chi_{RL}\rangle \tag{3.26}$$

Where the summation is performed over all atomic sites, R, and all atom-centered basis functions, L, and the coefficients, $c_{RL,j}$ form eigenvectors for band j. The overlap population between two basis functions, L and L', centered on two different sites, R and R', within band j is:

$$n(j, RL, R'L') = f_j c^*_{RL,j} S_{RL,R'L'} c_{R'L',j} \tag{3.27}$$

Where $S_{RL,R'L'} \equiv \langle \chi_{RL} | \chi_{R'L'} \rangle$ is an element of the overlap matrix S and f_j is the occupation number of the jth band. The total overlap population between two sites, R and R' is then the sum of the overlaps from each band and each basis function:

$$n(R, R') = \sum_{j,L,L'} n(j, RL, R'L') \tag{3.28}$$

The COOP is defined as the population-weighted DOS, yielding an energy resolved population between atomic site pairs, R and R':

$$\mathrm{COOP}_{R,R'}(\epsilon) = \sum_{j,L,L'} \frac{V_0}{(2\pi)^3} \int_{BZ} d\mathbf{k} \delta(\epsilon - \epsilon_j(\mathbf{k})) f_j c^*_{RL} S_{RL,R'L'} c_{R',L'} \tag{3.29}$$

where the summation is carried out over all bands and each basis function centered at sites R and R', and the integration over $\mathbf{k}$ is carried out within the first Brillouin zone, thus V_0 is the volume of the primitive cell. Positive COOP values correspond to bonding, negative value to anti-bonding, and null values to non-bonding interactions. Thus, the COOP provides information on the number of electrons that make up a bond. The elements of the overlap matrix that yields the COOP can be thought of as the contribution to the overall wavefunction due to the interaction of two basis functions centered on neighbouring sites.

Rather than partitioning the DOS by number of electrons via the overlap matrix, the DOS can be partitioned by the band energy by evaluating the elements of the Hamiltonian matrix in the local basis representation. This is dubbed the crystal

orbital Hamilton population (COHP). [25] The construction is the same as the COOP, except that the overlap matrix is replaced with the Hamiltonian matrix, $H_{RL,R'L'}$:

$$\mathrm{COHP}_{R,R'}(\epsilon) = \sum_{j,L,L'} \frac{V_0}{(2\pi)^3} \int_{BZ} d\mathbf{k}\delta(\epsilon - \epsilon_j(\mathbf{k})) f_j c^*_{RL} H_{RL,R'L'} c_{R',L'} \tag{3.30}$$

Thus, contrary to the COOP, negative COHP values denote bonding interactions since, in this case, they serve to lower the overall band energy. It is then typical for the negative COHP to be plotted so that bonding interactions are shown as positive values remaining consistent with the COOP picture. Thus, the COHP decomposes the total band structure energy into regions of bonding, anti-bonding, and non-bonding overlaps between neighbouring basis functions. This allows analysis of bond character of molecular orbitals, or bands, for atoms in different chemical environments.

3.7 Charge partitioning

The idea of assigning charge to individual atoms within complexes was perhaps pioneered by Mulliken. [70] This was done in the framework of linear combinations of atomic orbitals (LCAO) to obtain molecular orbitals whose overlap matrices were evaluated. The later development of the COOP is the same in spirit, except that the molecular orbitals are obtained from a self-consistent method, such as DFT in modern computations. Thus, by computing the COOP for atom-centered basis functions, one automatically obtains Mulliken charges. Before the advent of self-consistent computations, Löwdin [53] developed a numerical technique to evaluate overlap integrals that involved orthogonalization of basis functions. Upon obtaining atom-centered basis functions from plane-waves, it is then possible to evaluate the overlap matrices by both the Mulliken or Löwdin formalisms.

A different approach to assigning electrons to atoms within an extended structure is that of Bader. [6] In this scheme, individual orbitals are irrelevant; the quantity of interest is the electron charge density. The charge is divided based on what Bader called "zero-flux surfaces". In essence, this is a 2-dimensional surface corresponding everywhere to a local minimum in the 3-dimensional electron charge. This can most easily be pictured by imagining the electron charge along a chemical bond; the point

along the inter-atomic direction for which the charge takes on its minimum value will be a point on the Bader surface.

In all three cases, interesting insight can be gained by comparing atomic charges under different conditions; changes in atomic charges could be a signature of a different bonding environment.

Chapter 4

An analysis of the GGA+U formalism applied to TM-containing positive electrode materials for Li-ion batteries

By far the most common formalism used to compute properties of positive electrode materials for Li-ion batteries from first-principles is GGA+U. This framework is an extension of the GGA approximation to better account for localized electron states, such as TM-O bonds in TM oxides, for example. The general idea is to add a local potential, with strength determined by the value of U, centered about each atom whose electronic character would be poorly captured by GGA alone. The fact that U is a tunable parameter and must be chosen for each element within a material renders this method empirical by nature and it may not be obvious how the choice of U influences computed material properties. The goal of this chapter is to demonstrate how structural, electronic, and electrochemical properties of Li-containing Ni, Co, and Mn oxides depend on the choice of U.

Ni, Co, and Mn are the transition metals contained in the largest quantity in modern, high energy density positive electrodes, so their respective Li-containing oxides serve as good model materials for this study. Comparisons of crystallographic parameters (lattice parameters, TM-O bond lengths) and average voltages with experimental values, along with detailed electronic structure analyses, will provide insight into how U fundamentally influences the material. As a result, the consequences of choosing a particular U value can be better appreciated.

In the Li-ion battery positive electrode literature where GGA+U is widely employed, the choice of U is mostly guided by a 2006 publication from Ceder *et* al. [86] in which U was parametrized using experimental oxidation energies. V, Cr, Mn, Fe, Co, Ni, Cu oxides were considered, including mutliple TM oxidation reactions when appropriate (e.g., 4 FeO + $O_2 \rightleftharpoons$ 2 Fe_2O_3 and 6 FeO + $O_2 \rightleftharpoons$ 2 Fe_3O_4). Computed oxidation energies were obtained with $U = 0, 2, 4, 6$ eV for all TMs except for Ni

where $U = 8$ was also included. The U value which gave an oxidation reaction energy in agreement with the experimental value was indicated. The original purpose of this work may not have been to provide a rigorous determination of the best choice of U for TM oxide positive electrode chemistries, however, this appears to have been the interpretation in the literature. According to Google Scholar, this paper has been cited 1765 times. Nevertheless, some authors have opted to use U values different [15] from those quoted in ref. [86], or even chose to use GGA without U correction, [23] particularly when performing computations on mixed TM oxides such as NMC materials ($LiNi_{1-x-y}Mn_xCo_yO_2$). However, the consequences of choosing a particular value of U remains largely undiscussed. Additionally, Ref. [86] employed GGA+U without dispersion corrections, but particularly in de-lithiated layered oxides, some long-range, non-bonding interactions are expected. Therefore, in this work, dispersion corrections are added for all values of U using the method of Grimme *et* al. with Becke-Johnson damping. [31]

In 2016, the Strongly Constrained and Appropriately-Normed (SCAN) "meta-GGA" functional was published, demonstrating a significant improvement over GGA for a wide range of physical properties of a broad spectrum of chemical compostitions that, importantly, include transition metal oxides — although of different compositions from the ones considered here. [66, 76, 77] Corresponding computations using the SCAN XC functional will also be presented to be compared with GGA+U and experiment.

Section 4.1 describes the computation sets that will be presented for each material, along with the measured quantities to which computational results will be compared. Section 4.2 covers the basic theory required to interpret computed electronic structures, so that the the way in which U influences the TM-O interaction can be better appreciated. Results are then presented for each of the three lithiated and de-lithiated TM oxide chemistries. The final section of this Chapter provides some remarks in summary. Hopefully the work presented here will serve to heighten awareness towards the use of GGA+U for TM-containing positive electrode materials.

4.1 Computation Sets

Table 4.1 provides all TM-containing compounds considered in this study, along with experimentally determined lattice parameters, TM-O distances, and average voltages, to be compared with the computed values within the GGA+U formalism. Three chemistries were chosen to cover Ni, Co, and Mn oxides; (Li)NiO_2 (LNO), (Li)Co_2 (LCO), and (Li)Mn_2O_4 (LMO), which are relevant Li-ion battery positive electrode materials. The crystallographic parameters are determined from diffraction experiments (X-ray or neutron) and the average voltages from electrochemical de-lithiation. The experimental TM-O distance for CoO_2 is not available since the material is highly unstable making *in-situ* diffraction measurements difficult; the lattice parameters can be obtained from the peak positions, but the TM-O is determined from a peak intensity ratios, which are not sufficiently well-resolved. In a Ferromagnetic (FM) ordering is assumed for all structures since, in each case, TMs are arranged on a triangular sub-lattice that is geometrically frustrated. Magnetic ordering other than FM needs to be long range and thus energy differences are assumed to be small. At room temperature none of the chemistries considered here are magnetic, but computations are performed at 0 K where there is no thermal energy to disorder magnetic structures. For these resons, it is assumed that FM ordering is reasonable in these computations.

The true average voltage for a particular intercalation reaction is given by the integrated voltage-composition curve. Obtaining voltage-composition curves from first-principles is computationally intensive, but the average voltage between a fully lithiated composition and a fully de-lithiated composition is easily computed, if both structures are known; $V_{avg} = (dG_{Li}/dn - dG_p/dn)/e \approx (E_{Li} - \Delta E_p/\Delta n)/e$. $G = E + PV - TS$ is the Gibbs free energy, thus dG_{Li}/dn and dG_p/dn are the changes in Gibbs free energies of *bcc* Li metal and of the positive electrode as the Li content changes by an amount dn. Since the structure of *bcc* Li metal does not change as Li is added, dG_{Li}/dn is constant and equals the free energy per atom of the material. E_{Li} is the energy per atom of *bcc* Li metal, and $\Delta E_p/\Delta n$ is the energy difference per Li of the fully lithiated and de-lithiated structures. In this equation, the enthalpic (PV) and entropic (TS) contributions to the Gibbs free energy are assumed to be small so that $\Delta G \approx \Delta E$. The PV term can easily be verified to be negligible; the volume change between $LiNiO_2$ and NiO_2, for example, is ~ 4 $\mathring{A}^3$, and ambient pressure is

$\sim 1 \times 10^{-4}$ GPa, giving $PV \approx 2 \times 10^{-6}$ eV, which is 4 order of magnitude smaller than meaningful energy differences. The TS is more challenging to fully quanitify since it has contributions from both configurational and vibrational entropy. When comparing energies between fully lithiated and de-lithiated structures, however, there are no degrees of freedom for Li arrangement. This is an idealized scenario, so results should not be expected to match experiment perfectly. To determine the experimental average voltage that corresponds to the one computed, the measured voltages of fully lithiated and de-lithiated structures must be averaged, rather than integrating the voltage-composition curve.

The goal of this Chapter is to understand how the electronic structure of lithiated and de-lithiated chemical counterparts change with U, and how that leads to different electrochemistry. To this end, the computation sets presented in this Chapter include: full structure relaxation to determine equilibrium (non-thermal) lattice parameters and atomic coordinates; projected electronic densities of states (pDOS), projected Crystal Orbital Hamilton Populations (pCOHP),[25] magnetizations, and Mulliken and Loedwin population analyses to estimate charge transfer; and Bader charges [6, 36, 72, 88] to investigate spatial changes in electron charge. Structure relaxations were performed using the Vienna Ab-initio Simulation Package (VASP) [45, 44, 43] with projector augmented wave data sets (PAW) [43] to model core electrons. PAW data sets treated the TM $3d$ and $4s$, the O $2s$ and $2p$, and the Li $2s$ electrons as valence. Energy and force convergence, with respect to the PAW maximum kinetic energy cut-off and **k**-point sampling, was achieved for each structure independently with thresholds of 1 meV per formula unit and 0.01 eV/$\mathring{A}$, respectively. The pDOS, pCOHP, and Mulliken and Loedwin populations were computed using LOBSTER [22, 56, 58, 57]. These computations were each performed for values of U ranging from 0.0 to 8.0 eV, in 0.5 eV increments (LOBSTER computations were only performed for selected U values). The aim is to paint a complete picture of how the strength of U leads to changes in material properties. Compared to the work in ref. [86], where 2 eV increments in U were used, this study employed a finer U spacing in order to identify potential changes in spin-state that can manifest as non-monotonic changes in material properties.

Chemistry	Space group	Lattice Parameters (Å)	TM-O distance (Å)	Average Voltage (V)
$LiNiO_2$ [48]	$R\bar{3}m$	$a = b = 2.8734$ $c = 14.211$ $z = 0.24$	1.975	3.88
NiO_2 [48, 21]	$R\bar{3}m$	$a = b = 2.8118$ $c = 13.338$	1.85	
$LiCoO_2$ [40]	$R\bar{3}m$	$a = b = 2.818$ $c = 14.06$ $z = 0.2395$	1.9224	4.45
CoO_2[1]	P3m1	$a = b = 2.822$ $c = 4.2929$	—	
$LiMn_2O_4$ [50]	Fd3m	$a = b = c = 8.237$ $x = 0.26$	1.9209	4.05
Mn_2O_4 [29]	Fd3m	$a = b = c = 8.0407$ $x = 0.2625$	1.9149	

Table 4.1: Experimental crystallographic parameters and average voltages for positive electrode chemistries considered in this Chapter.

4.2 Ligand Field Theory

Before proceeding to computational results, it is important to consider how the construction of the GGA+U formalism modifies electron energies and how that may be reflected in TM-O interactions. Section 3.1.2 covered the basic mathematical construction of the GGA+U formalism. In simple terms, as the strength of U increases, partially occupied spin-dependent energy levels are penalized, giving preference to either fully occupied or completely unoccupied levels. First row TM atomic orbitals have the $4s^2 3d^n$ electron configuration. As U is made larger, the n $3d$ electrons will preferentially occupy individual d orbitals, that will be pushed to lower energies due to the penalty from U. Thus, an energy gap between occupied and unoccupied states will result, making the transfer of $4s$ electrons to $3d$ orbitals less energetically favourable. Hybridized orbitals with d character, in TM-O interactions for example, will also get penalized by U. However, in such orbitals there is greater degree of flexibility compared to isolated atomic orbitals, allowing electrons to re-arrange to minimize the total energy. Generally, this means that spin-dependent electron states that can be fully occupied are shifted to lower energies as U increases, while those that are unoccupied are shifted to higher energies. The following discussion

describes TM-O interactions according to Ligand Field Theory,[30] in the particular case of octahedral coordination, and how U may influence the population of resulting interacting orbitals.

In octahedrally coordinated TM complexes, the atomic orbital symmetry determines the energy splitting of the resulting hybridized orbitals. For this reason, the term symmetry orbitals denotes the combination of atomic orbitals that interact due their shared symmetry elements. In the case of first row TMs, such as the ones considered here, the TM $3d$, $4s$, and $4p$ atomic orbitals can be understood to hybridize with O_{2p} orbitals to form bonding, non-bonding, and anti-bonding symmetry orbitals. In the case of molecular complexes, the resulting energy spectrum is discreet, but for extended structures such as solid crystals, the resulting symmetry orbitals should be thought of as bands spanning an energy range. It is easier to describe and visualize electron energies as single levels, as will be done in this discussion, but later, when discussing densities of states, the band nature will be obvious, and the term "band" will used instead of "level".

Figure 4.1 (a) shows the three $2p$ atomic orbitals with Cartesian axes aligned in the direction of each lobe. Figure 4.1 (b) shows the five $3d$ atomic orbitals, each aligned within a depicted TM-O_6 octahedron (the TM ion is not shown, but occupies the center of each octahedron). The octahedra have been added to the orbital depictions, which were reproduced from Ref. [32]. In the electrostatic theory, the O atoms can be thought of as point charges of magnitude $2e$, having each had two electrons transferred to fill their $2p$ orbitals. Since the $3d_{xy}$, $3d_{xz}$, and $3d_{yz}$ orbitals are directed towards the octahedral edges and faces, the electrostatic repulsion from O ions is expected to be weaker compared with that from the $3d_{z^2}$ and $3d_{x^2-y^2}$ orbitals, which are directed towards the O ions at the octahedral vertices. In this picture, the TM ion is treated as having fully transferred charge so that O atoms have full $2p$ shells, and thus, the TM-O bonds are treated as purely ionic; the interactions between positively charged TM and negatively charged O ions stabilize the structure. A more precise treatment must allow for some mix of covalent and ionic bonding, and account for both electrons transferred to O atoms and the remaining TM valence electrons.

In the case of octahedral coordination, the $3d_{x^2-y^2}$ and $3d_{z^2}$ orbital lobes directed towards the octahedral vertices overlap with one of the three O_{2p} orbitals from each

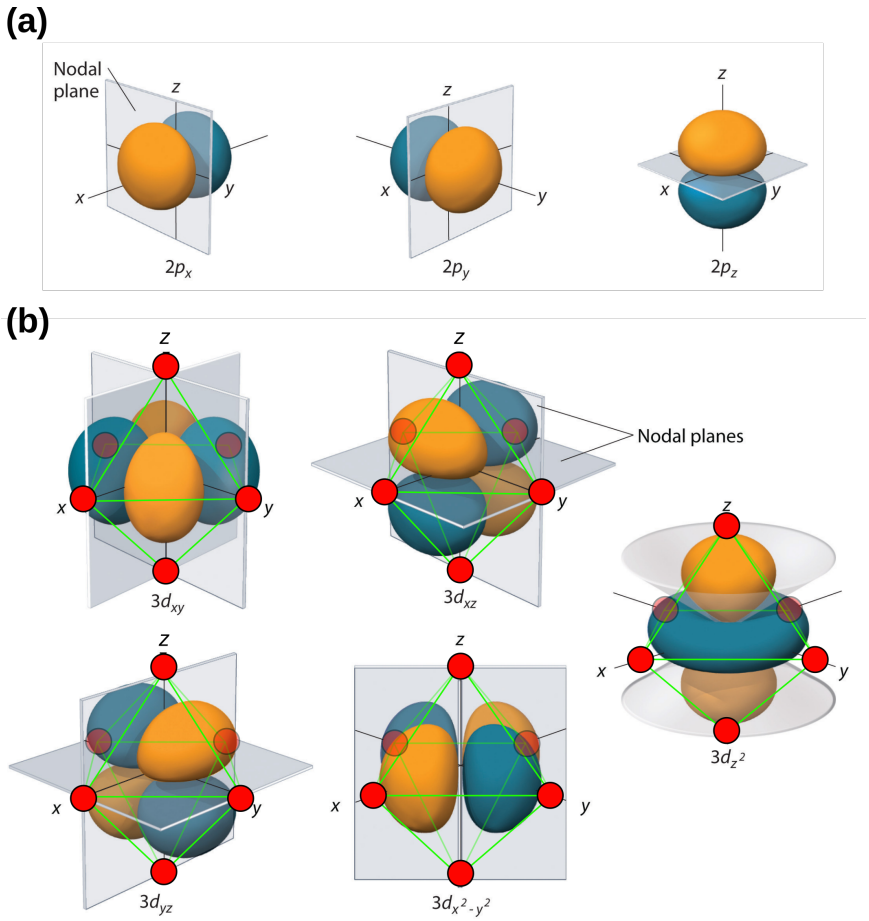

Figure 4.1: Cartesian representation of atomic orbitals. (a) $2p$ atomic orbitals, and (b) $3d$ atomic orbitals. Superimposed octahedra are shown with green lines along their edges. The red circles at the octahedral vertices represent O sites in octahedrally coordinated TM-O complexes where a TM ion occupies the octahedral center.

of the six vertices. As a result, their interactions are expected to be stronger. Conversely, the $3d_{xy}$, $3d_{xz}$, and $3d_{yz}$ orbital lobes directed towards interstitial regions do not overlap with any O_{2p} orbitals, resulting in weaker interaction. The resulting energy level diagram, based on the symmetry of each atomic orbital, is shown in Figure 4.2 (this figure was re-created from Ref. [30] with minor changes). The $3d_{xy}$, $3d_{xz}$, and $3d_{yz}$ orbitals are equivalent to one another with respect to the octahedral symmetry. As a result, any transformation that maps the octahedron onto itself will transform each of the three aforementioned orbitals in the same way, and the label t_{2g} is used to indicate the specific way in which they transform (it is called the irreducible representation). Additionally, due to being symmetrically equivalent, their energies

should be degenerate. Similarly, the $3d_{x^2-y^2}$ and $3d_{z^2}$ orbitals are labelled e_g due to their shared transformation properties, and are expected to have degenerate energies. It turns out that the O_{2p} orbitals share transformation properties with the e_g orbitals, but not with the t_{2g} orbitals. This can be most easily recognized with the observation that O_{2p} orbitals have lobes aligned along the same axes as those of the e_g orbitals so that any rotation, for example, will map them in the same way. The resulting hybridized orbitals preserve the symmetry of the respective atomic orbitals, thus, the e_g orbitals form a bonding/anti-bonding pair while the t_{2g} orbitals remain non-bonding. There are additional bonding/anti-bonding pairs formed from the interaction of the O_{2p} orbitals with the TM_{4s} and TM_{4p} orbitals, each having a_{1g} and t_{1u} symmetry, respectively. This results in a total of 6 bonding orbitals (three t_{1u}, one a_{1g}, and two e_g) that can accommodate twelve electrons. The exact order of the bonding orbitals is not known but, Griffith argues in Ref. [30], that because the $4s$ and $4p$ orbitals are less compact than the $3d$ orbitals, they should have stronger interactions leading to bonding and anti-bonding orbital energies laying below and above the respective e_g and e_g^* orbitals, as shown in the diagram of Figure 4.2. It will be shown later that U has a strong influence on the order of the resulting symmetry energy levels by virtue of only being applied to TM_{3d} orbitals.

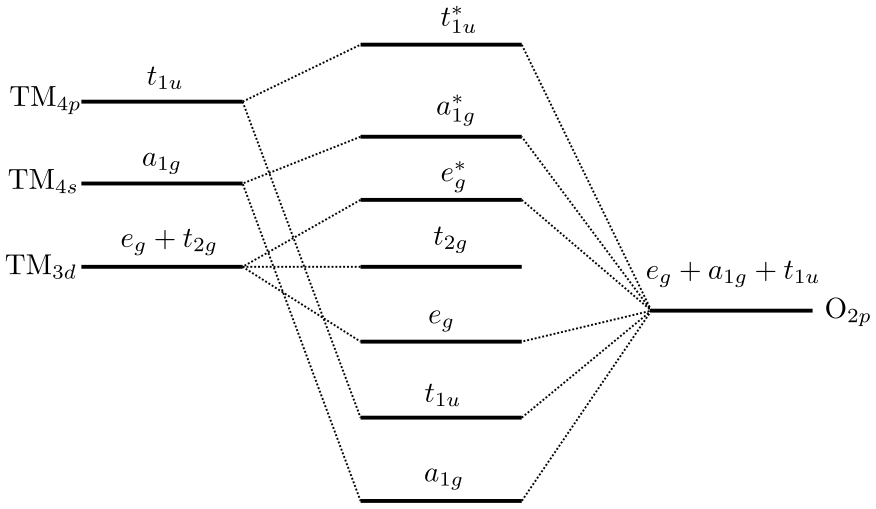

Figure 4.2: Energy level splitting in a TM-O_6 octahedral crystal field. The resulting symmetry orbitals are determined from the transformation properties of atomic orbitals with respect to the octahedral symmetry, and are respectively labelled.

The bonding orbitals are filled with O_{2p} electrons; assuming a filled $2p$ shell and

corresponding TM oxidation state, there are six available electrons per O atom, two in each of the p_x, p_y, and p_z orbitals. Since only one of the $2p$ orbitals is involved in the TM-O interaction — the one directed towards the octahedral center, each O atom contributes 2 electrons to the bonding orbitals, provided the $2p$ orbital in question is not shared with another site. In the NiO_2 stoichiometry for example, the TM:O ratio is 1:2 and each O site is coordinated by three Ni sites, thus each O_{2p} orbital contributes two electrons to the bonding orbitals. In total, there are twelve electrons per Ni site, filling the bonding orbitals exactly. In $LiNiO_2$ however, each of the three O_{2p} orbitals are shared with a Li site in addition to a Ni site. In a simple theory, Li atoms are treated as fully ionized, but in reality some electron charge is shared between Li and O ions. The consequence is a slight de-population of Ni-O bonding orbitals since all $2p$ electrons are not available to fill the TM-O e_g, t_{1u}, and a_{1g} bonding orbitals. This argument holds for each of the three Li-containing chemistries discussed in this Chapter.

The TM oxidation state is determined from its positive charge, assuming electrons have been transferred to fill the O_{2p} orbitals. For example, in $LiNiO_2$, four electrons must be transferred to O atoms; Li contributes one electron, thus Ni must contribute three, and is said to be in a 3+ oxidation state. The remaining number of electrons that can occupy the non-bonding t_{2g} and anti-bonding e_g^* TM-O orbitals is given by the number of TM valence electrons minus its oxidation state. For example, Ni has the $4s^2 3d^8$ valence configuration, thus Ni^{3+} has 7 electrons available to populate the t_{2g} and e_g^* orbitals.

There are two competing energy compensation mechanisms that determine how these orbitals are filled: the orbital energy, determined from the difference in energy between the t_{2g} and e_g^* orbitals, labelled Δ, and the exchange energy that is gained from having un-paired parallel spin electrons, labelled E_{ex}. The contribution of the latter is technically due to the quantum nature of electrons (identical spin-1/2 particles), but can be thought of in simple terms as minimizing the electrostatic repulsion between electrons by increasing their spatial separation, which occurs when they occupy different orbitals. Figure 4.3 shows two possible scenarios for a TM ion with 5 remaining $3d$ electrons. In the strong-field case shown in Figure 4.3(a), $\Delta_{SF} > E_{ex}$ so two down-spin electrons will be paired in the t_{2g} orbital. The electron

configuration is $(t_{2g})^5(e_g^*)^0$, with only 1 un-paired electron. Conversely, Figure 4.3(b) shows the weak-field case with $\Delta_{WF} < \Delta_{SF}$ and $\Delta_{WF} < E_{ex}$, so that electrons will preferentially occupy the higher energy e_g^* orbital rather than being paired in the t_{2g} orbital. The corresponding electron configuration is $(t_{2g})^3(e_g^*)^2$, with 5 un-paired electrons. In this case, the orbital energy per electron, Δ_{WF}, is less than the energy cost of pairing electrons, thus the energy is minimized by having each orbital occupied by a single electron. These two distinct configurations are referred to as low-spin (LS) and high-spin (HS), respectively, due to their net electron spins (total number of un-paired electrons). The spin-state is thus reflected in the spin magnetization, a quantity that is obtained from the pDOS as the difference between the up- and down-spin populations.

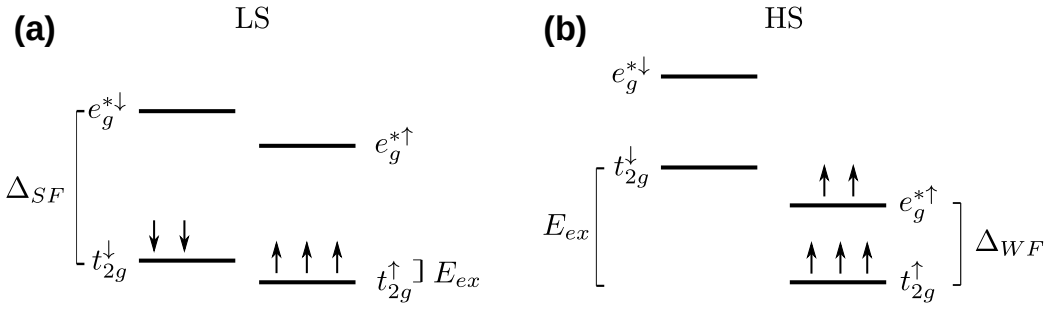

Figure 4.3: Energy level diagram for a TM ion in an octahedral crystal field. (a) Strong-field, Δ_{SF}, where a low-spin (LS) configuration is preferred, and (b) weak-field, Δ_{WF}, where a high-spin (HS) configuration is preferred.

It is important to realize, particularly when interpreting computed pDOS, that the bonding and anti-bonding orbitals are shared between the TM and O sites such that a certain amount of electron charge will reside on each of them. The lower laying t_{1u} and a_{1g} orbitals are expected to have charge mostly centered on the O atoms, while the e_g, t_{2g}, and e_g^* populations should be mostly concentrated on the TM ion, simply due to the compactness of the respective atomic orbitals that contribute to the TM-O symmetry orbitals. As a consequence, the TM is not ionized to its oxidation state and the TM pDOS will contain more electrons than only those in the t_{2g} and e_g^* levels. When U is applied, shifting the energies of TM_{3d} orbitals, the populations of shared symmetry orbitals centered on TM and O sites can change and the O magnetization can be non-zero. For this reason, the magnetization that will provide the closest value to the corresponding spin-state must be obtained from the total pDOS and not from

the TM pDOS.

As a final point of clarification regarding the pDOS analyses, the nature of the symmetry orbitals should be considered. In a pDOS computation, the l, m orbital decomposition is obtained, meaning that, for example, the contributions to the overall wavefunctions from all five $3d$ orbitals are separated. In the case of a perfectly symmetric octahedral crystal field, such as rocksalt-NiO, the e_g, t_{2g} and e_g^* orbitals are each purely composed of their respective $3d$ orbitals. In such a structure, each Ni atom is 6-fold coordinated to symmetrically equivalent O atoms and each O_{2p} lobe is equivalently directed towards a Ni site. In the case of lithiated structures, the perfect octahedral symmetry is broken, because each O_{2p} orbital must be shared between a TM and Li site. The octahedral crystal field remains, however the resulting symmetry orbitals are no longer separated into groups of pure atomic orbitals; the pDOS decomposition into the five $3d$ orbitals shows that the e_g, t_{2g}, and e_g^* orbitals are in fact each a superposition all five $3d$ atomic orbitals. For this reason, the pDOS presented here shows the total projection on each site, and the resulting crystal field symmetry orbitals are inferred based on energy ordering and bond character, obtained from the pCOHP.

4.3 $LiNiO_2$ — NiO_2

Figure 4.4 shows a depiction of the $LiNiO_2$ hexagonal unit cell. In Figure 4.4(a), only unique crystallographic sites are shown with the exception of the Li atom at the origin which is replicated once along the c-axis. In the hexagonal setting the unit cell contains 3 Li sites (green spheres), 3 Ni sites (grey spheres), and 6 O sites (red spheres). The primitive cell is rhombohedral and the three corresponding lattice vectors are superimposed within the hexagonal cell. The primitive cell contains 1 Li site, 1 Ni site, and 2 O sites. Figure 4.4(b) shows the octahedral coordination of Li and Ni with O. Green octahedra encompass Li sites, grey octahedra encompass Ni sites, and red spheres represent O atoms. In the hexagonal setting, the alternating triangular planes are obvious; O-Ni-O-Li planes are stacked along the c-axis. This structure is sometimes referred to as O3 because there are 3 unique O-Ni-O-Li layers in the unit cell. It is important to note that the Ni-O distance is shorter than the Li-O distance; the degree to which the O planes are closer to the Ni planes along the

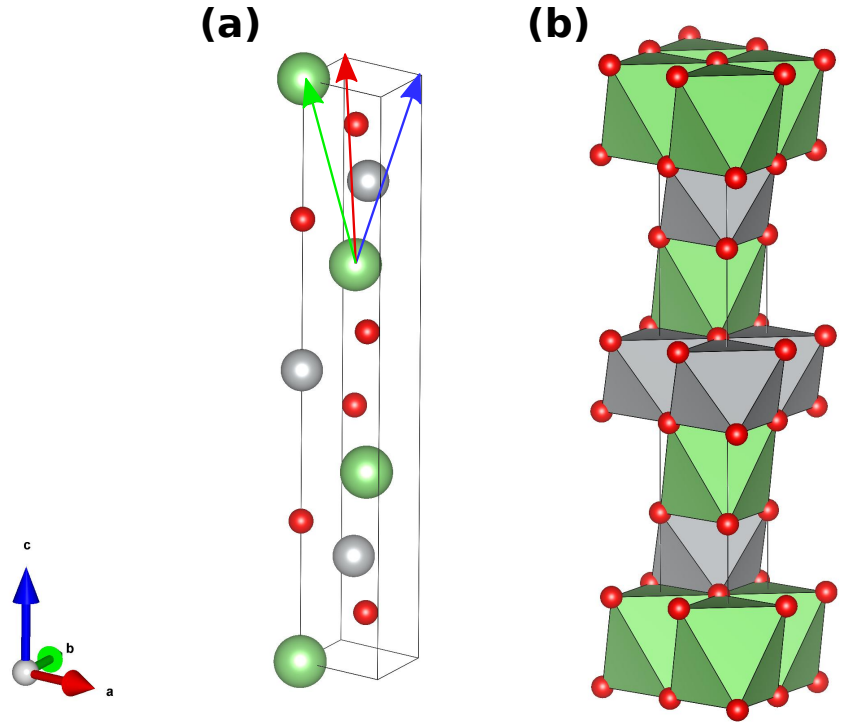

Figure 4.4: Depiction of the $LiNiO_2$ hexagonal unit cell. (a) Unique crystallographic sites (except that one Li is replicated along c-axis), where Li atoms are represented as green spheres, O atoms as red spheres, and Ni atoms as grey spheres. The thin red, green, and blue arrows within the hexagonal cell show the rhombohedral lattice vectors of the primitive cell. (b) Showing octahedral coordination within the unit cell. O atoms are represented by red spheres, Li sites are encompassed by green octahedra, and Ni sites are encompassed by grey octahedra.

c-axis is given by the crystallographic O_z parameter. If $O_z = 0.25$, then the Ni-O and Li-O distances would be the same. In the case of $LiNiO_2$, $O_z = 0.24$, giving an Ni-O distance shorter than Li-O by ~ 0.2 Å. The NiO_2 symmetry is identical to that of $LiNiO_2$ with the absence of Li being the only difference. The lattice and crystallographic parameters are of course different, but the O3 plane stacking is the same as $LiNiO_2$.

Figures 4.5 (a) and (b) show the a and c hexagonal lattice parameters for $LiNiO_2$ and NiO_2 as a function of U. The a lattice parameter for NiO_2 changes drastically compared to $LiNiO_2$; a decrease from 2.82 to 2.73 Å, $\sim 3\%$ change, compared to a decrease from 2.87 to 2.855 Å, $< 0.5\%$ change. The c-axis response to an increase in U is similar for both the lithiated and de-lithiated structures; $\sim 1\%$ increase. Figure

4.5 (c) shows the Ni-O distance as a function of U. This value encompasses the lattice parameters and the O_z parameter and is sensitive to the electronic structure. Interestingly, the Ni-O distance in $LiNiO_2$ changes by only 0.5%, whereas it changes by $\sim 2\%$ in NiO_2, as U goes from 0 to 8 eV. The structural changes in $LiNiO_2$ are minimal, while in NiO_2, the shortened Ni-O distance as U is increased leads to an appreciable contraction of the in-plane Ni-Ni distance, **a**. Overall, the structural changes occur very smoothly as a function of U, suggesting no abrupt transition within the electronic structure.

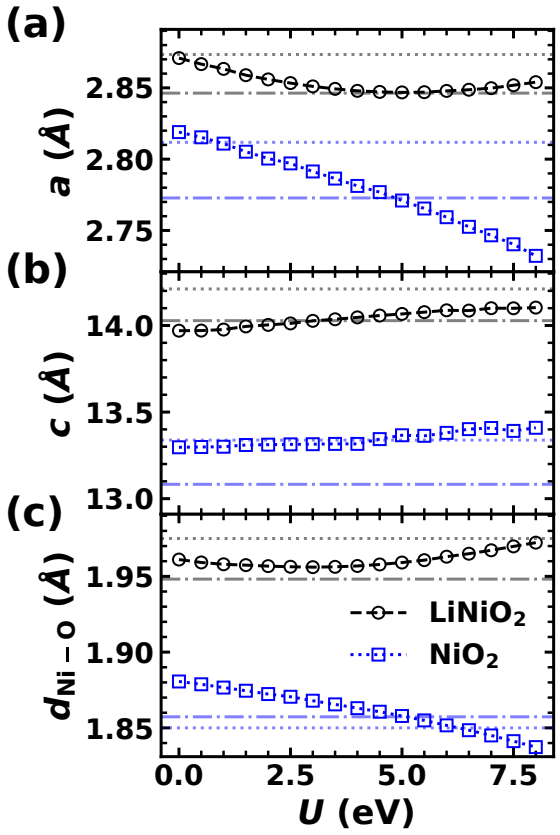

Figure 4.5: Structural parameters as a function of U for $LiNiO_2$ (black circles) and NiO_2 (blue squares). (a) the **a** hexagonal lattice vector, (b) the **c** hexagonal lattice vector, and (c) the Ni-O distance. The dotted lines correspond to experimental values and the dash-dotted lines correspond to computed values using SCAN+rVV10.

Figure 4.6 shows how the electronic structure of $LiNiO_2$ changes with U. The pDOS for Ni, O, and the total projection are shown in panels (a1), (a2), and (a3), respectively, for $U = 0, 4, 8$ eV. The up- and down-spin components of the pDOS are

shown to the right and left of the vertical center lines, respectively, and are labelled with up and down arrows. The energy is shifted so that the Fermi level, ε_f, lies at 0 eV. The pDOS below 0 eV thus corresponds to occupied states, while the pDOS above 0 eV corresponds to unoccupied states. Figures 4.6 (b1) and (b2) show the pCOHP of the Ni-O interaction for down- and up-spin components, respectively. The negative of the pCOHP is plotted so that bonding character is on the right (positive values) and anti-bonding character is on the left (negative values) of the vertical line, out of convention. The bond character obtained from the pCOHP can help determine which part of the pDOS corresponds to each of the ligand field bands. With $U = 0$, there are three bonding peaks in the pCOHP near -3 and -7 eV for both spin components, that correspond to the a_{1g}, t_{2u}, and e_g bonding bands which are shared between the Ni and O sites. The pDOS peaks around ε_f and just above it, between 0.5 and 1 eV, show well-defined anti-bonding character in the pCOHP, indicating that they belong to the e_g^* band. The t_{2g} peaks are between -2.5 and -0.5 eV and show moderate anti-bonding character in the pCOHP. This is in contrast to section 4.2 where it was argued that the t_{2g} bands should be non-bonding but, taken together with the electrostatic theory, the anti-bonding character of the t_{2g} band should be due to electrostatic repulsion.

As U is increased to 4 and 8 eV, there is a significant change in each of the Ni and O pDOS; the Ni states become incresingly spin-polarized with greater population at lower energies, and the O states also become increasingly polarized, but with opposite polarity, and a greater population at higher energies. This is reflected in the total pDOS where there is only a small difference between U values near ε_f, but a greater asymmetry between spin components as U is increased. The lowest energy peak for up-spin states with $U = 8$ eV has strong bonding character and thus corresponds to the $e_g^{\uparrow}$ bonding band. The $t_{2g}^{\uparrow}$ band between -1 and -2.5 , that is moderately anti-bonding, shifts to lower energy as U increases. When U reaches 8 eV, this band lies just above the $e_g^{\uparrow}$ band, between -5 and -6.5 eV and becomes slightly bonding. The $t_{2g}^{\downarrow}$ band, between -0.5 and -2 eV when $U = 0$ eV, is not shifted to lower energy as U is increased, but there is an increased low energy population. The corresponding pCOHP also shows, similarly to its up-spin counterpart, the $t_{2g}^{\downarrow}$ band going from moderately anti-bonding to moderately bonding, as U is increased from

0 to 8 eV. The difference in the response to U between the up- and down-spin $3d$ symmetry bands is due to the population of the $e_g^{\uparrow}$ band at the Fermi level; band energies are taken relative to highest occupied band, and since, for up-spin states, the $e_g^{\uparrow}$ remains partially occupied, the corresponding $3d$ symmetry bands are pushed to lower energy. Conversely, the $e_g^{\downarrow}$ band, which lies above ε_f, remains unoccupied as U is increased, thus the energy the occupied down-spin bands do not shift relative to ε_f. The gap between the highest occupied and lowest unoccupied $3d$ symmetry bands is approximately the same for both spin components, for each U. The pDOS obtained for $0 \leq U \leq 8$ is consistent with the LS Ni^{3+} crystal field configuration $(t_{2g})^6(e_g^{\uparrow})^1(e_g^{\downarrow})^0$. Despite a pronounced difference between the Ni and O pDOS, and an apparent increased spin-polarization, as U is increased, the charge states and net magnetization do not change. This point is discussed next.

Figure 4.7 (a1-a3) shows the electron charge of each ion computed with Bader charge partioning (black), and Mulliken (blue) and Loedwin (red) population analyses. All three methods show negligible changes in electron charge for each ion as U is increased from 0 to 8 eV. The relative magnitudes are different for each method by virtue of the way in which electrons are assigned to various atomic sites. Figure 4.7 (b) shows the total magnetization per Ni site as a function of U. Despite considerable spin polarization in the Ni and O pDOS with increasing U, the net magnetization remains unchanged. The fact that $m = 1.0\ \mu_B$ for U up to 8 eV indicates that Ni indeed remains in a LS state.

Figure 4.8 shows the Ni (a1), O (a2), and total (a3) pDOS, with corresponding down-spin (b1) and up-spin (b2) pCOHP for the Ni-O interaction in NiO_2. In this case, LS Ni^{4+} has the electron configuration $(t_{2g})^6(e_g^*)^0$. This is indeed observed in Figure 4.8; for example, with $U = 0$ eV, the total pDOS shows the unoccupied e_g^* bands above the Fermi level, and the t_{2g} bands, between -2 and 0 eV, with equal up- and down-spin populations, fully occupied. The unoccupied e_g^* bands show anti-bonding character in the pCOHP, as expected from Ligand Field Theory. Similarly to $LiNiO_2$, the t_{2g} band is expected to be non-bonding but shows moderate anti-bonding character in the pCOHP. The bonding a_{1g}, t_{1u}, and e_g bands occupy energies below -2 eV. As U is increased, the t_{2g} population closest to ε_f is depressed and shifts to lower energy. The bonding bands similarly shift to lower energy, but unlike $LiNiO_2$,

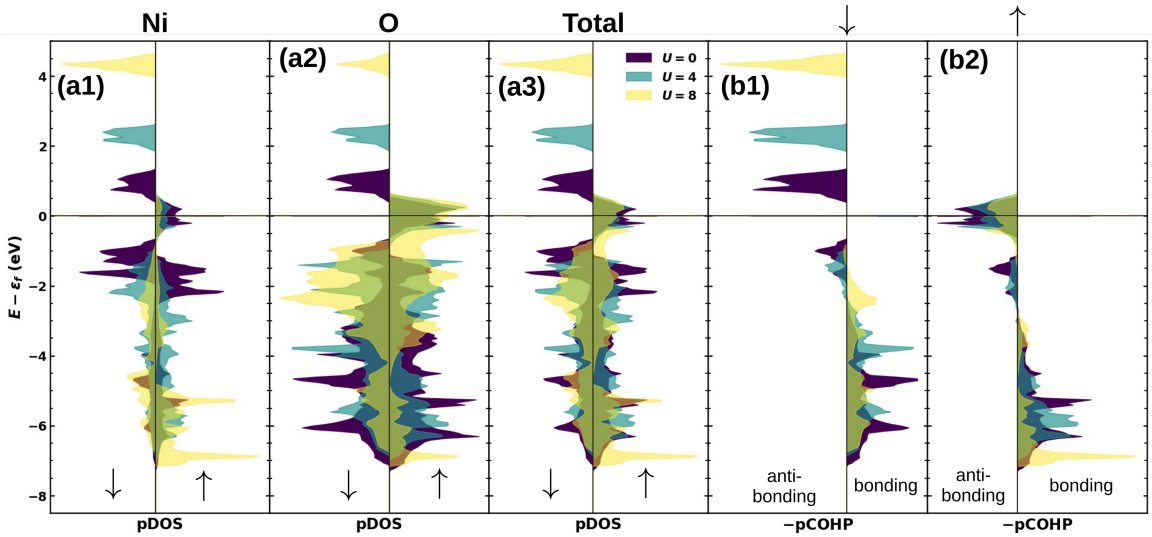

Figure 4.6: (a1) Ni projected DOS, (a2) O projected DOS, (a3) total projected DOS, (b1) down-spin and (b2) up-spin projected COHP for the Ni-O interaction in $LiNiO_2$. The up and down arrows denote electron spin components.

there does not appear to be a re-ordering of energy levels. For example, the lowest energy does not appreciably change shape as U increases from 0 to 8 eV. Hence, as the occupied t_{2g} and e_g symmetry bands are pushed to lower energy by U, the a_{1g} and t_{1u} bands are also shifted to lower energy. Without the presence of Li, there are 12 available electrons to fill the bonding bands. With the additional 6 electrons that fill the t_{2g} band, without a transition to a HS state, which is energetically unfavourable in this case, spin polarization cannot compensate the lowering of the $3d$ symmetry bands, thus all bands are simultaneously shifted to lower energy.

Figure 4.9 (a1) and (a2) show the net Ni and O atomic charges, respectively. Similarly to $LiNiO_2$, each of the three charge partioning method, Bader (black), Mulliken (blue), and Loedwin (red), do not show appreciable changes as U is increased from 0 to 8 eV. This is despite a significant shift of population in the Ni and O pDOS where lower energy states become increasingly centered on Ni sites, and higher energy states on O sites, as U increases. Figure 4.9 (b) shows that the net magnetization per Ni site remains exactly 0 for U up to 8 eV, reflecting the symmetry between spin components in the pDOS and the LS Ni^{4+} spin-state.

Figure 4.10 shows the average voltage between $LiNiO_2$ and NiO_2 as a function of U. The grey dotted line shows the experimental average voltage and the grey dash-dotted

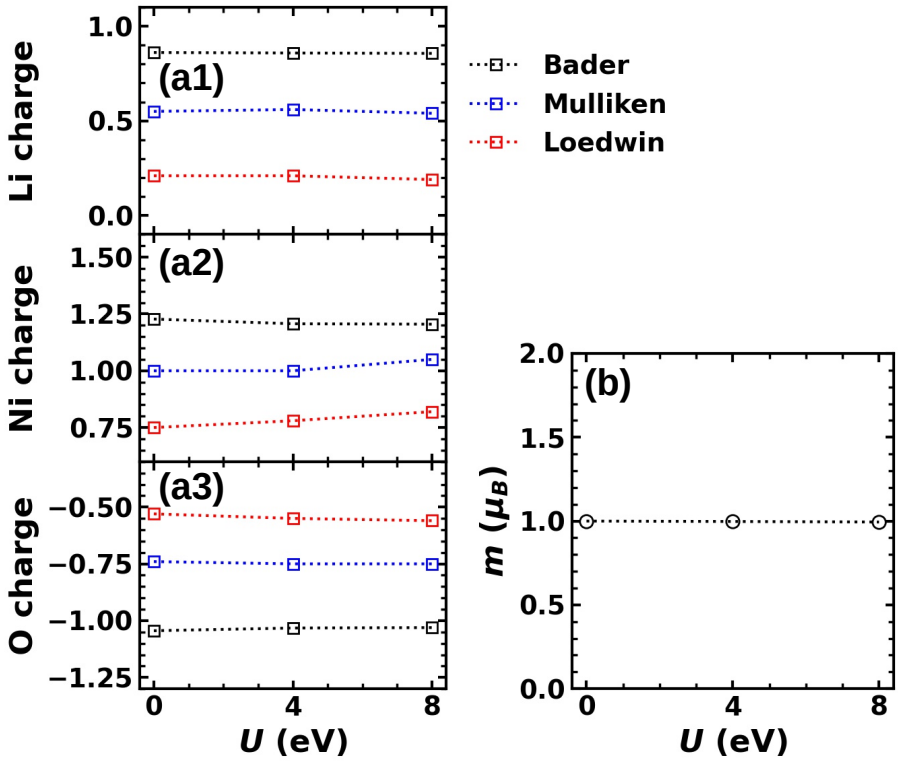

Figure 4.7: Charge transfer and magnetization in $LiNiO_2$. (a1) Li, (a2) Ni, and (a3) O net atomic charge versus U determined from Bader charge partitioning (black), Mulliken (blue), or Loedwin (red) orbital population analyses. (b) Total magnetization per Ni site versus U. Ni is expected to be in a LS state. Computed magnetizations with SCAN+rVV10 gave the LS state with $m = 1.0\ \mu_B$.

line shows the average voltage computed using SCAN+rVV10. GGA alone ($U = 0$) underestimates the average voltage by 0.8 V, while SCAN+rVV10 underestimates it by less than 0.2 V. If the best value of U was taken from this graph, it would be $U = 6.6$ eV. Interestingly, Ref. [86] found that $U = 6.4$ eV matched the experimental oxidation energy for the Ni^{2+}/Ni^{4+} redox reaction: $2NiO + O_2 \rightleftharpoons 2NiO_2$. However, this is not a reversible reaction; NiO_2 can only be obtained by de-lithiation of $LiNiO_2$. It is not known exactly how the experimental oxidation energy for this reaction was determined. Thus, the agreement between the U values for the oxidation energy and the average voltage could be real or could be due to a cancellation of errors between a fictitious experimental oxidation energy and dispersion corrections.

Since the average voltage is determined as the difference in energy between the lithiated and de-lithiated structures, a higher voltage indicates a greater energetic

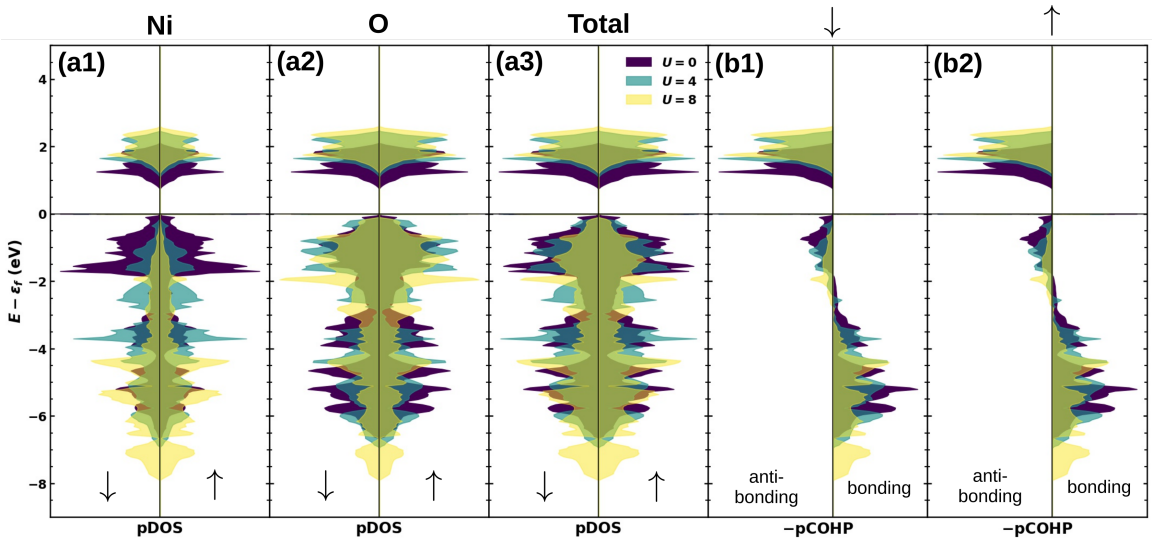

Figure 4.8: (a1) Ni projected DOS, (a2) O projected DOS, (a3) total projected DOS, (b1) down-spin and (b2) up-spin projected COHP for the Ni-O interaction in NiO_2. The up and down arrows denote electron spin components.

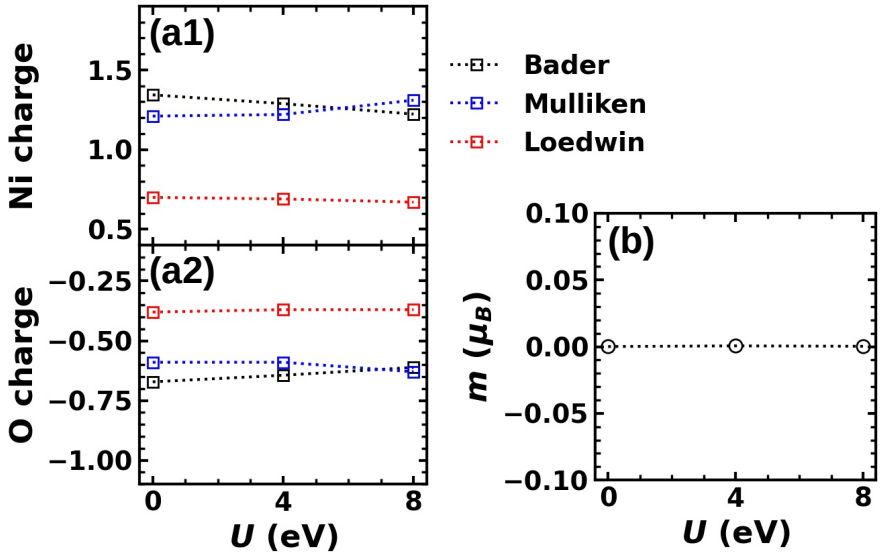

Figure 4.9: Charge transfer and magnetization in NiO_2. (a1) Ni and (a2) O net atomic charges versus U determined from Bader charge partitioning (black), Mulliken (blue), or Loedwin (red) population analyses. (b) Total magnetization per Ni site versus U. Ni is expected to be in a LS state. Computed magnetizations using SCAN+rVV10 gave the LS state with $m = 0.0\ \mu_B$.

separation between the two structures, with the lithiated one being preferred. The increase in voltage with larger U indicates that the NiO_2 energy increases by a greater amount compared to $LiNiO_2$. The presence of Li allows the e_g, t_{2g}, and e_g^* symmetry bands to respond differently to the TM_{3d} on-site potential, U; a slight de-population of bonding bands allows re-arrangement of occupancies to compensate for U. Conversely, in NiO_2, this compensation is restricted because all electrons are paired and ligand field bands filled. Additionally, the partial occupation of the e_g^* band in $LiNiO_2$ fixes the Fermi level, pushing the like-spin $3d$ bands to lower energy. The response of the electronic structure in NiO_2, paired with the absence of Li, which mediates lattice contraction, allows the Ni-O distance to shorten which contracts the in-plane distance, **a**, bringing positively charged Ni ions, and negatively charged O ions closer together, increasing the total energy. This smooth behaviour may at this point appear somewhat predictable given an understanding of the particular TM spin state, but similar analyses for (Li)CoO_2 and (Li)Mn_2O_4 will demonstrate otherwise.

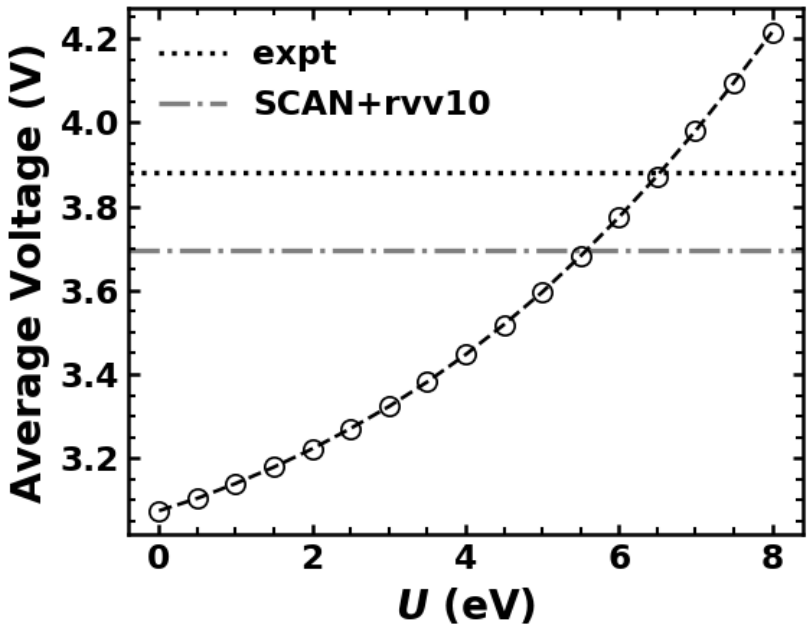

Figure 4.10: The average voltage for $LiNiO_2$ — NiO_2 as a function of U. The black dotted line shows the experimental value and the grey dash-dotted line shows the computed value using SCAN+rVV10.

4.4 $LiCoO_2$ — CoO_2

Figure 4.11 shows the crystal structure of $LiCoO_2$, which has the same O3 hexagonal plane stacking as $LiNiO_2$. Panel (a) depicts Li (green), Co (blue), and O (red) atoms as spheres to show unique crystallographic sites. The red, blue, and green arrows drawn within the hexagonal cell are lattice vectors of the rhombohedral primitive cell. Panel (b) shows the octahedral coordination by encompassing Co and Li sites with blue and green octahedra, respectively. The crystallographic parameters are thus of the same nature as those of $LiNiO_2$.

Figure 4.12 shows the CoO_2 primitive cell. This structure is slightly different than NiO_2, in which case the O3 structure is preserved from $LiNiO_2$ upon de-lithiation. The hexagonal symmetry is preserved upon de-lithiation, but CoO_2 adopts an O1 plane stacking; the same O-Co-O stacking is repeated in the out-of-plane direction. Each Co hexagonal plane, with two different O planes, above and below, is repeated along the **c**-axis. Thus, the **c**-axis represents the layer thickness, which to be compared on the same scale as $LiCoO_2$, must be tripled.

Figure 4.13 shows the dependence of the (Li)CoO_2 structural parameters on U. The **a** and **c** hexagonal lattice vectors (in the case of $LiCoO_2$, **c**/3 is plotted — the distance between two hexagonal Co planes, to be on the same scale as **c** for CoO_2) are shown in panels (a) and (b) respectively, while the Co-O distance is shown in panel (c). Data corresponding to $LiCoO_2$ is shown with black circles, and CoO_2 with blue squares. The dotted lines show experimental values and the dash-dotted lines show computed values obtained using SCAN+rVV10 rather than GGA+U. As U increases from 0 to 5.5 eV, the $LiCoO_2$ in-plane distance, **a**, contracts slightly, while the out-of-plane distance, **c**, expands, such that the Co-O distance remains constant. When U reaches 6 eV, there is an abrupt change in lattice parameters as the Co-O distance increases by more than 4%. Changes in the pDOS will show that this abrupt change in Co-O distance coincides with a transition from LS to HS. There is a similar abrupt change in Co-O distance in CoO_2 between $U = 2$ and 2.5, but by less than 1%. When U is increased beyond 6 eV, the Co-O distance increases rapidly, with a corresponding contraction of the in-plane distance, **a**. There is a abrupt decrease in **c** when $U = 7.5$ followed by an abrupt increase when $U = 8$ eV. However, the in-plane distance still varies smoothly. It will be shown later that there is a significant change

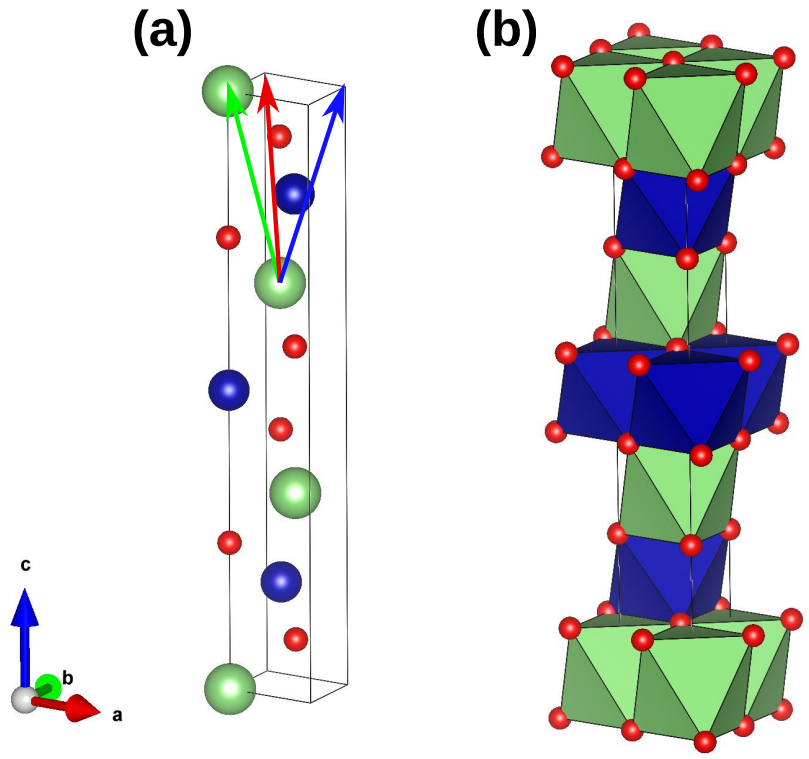

Figure 4.11: Depiction of the $LiCoO_2$ hexagonal unit cell. (a) Unique crystallographic sites (except that one Li is replicated along c-axis), Li atoms are represented by green spheres, O atoms by red spheres, and Ni atoms by grey spheres. The thin red, green, and blue arrows within the hexagonal cell show the rhombohedral lattice vectors of the primitive cell. (b) Octahedral coordination within the unit cell. O atoms are represented by red spheres, Li sites are encompassed by green octahedra, and Ni sites are encompassed by grey octahedra.

in the atomic charge when U changes from 7.5 to 8 eV.

Figure 4.14 (a1), (a2), and (a3) show the Co, O, and total pDOS, respectively, in $LiCoO_2$ for $U = 0, 5.5, 6, 8$ eV. The up- and down-spin components of the pDOS are shown on the right and left of the black vertical lines, respectively. The corresponding pCOHP for the Co-O interaction are shown in panels (b1) for the down-spin, and (b2) for the up-spin contributions, with bonding and anti-bonding characters shown on the right and left of the black vertical lines, respectively. The energies have been shifted so that the Fermi level, ε_f, is at 0 eV, shown with a black horizontal line. Co has the electron configuration $4s^2 3d^7$, and in $LiCoO_2$, has a 3+ oxidation state with 6 remaining valence electrons. The LS $(t_{2g})^6(e_g^*)^0$ configuration is observed experimentally in this octahedral crystal field.[59] In computations, it is sometimes

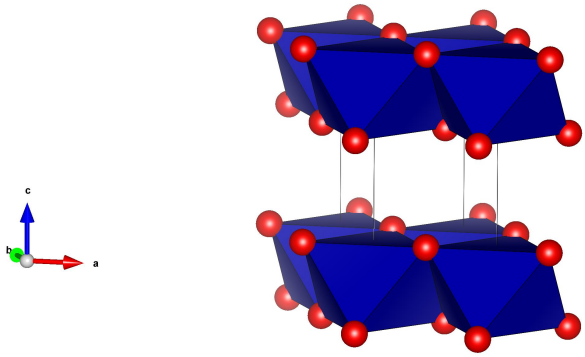

Figure 4.12: Depiction of the CoO_2 primitive cell. Co sites are encompassed by blue octahedra and O atoms are represented by red spheres. The primitive cell contains only one Co and two O atoms; to clearly demonstrate the layered structure, the Co site is reproduced along each lattice vector and the O atoms necessary to complete each octahedron are shown.

possible to converge different spin states and, for $LiCoO_2$, it is possible to converge both LS and HS Co for most values of U. The HS state becomes favorable for U just below 6 eV; the energy difference between the LS and HS states with $U = 5.5$ eV is $\Delta E_{\text{LS-HS}} \sim 500$ meV, whereas for $U = 6.0$ eV, $\Delta E_{\text{LS-HS}} \sim 50$ meV. In the following analysis, results are presented for the lowest energy spin state for each value of U.

With $0 \leq U \leq 5.5$ eV, the LS state is indeed observed, with the unoccupied e_g^* bands about 1 eV above ε_f, and the fully occupied t_{2g} bands showing peaks between -1 and -2 eV ($U = 0$) and -3 and -5 eV ($U = 5.5$). The energies of the up- and down-spin bands are identical because each band is either fully occupied, or completely unoccupied. For both $U = 0$ and 5.5 eV, the t_{2g} bands show moderate anti-bonding character, similar to $LiNiO_2$, that is likely due to electrostatic repulsion with the negatively charged O ions. The anti-bonding character of the e_g^* bands, above the Fermi level, is pronounced, as expected from Ligand Field Theory. The states between -7.5 and -2 eV for $U = 0$, and between -6 and -2 eV for $U = 5.5$ eV, for both the Co and O pDOS, show bonding character in the pCOHP, corresponding to the a_{1g}, t_{2u}, and e_g bands. Similarly to $LiNiO_2$, as U increases from 0 eV, the t_{2g} band is depressed to lower energy by U, which is seen just below ε_f in the total pDOS of panel (a3), and the band gap increases from 1 to 3 eV. When U is increased from 5.5 to 6 eV, there is a drastic change in the electronic structure coinciding with a change in spin-state.

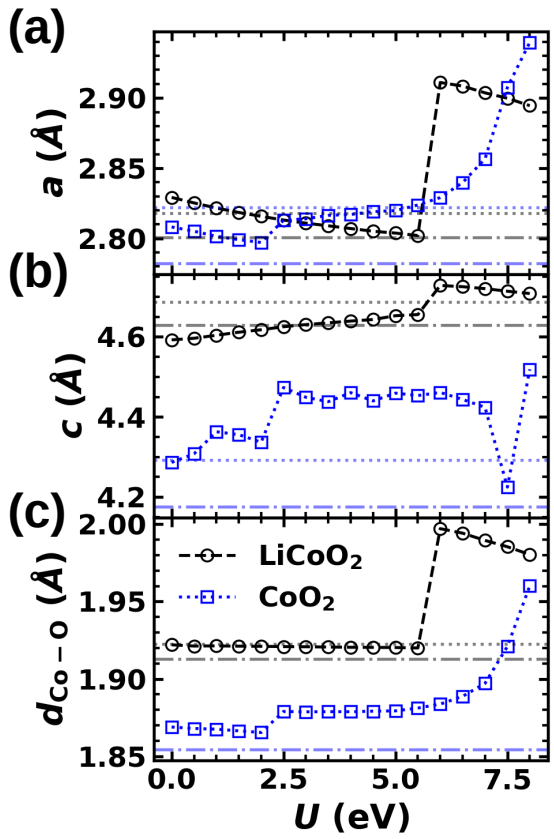

Figure 4.13: Structural parameters as a function of U for $LiCoO_2$ (black circles) and CoO_2 (blue squares). (a) the **a** hexagonal lattice vectors, (b) the **c** hexagonal lattice vectors — **c**/3 is shown for $LiCoO_2$, due to differences in plane stacking, to be comparable in magnitude to that of CoO_2, and (c) the Co-O distances. The dotted lines correspond to experimental values and the dash-dotted lines correspond to computed values using SCAN+rVV10.

HS Co^{3+} has the electron configuration $(t_{2g}^{\uparrow})^3(t_{2g}^{\downarrow})^1(e_g^{*\uparrow})^2(e_g^{*\downarrow})^0$. With $U > 5.5$ eV, three distinct peaks appear in the pDOS at the lowest energies. The pCOHP shows that one possesses bonding character, while the others are weakly bonding. These peaks are more prominent in the Co pDOS, indicating that they are mostly centered on the Co site and correspond to Co_{3d} orbitals. The $(e_g^{\uparrow})^2$ bonding band has the lowest energy, while the t_{2g} band is split in two; the sharpest, lower energy band is occupied only by up-spin electrons, while the third, higher energy band shows a corresponding peak in the down-spin pDOS, that is shifted to higher energy. Together, these two bands compose the $(t_{2g}^{\uparrow})^3(t_{2g}^{\downarrow})^1$ bands. Interestingly, the t_{2g} band shows weakly bonding character, as opposed to moderate anti-bonding character when $U <$

6 eV. This could be due to increased localization, which reduces electrostatic repulsion with O_{2p} orbitals. The bonding e_g band should not contribute to the TM spin-state, yet it appears fully polarized when $U \geq 6$ eV. Its down-spin counterpart must then occupy higher energies and be mostly centered on O sites. This occurs, similar to $LiNiO_2$, because the occupation of the $e_g^{*\uparrow}$ bands fixes ε_f, pushing the corresponding up-spin $3d$ bands to lower energies, splitting the spin components. This may be further facilitated by slightly de-populated bonding bands, due to shared electrons with Li sites, which creates degeneracy. The anti-bonding character just below ε_f in the up-spin pCOHP for $U \geq 6$ eV, which is not present in the down-spin pCOHP, then corresponds to the half-filled e_g^* band: $(e_g^{*\uparrow})^2(e_g^{*\downarrow})^0$. Interestingly, the e_g^* band, just below ε_f, shows only a small contribution from the Co site, but a larger one from the O site, perhaps indicating a strong degree of hybridization. The unoccupied down-spin states above ε_f show two distinct peaks when $U = 6$ eV that merge into a single, broad peak when $U = 8$. These correspond to the remaining unoccupied $t_{2g}^{\downarrow}$ and $e_g^{*\downarrow}$ bands. Thus, the electronic structure when $U \geq 6$ eV is consistent with HS Co^{3+}. The LS to HS transition can be understood as follows: the occupation of the e_g^* band must provide electron states just below ε_f, and, as a result, its energy eigenvalues cannot compensate the penalty from U, increasing the total energy. The HS configuration thus becomes preferred only when the t_{2g} and e_g bands are depressed by U to sufficiently low energies to compensate for the e_g^* partial occupation.

Figure 4.15 (a1), (a2), and (a3) show the Bader (black), Mulliken (blue), and Loedwin (red) charges, respectively. The increased Co and O charges when U is increased beyond 5.5 eV can explain, in simple terms, the expansion of the lattice vectors and increase in Co-O distance observed in Figure 4.13; a Co and O plane carrying more net charge will have greater site-to-site repulsion. The additional charge transfer may be due to the $e_g^{*\uparrow}$ band preferentially centered on O sites. Figure 4.15 (b) shows the magnetization per Co site, m, as a function of U. The transition from LS to HS is clearly represented, with m jumping from 0 to 4 μ_B when U is increased from 5.5. to 6 eV. HS Co^{3+} is expected to have $m = 4$ μ_B, in perfect agreement with the computational result. The change in band occupation paired with the change in magnetization clearly signify a transition from LS to HS.

Figure 4.17 (a1) and (a2) shows the Co and O pDOS, and panel (a3) shows the

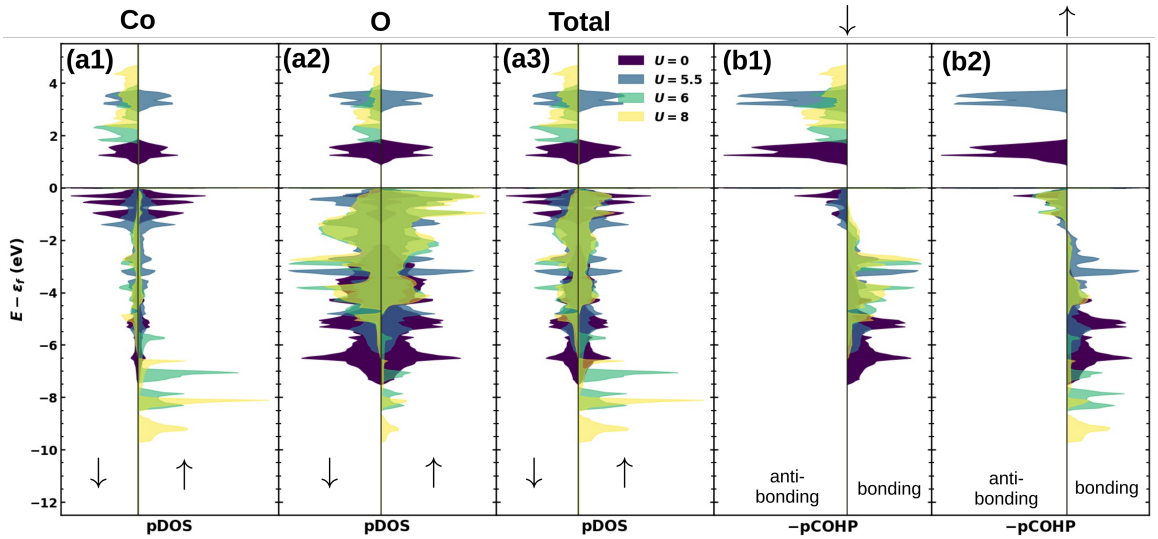

Figure 4.14: (a1) Co projected DOS, (a2) O projected DOS, (a3) total projected DOS, (b1) down-spin and (b2) up-spin projected COHP for the Co-O interaction in $LiCoO_2$. The up and down arrows denote electron spin components. Data is shown for $U = 0, 5.5, 6, 8$ eV.

total pDOS for CoO_2. Panels (b1) and (b2) show the corresponding pCOHP of the down- and up-spin components for the Co-O interaction in CoO_2 for $U = 0, 2, 2.5$, and 4 eV. Figure 4.16 shows the same computed quantities but for $U = 0, 4, 7.5$, and 8 eV. When $U \leq 2$ eV, there are electron state across ε_f, indicating metallic or semi-metallic character. In Figure 4.17, when U is increased from 2 to 2.5 eV, a band gap of about 0.5 eV opens, indicating a transition to semi-conducting. However, in Figure 4.16, when U is increased to 7.5 eV, some electron states re-appear at the Fermi level, and the material is again semi-metallic. The changes in electron states at the Fermi level in CoO_2 is in contrast to those of $LiCoO_2$ where semi-conduction persists for $0 < U < 8$ eV.

In CoO_2, Co assumes a 4+ oxidation state with the LS configuration $(t_{2g}^{\uparrow})^3(t_{2g}^{\downarrow})^2$. When $U \leq 2$ eV, the total pDOS from Figure 4.17 (a3) shows the $t_{2g}^{\uparrow}$ band just barely crossing ε_f, while a greater portion of the $t_{2g}^{\downarrow}$ band lies above ε_f. The e_g^* bands are above ε_f, between 1.5 and 3 eV, and have prevalent anti-bonding character in the pCOHP. When U is increased from 2 to 2.5 eV, the unoccupied $t_{2g}^{\downarrow}$ states are pushed completely above ε_f, opening the band gap. The Co and O pDOS in Figures 4.17 (a1) and (a2) show an increased population of the t_{2g} band on the O sites upon the band

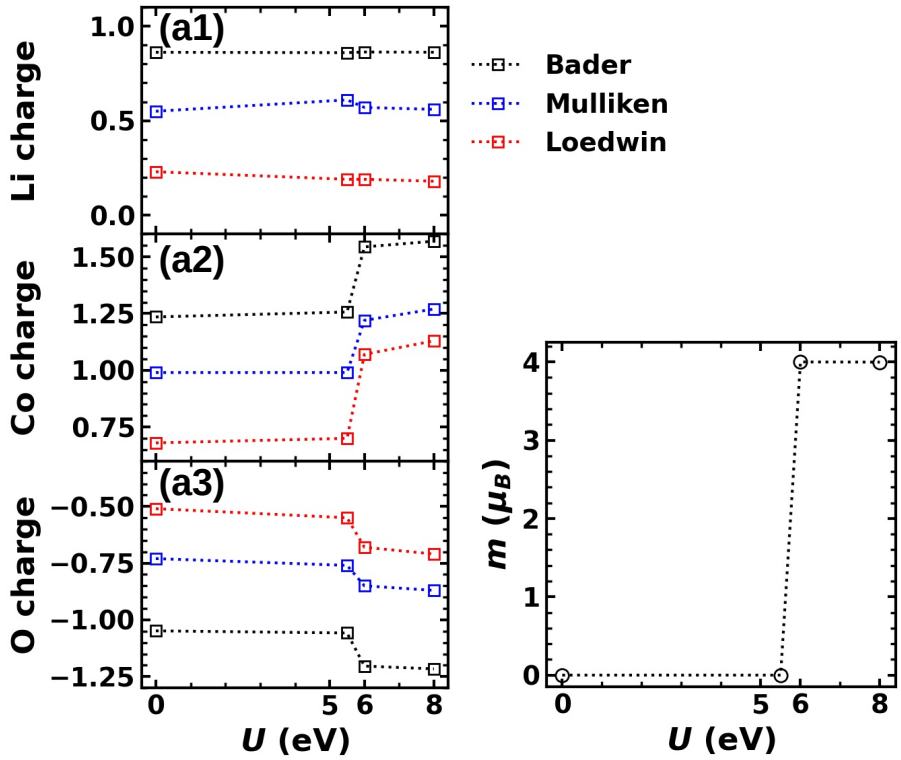

Figure 4.15: Charge transfer and magnetization in $LiCoO_2$. (a1) Li, (a2) Co, and (a3) O net atomic charges versus U determined from Bader charge partitioning (black), Mulliken (blue), or Loedwin (red) orbital population analyses. (b) Total magnetization per Co site versus U. Co is expected to be in a LS state. Computed magnetizations with SCAN+rVV10 gave the LS state with $m = 0.0\ \mu_B$.

gap opening. To compensate the charge, the a_{1g}, t_{1u}, and e_g bonding bands become increasingly centered on the Co sites. When U is increased from 2.5 to 4 eV, the band occupations do not change, but the unoccupied $t_{2g}^{\downarrow}$ states are pushed to higher energy, increasing the band gap to about 1 eV, such that the lowest unoccupied states are those of the $e_g^{*\uparrow}$ band. The total pDOS in Figure 4.16 (a3) shows that as U increases from 4 to 7.5 eV, the $e_g^{\uparrow}$ band, which shows strong bonding character, is depressed in energy to between -6.5 and -8 eV, while the $t_{2g}^{\uparrow}$ band is pushed down to between -4 and -6 eV. The broadened peak just above ε_f corresponds to the unoccupied $e_g^{*\uparrow}$ band, whose down-spin counterpart lies at higher energies. Since both e_g^{*} bands are unoccupied, Co is assumed to remain in a LS state up to 7.5 eV; this will be confirmed by Figure 4.18. Despite not changing spin-state, the energy splitting between spin components is much more pronounced with $U = 7.5$ compared to $U = 4$ eV, and

the way in which electrons are shared between Co and O clearly changes, and can be seen from their respective pDOS. When U reaches 8 eV, HS Co becomes energetically preferred. The peak depressed to lowest energy, near -10 eV, shows strong bonding character and corresponds to the $e_g^{\uparrow}$ band. The one directly above it, around -9 eV, shows weak bonding character and corresponds to the $t_{2g}^{\uparrow}$ band. The peak just above -6 eV in the down-spin total pDOS has a corresponding prominent peak in the pCOHP that shows strong bonding character, thus is associated with the $e_g^{\downarrow}$ band. The sharp peak in the up-spin component total pDOS, near -1 eV, shows strong anti-bonding character and thus corresponds to the $e_g^{*\uparrow}$ band. Only down-spin bands are unoccupied, with two sets of peaks above ε_f, corresponding to the $t_{2g}^{\downarrow}$ and $e_g^{*\downarrow}$ bands. Thus, the electronic structure when $U = 8$ eV is consistent with the HS configuration $(t_{2g})^3(e_g^*)^2$.

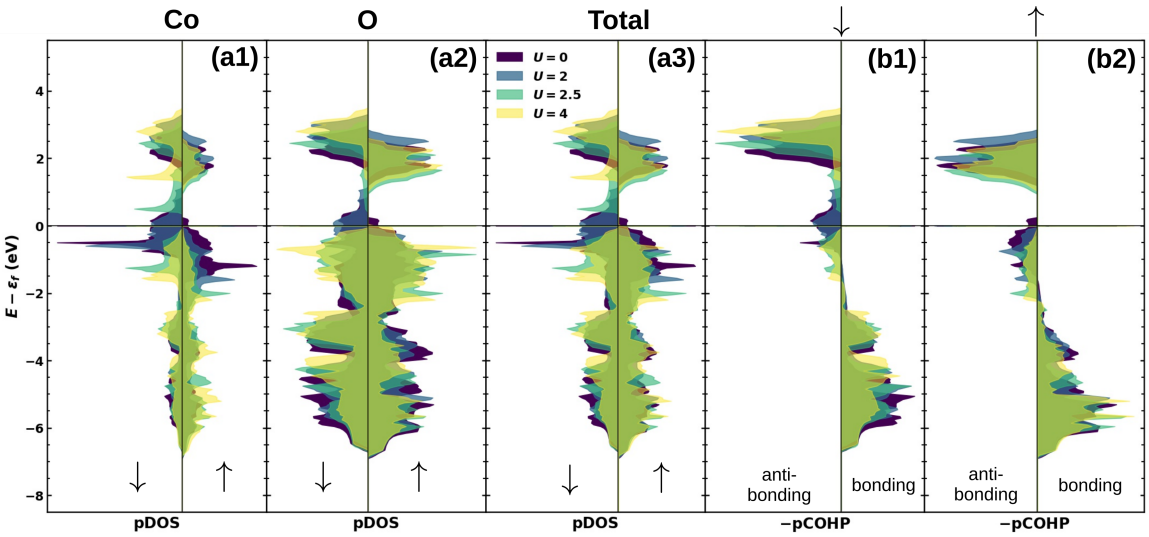

Figure 4.16: (a1) Co projected DOS, (a2) O projected DOS, (a3) total projected DOS, (b1) down-spin and (b2) up-spin projected COHP for the Co-O interaction in CoO_2. The up and down arrows denote electron spin components. Data is shown for $U = 0, 2, 2.5, 4$ eV.

Figures 4.18 (a1) and (a2) show the computed atomic charges centered on Co and O sites, respectively, as a function of U, obtained from Bader charge analysis (black) and Mulliken (blue) and Loedwin (red) population analyses. The (semi) metallic to semi-conducting transition when U is increased from 2 to 2.5 eV shows a small increase of charge transfer towards the Co sites. Comparatively, the LS to HS

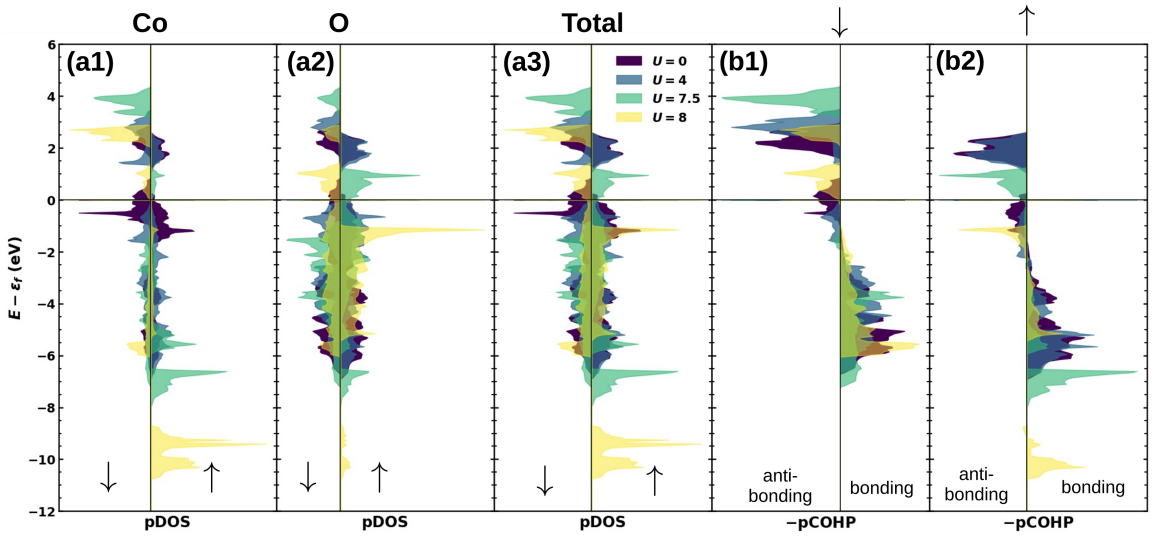

Figure 4.17: (a1) Co projected DOS, (a2) O projected DOS, (a3) total projected DOS, (b1) down-spin and (b2) up-spin projected COHP for the Co-O interaction in CoO_2. The up and down arrows denote electron spin components. Data is shown for $U = 0, 4, 7.5, 8$ eV.

transition when U is increased from 7.5 to 8 eV is accompanied by a much greater amount of charge transfer towards the Co site. Charge transfer towards the Co site was also seen in $LiCoO_2$ across the LS to HS transition. Recall that in Figure 4.16 (a2), the $e_g^{*\uparrow}$ band was mostly centered on the O site, similar to Figure 4.16 (a2), which may be responsible for the increase in electron charge around O sites. Figure 4.18 (b) shows the magnetization per Co site, m, as a function of U. LS Co^{4+} is expected to have $m = 1\mu_B$, which is indeed observed for $2 \leq U \leq 7.5$. For $U = 0$ eV, m is slightly less than one, which may due to the fact that there are electron states at the Fermi level for both spin components, whereas for $U = 2$, only down-spin electron states exist at ε_f (see Figure 4.17 (a3)). HS Co^{4+} is expected to have $m = 5\ \mu_B$, thus the LS to HS transition, between $U = 7.5$ and 8 eV, is clearly demonstrated in the magnetization. It is worth noting, that as in $LiNiO_2$ and $LiCoO_2$, as U increases, the local Co magnetization increases but is compensated by the local O magnetization. This enforces the point that symmetry orbitals resulting from the octahedral crystal field are shared between Co and O sites so that changes in one can be compensated by the other.

The average voltage for the $LiCoO_2$ — CoO_2 reaction as a function of U is shown

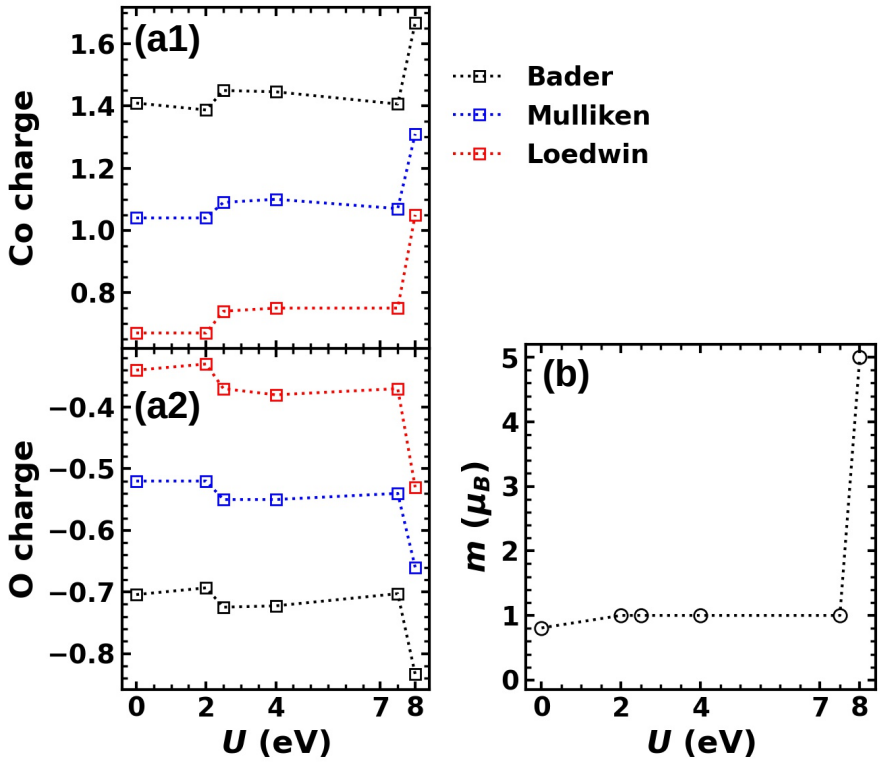

Figure 4.18: Charge transfer and magnetization in CoO_2. (a1) Co and (a2) O net atomic charges versus U determined from Bader charge partitioning (black), Mulliken (blue), or Loedwin (red) orbital population analyses. (b) Total magnetization per Co site versus U. Co is expected to be in a LS state. Computed magnetizations with SCAN+rVV10 gave the LS state with $m = 1.0\ \mu_B$.

in Figure 4.19. The features in this curve are each due to some transition in the electronic structure of either $LiCoO_2$ or CoO_2; the cusp at $U = 2$ eV is due to the (semi) metallic to semi-conducting transition in CoO_2, the increase in voltage starting at $U = 5.5$ eV is due to the LS to HS transition in $LiCoO_2$, and the steep increase in voltage between $U = 7.5$ and 8 eV is due to the LS to HS transition in CoO_2. A larger average voltage indicates that $LiCoO_2$ is more thermodynamically preferred, i.e., there is a greater energy difference between the two compositions. It is interesting that the average voltage only increases near the experimental value once the HS state becomes preferred in $LiCoO_2$, which is not the experimentally observed spin state. The sample temperature during the electronic structure measurements of $LiCoO_2$ from Ref. [59] was not stated, thus, if the measurements were performed at ambient conditions, it is possible that the HS state of Co^{3+} may be preferred near 0 K. The

spin state of CoO_2 has not been experimentally determined; CoO_2 is highly unstable upon delithiation making careful characterization difficult. Nevertheless, within the GGA+U formalism, it is not possible to obtain an average voltage in agreement with experiment for LS Co in $LiCoO_2$. The computed average voltage using SCAN+rVV10 is in excellent agreement with experiment, and predicted LS Co^{3+} in $LiCoO_2$. The oxidation reaction enthalpy quoted in Ref. [86] leads to a "best" U value of 3.3 eV for the $Co^{2+} \rightleftharpoons Co^{2.7+}$ oxidation reaction. This value of U leads to an average voltage underestimated by ~ 0.7 V. The results of this section indicate the possibility that the GGA+U formalism may not be appropriate for Co containing Li oxides.

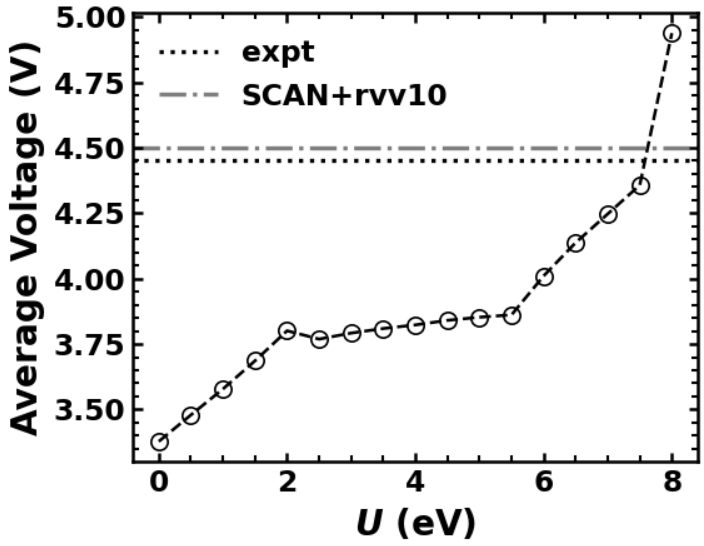

Figure 4.19: The average voltage for $LiCoO_2$ — CoO_2 as a function of U. The black dotted line shows the experimental value and the grey dash-dotted line shows the computed value using SCAN+rVV10.

4.5 $LiMn_2O_4$ — Mn_2O_4

Figure 4.20 (a) shows the primitive cell for $LiMn_2O_4$, while panel (b) shows two repetitions of the primitive cell along each lattice vector. Mn sites sites are encompassed by purple octahedra, Li sites by green tetrahedra, and O atoms are represented by red spheres. This is a spinel structure characterized by tetahedrally coordinated Li sites within 3-dimensional channels of a Mn-O sub-lattice. Each O site is coordinated with three Mn sites and one Li site. The primitive lattice vectors point towards the faces of a larger cubic cell, this is thus an *fcc* lattice. The de-lithiated crystal structure of Mn_2O_4 is the same as its lithiated counterpart, except of course with the absence of Li.

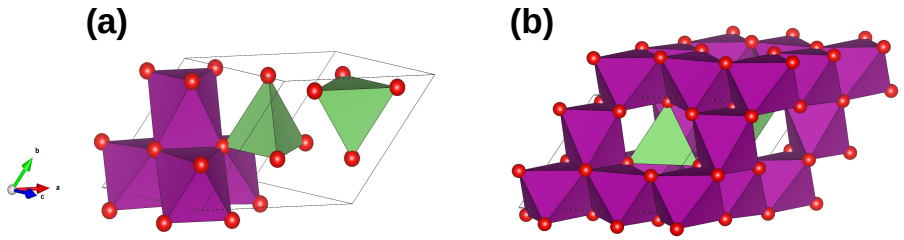

Figure 4.20: Depiction of the $LiMn_2O_4$ unit cell. (a) The primitive cell, and (b) two repetitions of the primitive cell along each lattice vector. Mn sites are encompassed by purple octahedra, Li sites are encompassed by green tetrahedra, and O atoms are represented by red spheres.

Figure 4.21 shows the structural dependence of (Li)Mn_2O_4 on U. In panel (a), the primitive lattice vectors were converted to the conventional cubic setting to compare with experimentally quoted values. In panel (b), the corresponding Mn-O bond lengths are shown. The black circles correspond to $LiMn_2O_4$ while the blue squares to Mn_2O_4. The dotted lines correspond to the experimental values and the dash-dotted lines to computed values obtained using SCAN+rVV10. In both cases the grey and light blue colors correspond to $LiMn_2O_4$ and Mn_2O_4, respectively.

In $LiMn_2O_4$, there is a abrupt increase in the lattice vectors, with a corresponding increase in the Mn-O distance, between $U = 1.5$ and 2 eV. Electronic structure analysis, discussed later, will show that this corresponds to a transition from LS to HS. The lattice vectors are underestimated compared to the experimental value when $U \leq 1.5$ eV and overestimated when $U \geq 2$ eV, while the Mn-O distance

is overestimated for all values of U. Comparatively, SCAN+rVV10 underestimates the lattice vector lengths but gives a Mn-O distance in excellent agreement with experiment. In Mn_2O_4, the lattice vectors are overestimated for all values of U, with $U = 0$ eV giving the best agreement. $U = 0$ eV gives an Mn-O distance in excellent agreement with experiment, while larger values U progressively overestimate it. The lattice vectors in Mn_2O_4 are also underestimated by SCAN+rVV10, however the agreement is much better compared with that of $LiMn_2O_4$. As a result, the Mn-O distance is underestimated by SCAN+rVV10, but only by 1%.

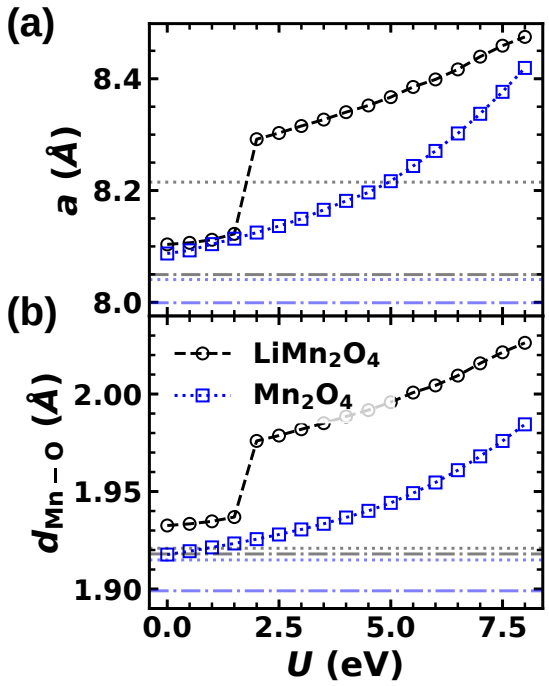

Figure 4.21: Structural parameters as a function of U for $LiMn_2O_4$ (black circles) and Mn_2O_4 (blue squares). (a) the cubic lattice vector length, **a**, and (b) the Mn-O distance. The dotted lines correspond to experimental values and the dash-dotted lines correspond to computed values using SCAN+rVV10.

Mn has the electron configuration $4s^2 3d^5$. In $LiMn_2O_4$, the filling of O_{2p} orbitals requires one electron from Li and 3.5 electrons from Mn, leaving Mn in an average oxidation state of 3.5+. The LS octahedral crystal field configuration is then $(t_{2g}^{\uparrow})^3(t_{2g}^{\downarrow})^{0.5}(e_g^*)^0$. But, there is a distinctive structural difference compared with $LiNiO_2$ and $LiCoO_2$: the Li ions are tetrahedrally, not octahedrally, coordinated, and they occupy 3-dimensional channels rather than 2-dimensional planes. Tetrahedrally

coordinated Li ions are not aligned with the TM-O axes, nor the O_{2p} orbitals, thus the influence of Li on the Mn-O bonding bands should be reduced. The Mn:O ratio is 1:2, which provides 12 electrons to fill the 12 spin-dependent bonding bands, thus should be less sensitive to U, as was seen in NiO_2 and CoO_2. However, the valence bands still provide electronic degrees of freedom that may be sensitive to U.

Figure 4.22 (a1), (a2), and (a3) show the Mn, O, and total pDOS, respectively, for $U = 0, 1.5, 2, 6$ eV, while panels (b1) and (b2) show the corresponding pCOHP for the Mn-O interaction. With $U = 0$, the up-spin total pDOS peaks between -1 and -3 eV correspond to a fully occupied $t_{2g}^{\uparrow}$ band. The $t_{2g}^{\downarrow}$ band is partially occupied, with most of its population above the Fermi level, consistent with the LS configuration. Both spin components of the t_{2g} band show moderate anti-bonding character, which is attributed to electrostatic repulsion. The $e_g^{*\uparrow}$ and $e_g^{*\downarrow}$ bands correspond to those peaks completely above ε_f for both spin components, which are both fully unoccupied, also consistent with the LS Mn configuration. When U is increased to 1.5 eV, the $t_{2g}^{\uparrow}$ band is shifted to lower energy, between -2 and -3.5 eV, but the LS configuration remains energetically preferred so the $t_{2g}^{\downarrow}$ partial occupation at the Fermi level remains unchanged. However, in the LS configuration, as U increases, the $t_{2g}^{\uparrow}$ band shifts to lower energy and the unoccupied $e_g^{*\uparrow}$ band shifts closer to ε_f, foreshadowing the transition to HS. For both $U = 0$ and 1.5 eV, there is little difference in the bonding a_{1g}, t_{1u}, and e_g bands, and the overall populations centered on the Mn and O sites do not vary.

There is an abrupt change in the pDOS when U increases from 1.5 to 2 eV; the $e_g^{*\uparrow}$ band, unoccupied with $U < 2$ eV, becomes partially occupied while the $t_{2g}^{\downarrow}$ band, partially occupied with $U < 2$ eV, becomes unoccupied. This represents a transition from LS to HS with the electron configuration $(t_{2g}^{\uparrow})^3(t_{2g}^{\downarrow})^0(e_g^{*\uparrow})^{0.5}(e_g^{*\downarrow})^0$. The occupied $e_g^{\uparrow}$ and $t_{2g}^{\uparrow}$ bands are shifted to lower energy, while there is an increased population of down-spin electrons centered on the O sites within the bonding bands energy range. The change in the electronic structure is not as drastic as with $LiCoO_2$, for example, because the LS to HS transition involves only the promotion of half an electron from the t_{2g} to e_g^* band.

Figure 4.23 shows the Bader charge (black), and Mulliken (blue) and Loedwin (red) populations in panels (a1), (a2), and (a3), respectively. The total magnetic

moment per Mn, m, is shown panel (b). There is a small transfer of charge from Mn to O sites when U goes from 1.5 to 2 eV due to the population of the higher energy $e_g^{*\uparrow}$ band. The Mn magnetic moment also abruptly changes from 2.5 to 3.5 μ_B, as a result of promoting half an electron from $t_{2g}^{\downarrow}$ to $e_g^{*\uparrow}$ in the transition from LS to HS.

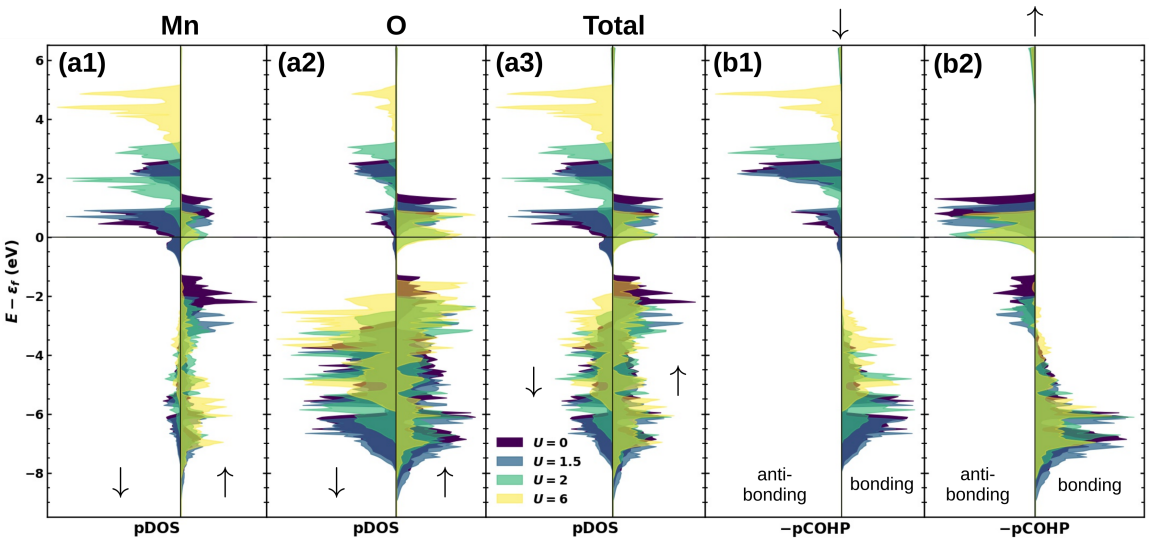

Figure 4.22: (a1) Co projected DOS, (a2) O projected DOS, (a3) total projected DOS, (b1) down-spin and (b2) up-spin projected COHP for the Mn-O interaction in $LiMn_2O_4$. The up and down arrows denote electron spin components. Data is shown for $U = 0, 1.5, 2, 6$ eV.

In Mn_2O_4, Mn is present in the 4+ oxidation state. This leaves 3 electrons in the t_{2g} band, thus the $(t_{2g}^{\uparrow})^3(t_{2g}^{\downarrow})^0(e_g)^0$ configuration is the only possibility. Figures 4.24 (a1), (a2), and (a3) show the Mn, O, and total pDOS, respectively, for $U = 0, 4, 8$, and panels (b1) and (b2) show the corresponding pCOHP for both spin components of the Mn-O interaction. With $U = 0$ eV, the $t_{2g}^{\uparrow}$ band, with moderate anti-bonding character, is fully occupied, just below the Fermi level, and is centered mostly on the Mn sites. The $t_{2g}^{\downarrow}$ band is empty, spanning the 1 to 2.5 eV range, as are both e_g^* bands which span energies between 2 to 3 eV (up-spin), and 3.5 to 4.5 eV (down-spin). The a_{1g}, t_{1u}, and e_g bonding bands span the -6.5 to -1.5 eV energy range with spin component energies shifted by about 0.5 eV due to the fully polarized t_{2g} band. As U is increased, occupied bands with $3d$ character are shifted to lower energies; the Mn pDOS clearly shows a decrease in population just below ε_f with an increase in population below -4 eV ($U = 4$) and -6 eV ($U = 8$). The prevalent peaks below

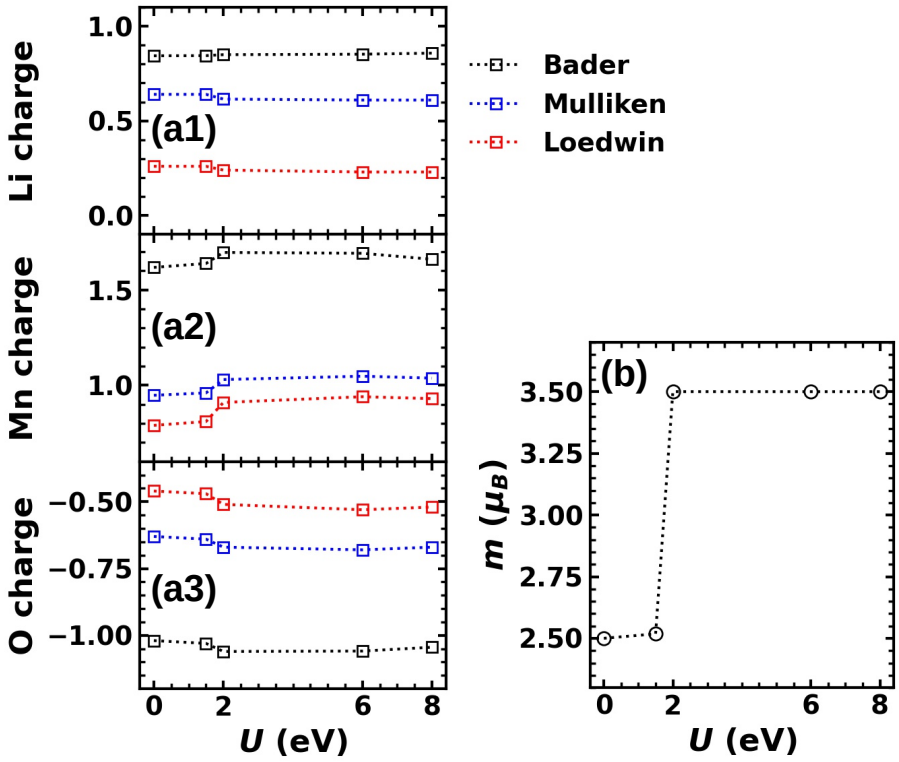

Figure 4.23: Charge transfer and magnetization in $LiMn_2O_4$. (a1) Li, (a2) Mn, and (a3) O net atomic charges versus U determined from Bader charge partitioning (black), Mulliken (blue), or Loedwin (red) orbital population analyses. (b) Total magnetization per Mn site versus U. Mn is expected to be in a LS state. Computed magnetizations with SCAN+rVV10 gave the LS state with $m = 2.5\ \mu_B$.

-6 eV when $U = 8$ eV shows bonding character in the pCOHP, and correspond to the occupied t_{2g} and e_g bands. As a result, the e_g band becomes spin-polarized as U increases; the $e_g^{\downarrow}$ band is hardly influenced by U because it is fully occupied and has no other occupied $3d$ bands at higher energies.

Figures 4.25 (a1) and (a2) shows the Mn and O atomic charges computed from Bader charge partitioning (black) and Mulliken (blue) and Loedwin (red) population analyses. There is a negligible change in charge transfer for $0 \leq U \leq 8$. Figure 4.25 (b) shows that the total magnetization per Mn site, m, equals 3 μ_B for all values of U, consistent with the t_{2g}^3 electron configuration. Hence, the local increase in spin polarization on Mn sites is exactly compensated for by O sites since the response of the electronic structure to U is constrained by the spin-state.

Figure 4.26 shows the average voltage between $LiMn_2O_4$ and Mn_2O_4. The black

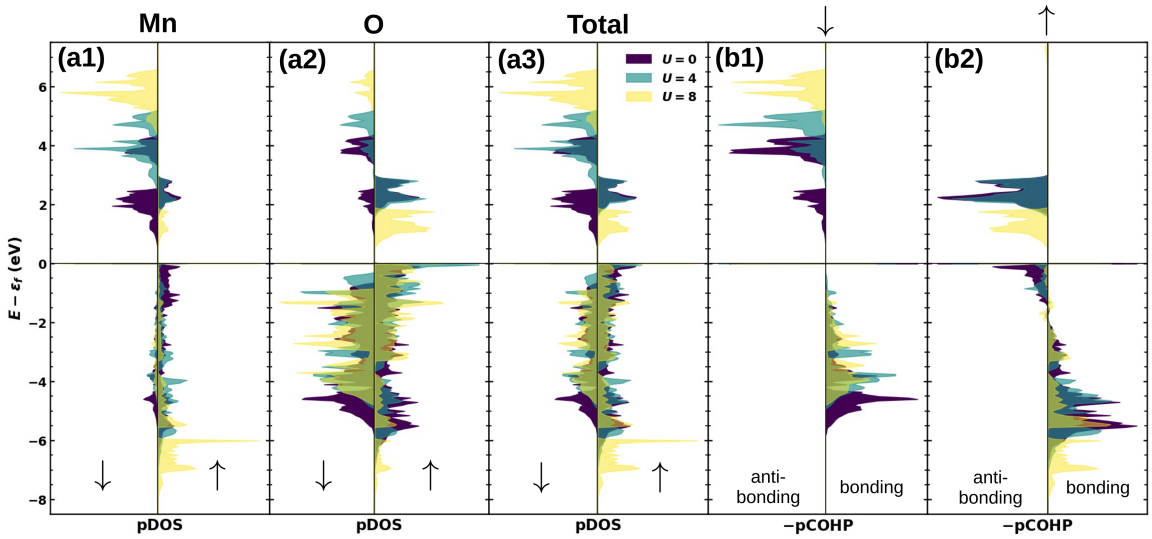

Figure 4.24: (a1) Co projected DOS, (a2) O projected DOS, (a3) total projected DOS, (b1) down-spin and (b2) up-spin projected COHP for the Mn-O interaction in Mn_2O_4. The up and down arrows denote electron spin components. Data is shown for $U = 0, 4, 8$ eV.

dotted line shows the experimental value and the grey dash-dotted line shows the computed value obtained using SCAN+rVV10, instead of GGA+U. For $U \leq 1.5$ eV, LS Mn is preferred in $LiMn_2O_4$ and is penalized to a greater extent by U compared to Mn_2O_4, hence the voltage decreases. For $U \geq 2$ eV, HS Mn in $LiMn_2O_4$ is penalized by U to a lesser extent than Mn in Mn_2O_4, thus the voltage increases. The value $U = 6.25$ gives an average voltage in agreement with experiment. Ref. [86] found values of $U = 3.8, 4.0, 3.5$ eV for the Mn^{2+} to $Mn^{2.7+}$, Mn^{2+} to Mn^{3+}, and Mn^{2+} to Mn^{4+} oxidation reactions, respectively. All of these values underestimate the Li intercaltion potential; with $U = 4$ eV, the average voltage is 3.7 V, less than the experimental value by 0.45 V. In this case, SCAN+rVV10 favours LS Mn in $LiMn_2O_4$ and underestimates the average voltage by 0.45 V.

4.6 Summary and remarks

This Chapter presented an analysis of the dependence of structural parameters, electronic structure, and electrochemistry on the U parameter within the GGA+U formalism applied to (Li)NiO_2, (Li)CoO_2, and (Li)Mn_2O_4. Changes in TM spin-state

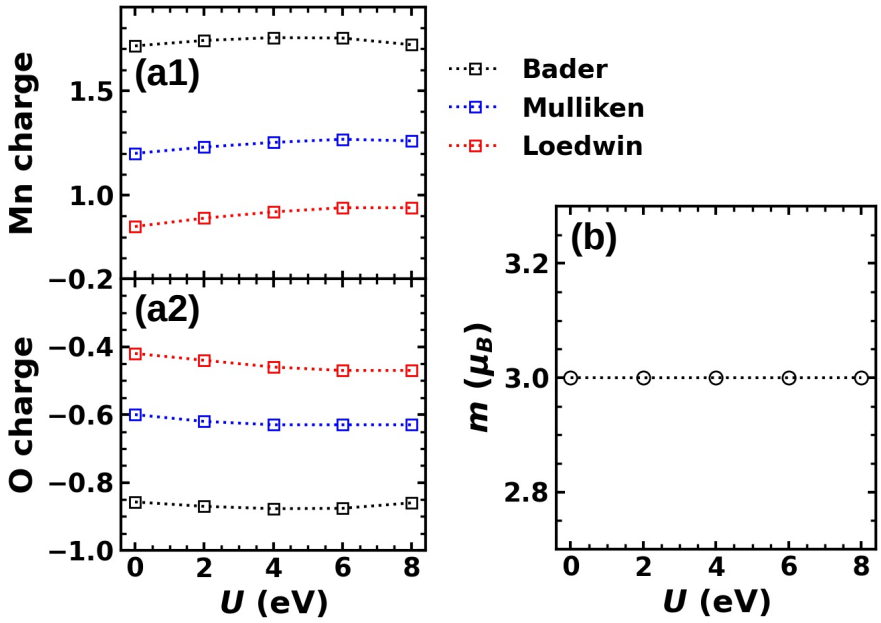

Figure 4.25: Charge transfer and magnetization in Mn_2O_4. (a1) Mn and (a2) O net atomic charges versus U determined from Bader charge partitioning (black), Mulliken (blue), or Loedwin (red) orbital population analyses. (b) Total magnetization per Mn ion versus U. Mn is expected to be in a LS state. Computed magnetizations with SCAN+rVV10 gave the necessary spin state with $m = 3.0\ \mu_B$.

were identified for $LiCoO_2$ at $U = 6$ eV, CoO_2 when $U = 8$ eV, and $LiMn_2O_4$ when $U = 2$ eV. It is possible that $LiNiO_2$ and NiO_2 would undergo a transition from LS to HS at U values greater than 8 eV, but this was not considered here. CoO_2 additionally transitions from metallic to semi-conducting when $U = 2.5$ eV, and again to metallic when $U = 7.5$. Each of these transitions manifest a clear signature in the average voltage between the lithiated and de-lithiated structures. The U values from Ref. [86] which gave oxidation energies in agreement with experiment also gave good agreement for the $LiNiO_2$ — NiO_2 average voltage, but underestimated those of $LiCoO_2$ — CoO_2 and $LiMn_2O_4$ — Mn_2O_4 by 0.7 V and 0.45 V, respectively.

With the understanding that different oxidation states will respond differently to U, and that intercalation potentials are determined from the change in TM oxidation state, it is not surprising that a single U value would not be appropriate for different oxidation reactions of a given TM. The presence of Li in the TM oxides considered here modifies the electronic structure which facilitates shifting of crystal field bands

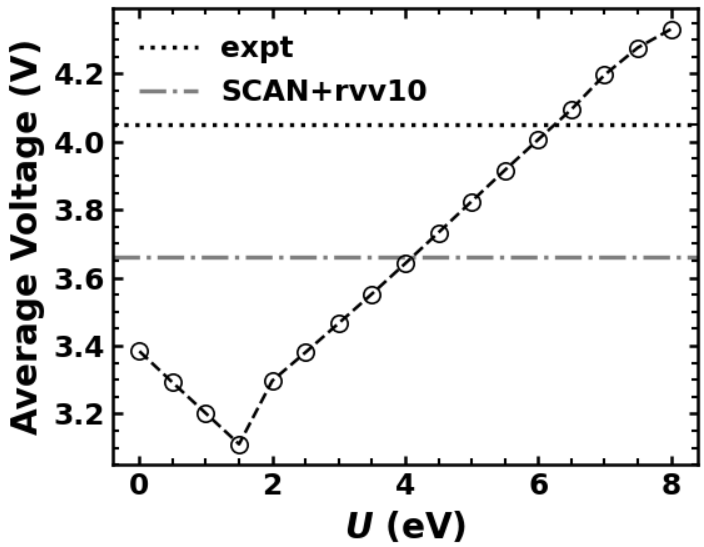

Figure 4.26: The average voltage for $LiMn_2O_4$ — Mn_2O_4 as a function of U. The black dotted line shows the experimental value and the grey dash-dotted line shows the computed value using SCAN+rVV10.

in response to U. The work of Dudarev [26] which presented the GGA+U formalism employed in this work, compared measured spectra only of the O_{2p} conduction band, in NiO to that of GGA+U. An interesting point is that if the electronic structure allows it, U has a strong tendency towards spin-polarization leading to ordering of band energies that may not be intuitive. For example, in $LiNiO_2$, the $t_{2g}^{\uparrow}$ band was shifted to energies lower than that of the a_{1g} and t_{1u} bonding bands. Obtaining an average voltage in agreement with experiment could in fact be a case of "getting it right for the wrong reasons". It would thus be of value to obtain high fidelity electronic structures and energies from beyond-GGA methods, such as the Random Phase Approximation (RPA) or hybrid functionals, to compare with GGA+U and experiment. Since average voltages computed with SCAN+rVV10 were also underestimated for Ni and Mn oxides, but gave very good agreement for the Co oxide, another good approach may be to add a small U value to SCAN+rVV10.

As a final point, it should be stressed that the intention of this work is not to claim that GGA+U should not be used for Li-containing TM oxides, but that care should be taken to understand how the particular choice of U may influence results.

Chapter 5

Is Co dispensable in Ni-rich positive electrode materials?

The current state-of-the-art positive electrode materials for Li-ion batteries are so-called NCA or NMC materials. Both of these materials are generally considered "Ni-rich", because Ni is the TM contained in the largest quantity and $LiNiO_2$ is the parent material. In the case of NCA, some Ni atoms are substituted for Co and Al, giving the chemical formula $LiNi_{1-x-y}Co_xAl_yO_2$, and in the case of NMC, some Ni atoms are substituted for Mn and Co, giving the chemical formula $LiNi_{1-x-y}Mn_xCo_yO_2$. Figure 5.1 shows how an example NMC crystal structure can be obtained from a $LiNiO_2$ unit cell. In this depiction, Ni, Mn, and Co are represented by grey, purple, and blue octahedra, respectively and O atoms are represented by red spheres. The layered structure is preserved through the Ni substitutions and the substitutive TMs (Co and Al, or Mn and Co) are randomly distributed in the TM layers.

Increasing the Ni content in both NCA and NMC materials is desirable because it leads to increased specific capacity; a larger fraction of Li atoms can be removed from the material at the designated upper cut-off voltage. This is generally paired with worse capacity retention, but optimization of electrolyte composition, particle morphology, surface coatings, and synthesis conditions has lead to commercial-quality materials with up to ∼80 % Ni.[89, 75] But the economy rules; if a material is too expensive, even if it is the best, it may not be widely adopted. In this regard, Co is much more expensive than Ni, Mn, and Al, and its cost is much more volatile (prone to sudden, unforseen changes). Additionally, there are ethical concerns surrounding Co mining [3] that, paired with high and volatile cost, generates a strong economic driving force to eliminate Co from Ni-rich materials. Naturally, one might ask "why is Co used at all?", and this would be a great question, the answer to which is not clear. Perhaps it is simply a relic of history; $LiCoO_2$ can be synthesized with no cation mixing (TMs in the Li layers)[71], whereas initial synthesis of $LiNiO_2$ contained substantial amounts of Ni atoms in the Li layers and cycled far worsely, [62, 49] leading

to a widespread adoption of $LiCoO_2$ over $LiNiO_2$. The prevailing methodology in the literature has been to incrementally increase the Ni content while decreasing the Co content in both NCA and NMC materials, converging towards $LiNiO_2$. In this section, the opposite approach is investigated; starting from $LiNiO_2$, how do small amounts of Ni substitutents influence electrochemical properties? This work was motivated by Figure 5.2 where the differential capacity of NCA with 5 % Al and 5 % Co (NCA900505) is compared to that of $LiNiO_2$ with 5 % Al or 5 % Mn ($LiNi_{0.95}M_{0.05}O_2$, M = Al, Mn).[47] There are certainly differences between these curves; the peak near 3.6 V during charge (positive dQ/dV) is much more pronounced in NCA900505 and is generally associated with kinetics — a supressed peak indicates kinetic hindrance (this point is discussed in section 5.2), the charge and discharge peaks just below 4.2 V are suppressed to a greater extent in NCA900505, but really not by much considering there is an additional 5 % Co in the material. Overall the similarities between these curves are striking and beg the question: what is the role of small amounts of Co in Ni-rich positive electrode materials? This Chapter aims to answer that question by going "back to basics" and isolating the effects of individual substituents on the electrochemical, thermal, and kinetic properties of Ni-rich positive electrode materials. Results presented in this Chapter have been published in references [47, 19, 69, 68].

5.1 Influence of dilute substitution on the electrochemical and thermal properties of $LiNiO_2$

5.1.1 Li site energy landscape

The Li site energy landscape is the fundamental property that determines the structure of the voltage-composition profile for Li intercalation reactions. In $LiNiO_2$, there are a number of phase transitions that have been characterized by *in situ* X-ray diffraction XRD.[48] Of particular interest is the so-called H2-H3 transition just below 4.2 V vs Li/Li^+, where the phase coexistence in this region corresponds to one phase with some remaining Li, denoted H2, and a second phase with no or very little remaining Li, denoted H3. The exact crystal structure of the H2 and H3 phases, which depends on the arrangement of Li atoms, is not known; neutron diffraction studies

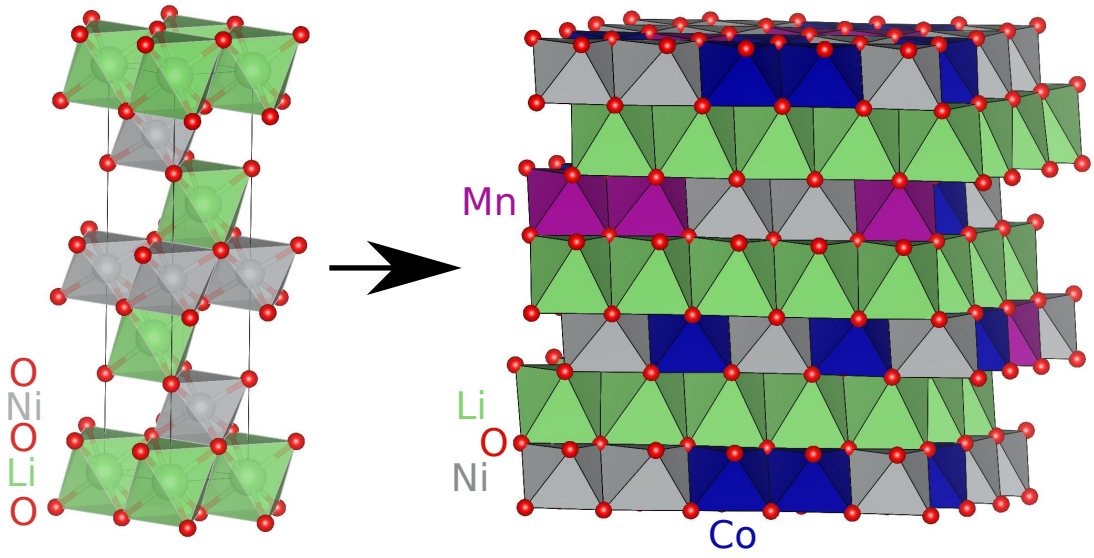

Figure 5.1: An example NMC material (right). The parent structure of $LiNiO_2$ (left) is preserved but has Ni atoms (grey spheres) partially substituted for Mn and Co. Li atoms are represented by green spheres, Li sites are encompassed by green octahedra, Ni, Mn, and Co sites are encompassed by grey, purple, and blue octahedra, respectively, and O atoms are represented by red spheres.

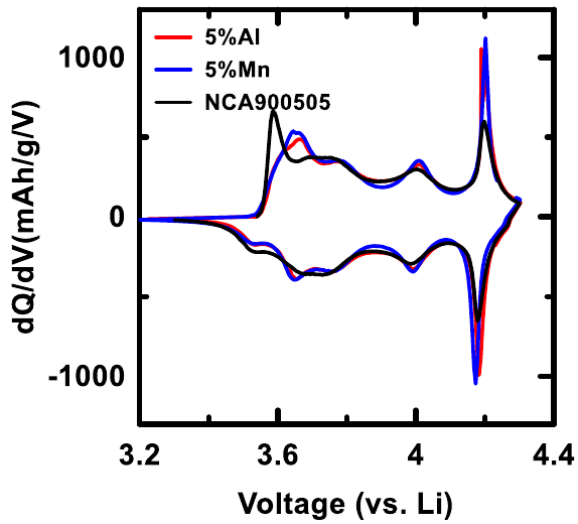

Figure 5.2: Differential capacity versus voltage for $LiNi_{0.9}Co_{0.05}Al_{0.05}O_2$ (NCA900505, black), $LiNi_{0.95}Al_{0.05}O_2$ (red), and $LiNi_{0.95}Mn_{0.05}O_2$ (blue).[47]

are required to resolve any superstructure arrangements. However, *in situ* XRD measurements revealed a large difference in volume between the H2 and H3 phases [48] due to a contraction of the layers in the out-of-plane direction, that is postulated

to cause particle fracture during charge-discharge cycling, leading to poor capacity retention and oxygen evolution. Figures 5.3a1-a5 show the voltage-composition profiles for $LiNiO_2$ and $LiNi_{0.95}M_{0.05}O_2$ (M = Al, Mn, Mg, or Co), and Figure 5.3b1-b5 shows the corresponding differential capacities, dQ/dV versus voltage from Ref. [47]. Note that by plotting dQ/dV vs. voltage, sharp peaks correspond to well-defined plateaus in the voltage-composition profiles and are an indication of a phase transition (*in situ* XRD is generally required to confirm two-phase coexistence). In Figure 5.3b1, the H2-H3 phase coexistence is clearly marked by sharp peaks during charge and discharge just below 4.2 V. Figures 5.3b2-b4 subsequently show a strong suppression of these peaks as 5 % Al, Mn, or Mg is substituted for Ni. In the case of 5 % Co however, the H2-H3 phase transition peaks are suppressed compared to $LiNiO_2$ but not nearly to the same extent as for 5% Al, Mn, or Mg. Considering the small amounts of substituents, the differences in voltage-composition profiles are striking and beg the question: how can only 5% substituents have such a significant impact on the electrochemical properties of LNO? This can be at least partly understood using atomistic computations. Results presented in this section have been published in [47].

Understanding how the energies of Li sites are influenced by substituents can help explain the suppression of phase transition peaks observed in Figure 5.3. Figure 5.4a shows the various Li configurations considered in the neighbourhood of substituent sites. A supercell consisting of $3 \times 3 \times 1$ repetitions of the hexagonal $LiNiO_2$ unit cell was used, substituting a single Ni atom for either Al, Mg, Mn, or Co and considering 5 different Li arrangements within the layers directly above and below the substituent-containing TM layer with a single Li atom in each layer (1/9 remaining Li). This amounts to supercells containing a total of 84 atoms.

Each configuration is denoted by two letters that describe the relationship between the Li and substituent sites: “E” (yellow) — the Li and substituent octahedra are edge-sharing, “V” (green) — the Li and substituent octahedra are vertex-sharing, and “F” (light blue) — Li occupies a site as far from the substituent as possible (for the size of the supercell). The dark blue octahedron in the bottom-most Li layer represents a Li site that was constantly occupied in all five configurations.

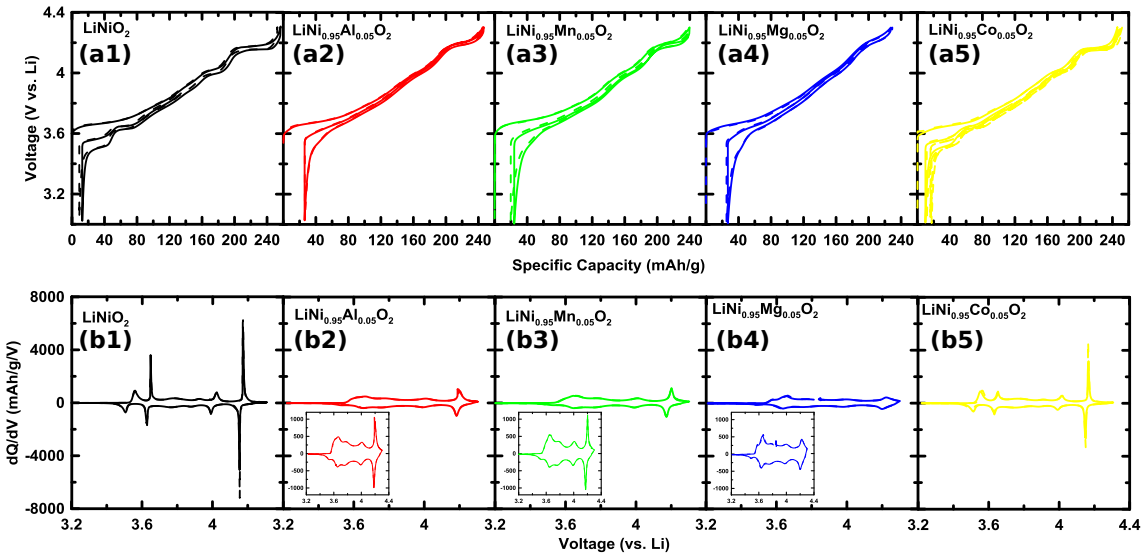

Figure 5.3: (a1-a5) Voltage versus specific capacity (composition) for $LiNiO_2$ (black) and $LiNi_{0.95}M_{0.05}O_2$ with M = Al (red), Mn (green), Mg (blue), Co (yellow). (b1-b5) Corresponding differential capacity versus voltage curves. The color correspondence is the same as a1-a5. The insets in panels b2, b3, and b4 have zoomed-in vertical axes to show more clearly the structure of the dQ/dV profiles.

Employing the SCAN+rvv10 functional to approximate the exchange and correlation energies, as implemented in VASP [45, 44, 46], the total ground state energies of each configuration were computed (25 in total - 5 substituents, 5 Li arrangements) by fully relaxing the atomic positions and lattice vectors with a plane-wave energy cut-off of 600 eV and a Γ-centered, $4 \times 4 \times 2$ **k**-point grid (20 irreducible **k**-points). PAW datasets [43] were used for Li, O, Ni, Mg, Al, Mn, Co with 3, 6, 18, 10, 15, 17 valence electrons, respectively. Total energy convergence to within 1 meV per supercell was achieved. Figure 5.4b shows the energies of each Li configuration relative to the (F,F) configuration for each substituent.

The black stars in Figure 5.4(b) show the Li site energy landscape when there are no substituents. The (F,F) configuration is preferred by ~ 250 meV. This configuration corresponds to occupied Li sites with maximal interlayer separation (i.e., projecting all three occupied Li sites into a single triangular lattice plane would result in maximal Li-Li distances) indicating a strong interlayer repulsion. This leads to full and empty layers which drive the H2-H3 phase separation. Similarly, the green

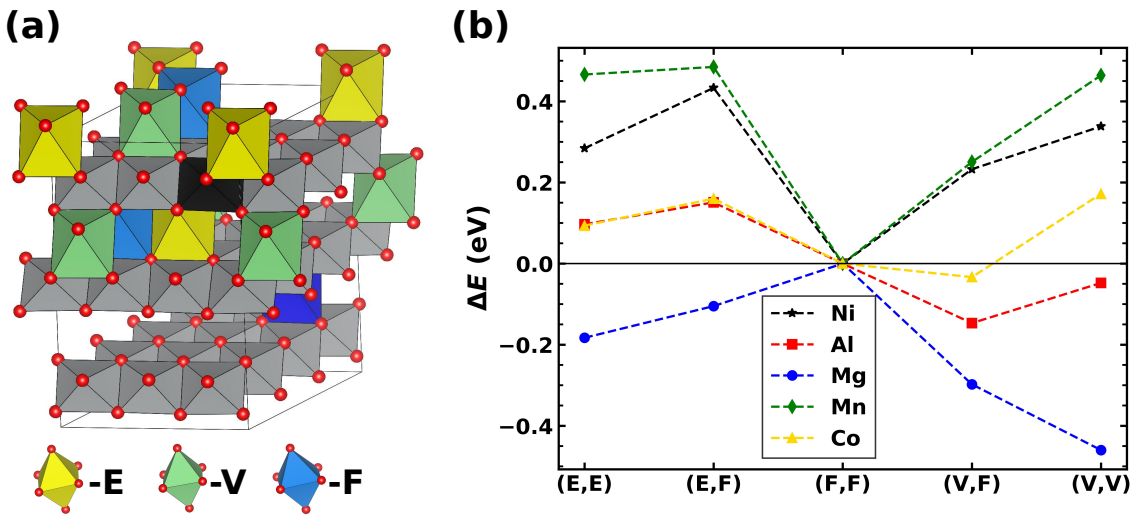

Figure 5.4: Li site energy landscape with TM substitution. (a) The various Li configurations are shown. The red spheres represent O atoms, the grey octahedra represent Ni atoms, the black octahedron represents the substitutive site to be occupied by either Ni (no substitution), Al, Mg, Mn, or Co. The colored octahedra represent Li atoms. $3 \times 3 \times 1$ repetitions of the hexagonal $LiNiO_2$ unit cell is shown. For each configuration, a single Li site is occupied in each layer and the colors denote the spatial relationship to the substitutive site; edge-sharing octahedron (yellow), vertex-sharing octahedron (green) and spatially separated (light blue). A Li configuration is composed of two sites, one in the layer above and one in the layer below the substitutive site. The Li site in the bottom-most layer (dark blue) is unchanged in all configurations. (b) Site energies relative to the (F,F) configuration for Ni (black stars), Al (red squares), Mg (blue circles), Mn (green diamonds), and Co (yellow triangles) occupying the substitutive site.

diamonds show that the (F,F) configuration is also preferred when Mn is substituted in a Ni site. However there is a caveat; Mn substitution leads to cation mixing where some Ni and Li atoms are exchanged (this can be explained simply with charge balance), so the fact that Mn substitution in these computations gives the same energy landscape as Ni suggests that the suppression of phase transition peaks seen in Figure 5.3(b3) can be attributed to cation mixing. Indeed, the following interpretations of the Li site energy landscape for the other substituents reveal that charge balance is enforced locally, and as a consequence the Ni atoms occupying Li sites would be spatially coordinated with Mn in randomly distributed sites, hindering Li ordering and the formation of the H3 phase.

The red squares show that in the case of Al substitution, the (V,F) configuration is

preferred corresponding to Li occupying one vertex-sharing site and another spatially separated site. Comparatively, the blue circles show that for Mg substitution, the energetically preferred Li configuration has both Li sites vertex-sharing with the Mg site. The phase transition suppression argument for Al and Mg substitution is the same; the substituents are randomly distributed in the TM layers and because they attract Li in preferential sites, long-range Li ordering is hindered. The H2-H3 phase transition is also suppressed because the Li energy well owed to the presence of Al and Mg prevents layers from being fully emptied below 4.3 V. To this end, it would be expected that Mg substitution would have a greater effect due to the deeper energy well created for two Li sites. Indeed, Figure 5.3(b4) shows the greatest degree of H2-H3 peak suppression.

The yellow triangles in Figure 5.4(b) show the Li site energies for Co substitution. The (F,F) and (V,F) configurations are energetically competitive, meaning that for a small energy cost, Li atoms could occupy the (F,F) configuration, which is energetically preferred when there are no substituents. A small disturbance to Li ordering would be expected from this site energy landscape and it should be slightly more difficult to fully empty Li layers, leading to a moderate suppression of phase transition peaks. Figure 5.3b5 reflects this analysis; the overall structure of the dQ/dV curves are retained, but the peaks are slightly less pronounced compared to $LiNiO_2$ in Figure 5.3b1.

The overall analysis of the changes to Li sites energies due to TM substitution explains well the experimental observations. However, an argument based on charge balance alone can get to nearly the same conclusion. In $LiNiO_2$, Ni must occupy a 3+ oxidation state to maintain electro-neutrality. Al has one $3p$ electron and two $3s$ electrons, preferentially being oxidized to 3+. The Al oxidation potential from 3+ to 4+ is very large, so for each Al atom in the material, one Li atom would be rendered "inactive". Similarly, Mg has two $3s$ electrons and cannot be oxidized to 3+, hence for each Mg atom in the material, two Li atoms would be rendered "inactive". Indeed, the 1:1 and 1:2 "inactive" Li trend is observed for dilute concentrations of Al and Mg, respectively.[47] However, this simple argument on its own does not explain the suppression of the H2-H3 peak because the extent to which charge balance is enforced locally is not captured; the Li site energy landscape demonstrates how charge balance

must be satisfied locally and Li sites with a specific spatial relation to the substitutive site become energetically favoured. This last part is required to demonstrate how the H3 phase is prevented from forming by binding Li atoms in randomly dispersed sites.

5.1.2 Propensity for O evolution

An important limitation of Ni-rich positive electrode materials is the greater propensity for O evolution as the Ni content is increased. This means that the more Ni is in the material, the less safe it becomes when charged, leading to higher risk of thermal runaway. An example reaction where O is evolved is $NiO_2 \rightarrow NiO + \frac{1}{2}O_2$. This represents a reaction without any Li, when some parts of charged $LiNiO_2$ are empty of Li, such as in the H2-H3 phase transition region near 4.2 V. The difference in free energy between the reactants and products determines the thermodynamic force that drives this reaction, but there is also a kinetic barrier that must be overcome. Thermal runaway occurs when the heat released from the O evolution reaction is sufficient to combust the oxygen gas and electrolyte mixture, initializing further reaction. The risk of thermal runaway is greater when the thermodynamic driving force is large (a lot of heat released per reaction unit) and the kinetic barrier is small (larger reaction rate). The first thing that must occur for O to be released from the material is the creation of an O vacancy. This section investigates the role of substituents (Al, Mg, Mn, Co), and of Li content, on the O binding energy (the energy required to create an O vacancy) — a factor that contributes to the reaction barrier. A larger binding energy would correspond to a larger reaction barrier, leading to a smaller reaction rate and a material less prone to thermal runaway. Binding energy computations were performed using the same computational parameters as in the previous section. Results presented in this section have been published in [19]

Figure 5.5 shows the O binding energies for various local O environments, depicted in Figure 5.5(a), where O vacancies are formed within different surroundings. In these depictions, O vacancies are represented with black spheres and O atoms by red spheres. Li atoms occupy the center of the green octahedra, Ni atoms the center of the light grey octahedra, and substituent sites are encompassed by dark grey octahedra and are occupied by either Ni (no substituent), Al, Mg, Mn, or Co. The O environments depicted in Figure 5.5(a) only show the local environment but are part

of $3 \times 3 \times 1$ supercells made from the hexagonal $LiNiO_2$ unit cell. In this case, the local environment is the only important factor because the O binding energies are compared to the O binding energy from a reference environment. The O vacancy environments are described as follows, where in all cases the O vacancy is formed with 3 TM nearest neighbours and the substituent site can be occupied by either Ni, Al, Mg, Mn, or Co: I — O vacancy formed in a fully lithiated environment, corresponding to 3 Li nearest neighbours, and nearest neighbour to the substituent site; II — O vacancy formed in a partially de-lithiated material with 1 Li nearest neighbour and is nearest neighbour to the substituent site; III — O vacancy formed nearest the substituent site but second-nearest neighbour to a Li site; IV — O vacancy formed two O layers away from the substituent site and second-nearest neighbour to a Li site.

Figure 5.5(b) shows the O binding energy relative to that of environment IV with Ni occupying the substituent site (no substituent). All of the points for environment IV lie nearly on top of each other, irrespective of the substituent, suggesting that dilute substituent concentrations only influence the local O environment. The relative binding energies are plotted against a dimensionless proximity metric defined as: $\alpha = d^{M-V_0}/d_0^{M-O} + (1/n)d_{avg}^{Li-V_0}/d_0^{Li-O}$. Here, d^{M-V_0} is the distance between the substitutive site and the O vacancy, d_0^{M-O} is the equilibrium substituent-O distance in the fully lithiated material, n is the number of vacancy-coordinated Li atoms, $d_{avg}^{Li-V_0}$ is the average Li-O distance of vacancy-coordinated Li atoms or of the nearest Li atom if there are no vacancy-coordinated Li atoms, and d_0^{Li-O} is the equilibrium Li-O distance in fully-lithiated $LiNiO_2$. α is then a dimensionless metric that gives the proximity between an O vacancy and both a substitutive site and occupied Li sites. Smaller values of α correspond to O vacancies near a substitutive site and coordinated by Li atoms (α is smaller if there are more vacancy-coordinated Li atoms), while larger values of α correspond to O vacancies coordinated by only Ni, away from a substitutive site and Li atoms.

The black stars show the O binding energy without the presence of substituents, which indicates how local Li arrangements influence the formation of O vacancies. In this case, environments III and IV are within ~ 0.03 eV of each other because in both cases the O vacancy is formed without any Li nearest neighbours. Environment II and environment I, on the other hand, penalize the formation of an O vacancy

by ~ 0.5 and ~ 1.0 eV due to the presence of one and three Li nearest neighbours, respectively. The black stars in Figure 5.5(b) can then be interpreted as showing the extent to which Li penalizes the formation of O vacancies in Li_xNiO_2 ($0 < x < 1$). With this in mind, the difference between the black stars and each set of points that correspond to different subsituents can be understood to represent how the substituent itself influences the O binding energy for each environment.

The relative binding energies of environment I and II represented by the black stars are 1.0 and 0.5 eV lower compared to environments III and IV, indicating that Li alone binds O strongly. The substituents also penalize the formation of O vacancies more severely than Ni, where the largest difference is seen in environments I and III. Environment I corresponds to a fully lithiated material, which is synthesized at high temperature so is thermally stable; any benefit to the O binding energy in this environment would not directly benefit material stability since O evolution reactions in the fully lithiated state must occur at temperatures far greater than typical cycling conditions. The benefit to the O binding energy observed for environment III from Al, Mn, and Co suggest that with sufficiently large substituent percentage, material stability should be improved even in highly delithiated states.

Figure 5.6 shows Accelerating Rate Calorimetry (ARC) measurements from Ref. [19] for $LiNiO_2$ (LNO) and $LiNi_{0.95}M_{0.05}O_2$ (M = Al, Mg, Mn, Co) at two different states of charge. ARC measurements are done by placing electrode powder with electrolyte in a stainless steel tube that is sealed.[54, 55] A thermocouple measures the temperature of the tube over time. The purpose of ARC measurements is to detect exothermic reactions, so the sample is incrementally heated until self-heating is detected. Plotting the self-heating rate, dT/dt versus the temperature shows how the exothermic reaction proceeds. For example, a curve that becomes steeper as the temperature increases indicates thermal runaway; the heat generated by the reaction accelerates the reaction further. On the other hand, a curve that dips downward indicates a reaction that proceeds in a much more controlled manner, reacting all available reactants without a significant change to the reaction rate despite an increase in temperature. A thermal runaway reaction must have a comparatively smaller activation barrier.

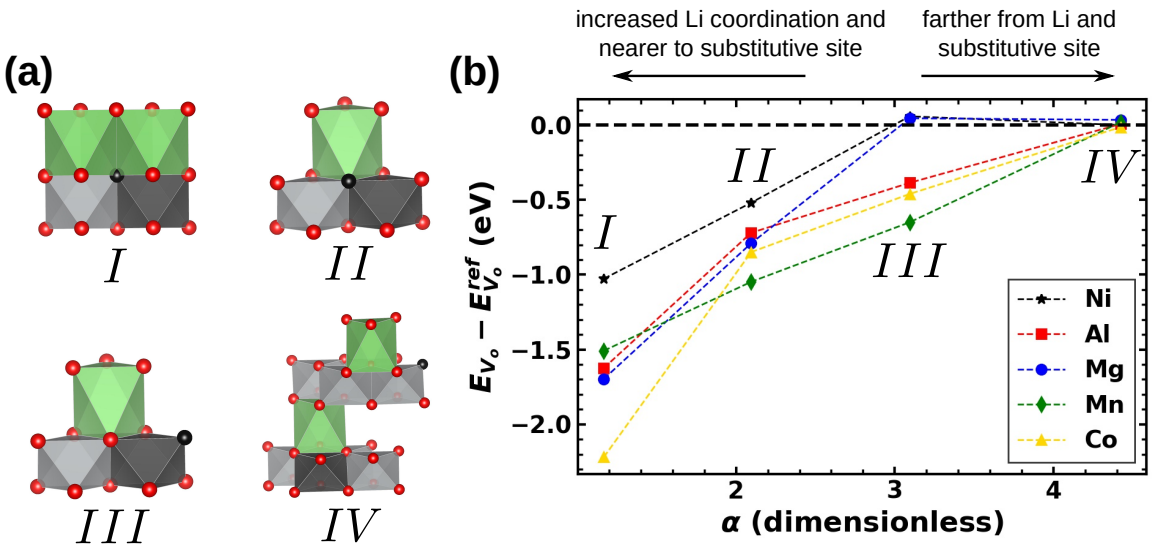

Figure 5.5: Relative O binding energy as a function of distance from Li atoms and substituent site. (a) Four different O sites are depicted, where the green and light grey octahedra encompass Li and Ni sites; the dark grey octahedra encompasses the substituent sites and can be occupied by either Ni, Al, Mg, Mn, or Co; and the red spheres represent O atoms. (b) The O binding energy is shown relative to the binding energy of environment *IV* without substituent (Ni in the substituent site). The relative O binding energy is plotted against a dimensionless proximity metric, α, that reflects the distance of the O vacancy to both its nearest Li atoms and the substituent sites (see text for details).

Figure 5.6(a) shows ARC measurement for materials charged to 230 mAh/g, corresponding to approximately 16 % remaining Li. The LNO (black) and Co-substituted (gold) materials show clear signs of thermal runaway while the Al, Mg, and Mn substituted materials show controlled exothermic reactions. Clearly, only 5% Al, Mg, or Mn significantly improves material reactivity. However, Figure 5.6(b) shows ARC measurements for the same materials (excluding Mn and Co) but charged to 190 mAh/g, corresponding to approximately 30% remaining Li. In this case, even the LNO (black) material, where there are no substituents, does not experience thermal runaway. The difference between the LNO reactivity observed in panel (a) compared with panel (b) can be attributed to the presence of the H3 phase, which does not contain any Li. At 16% remaining Li, the H2 and H3 phase coexist and thermal runaway is caused by reaction of the H3 phase. Conversely, at 30% remaining Li, the H3 phase does not exist and the material does not go into thermal runaway. With this in

mind, recall from the previous section that 5% Al, Mg, and Mn suppressed the H2-H3 almost completely by hindering the complete removal of Li. It is thus the suppression of the H3 phase from substitution that improves material reactivity. This explains why the Co substituted material also undergoes thermal runaway when charged to 230 mAh/g; 5% Co is not sufficient to suppress the H2-H3 phase transition.

In summary, 5% Al, Mg, Mn substituted into LNO suppress the H3 phase transition by changing the Li site energy landscape. The H3 phase is the bad actor, leading to poor capacity retention due to a large difference in unit cell volume and increased material reactivity. Even such a small percentage of substituent greatly improves electrochemical and thermal material properties by locally altering the Li site energy landscape, inhibiting the formation of the H3 phase.

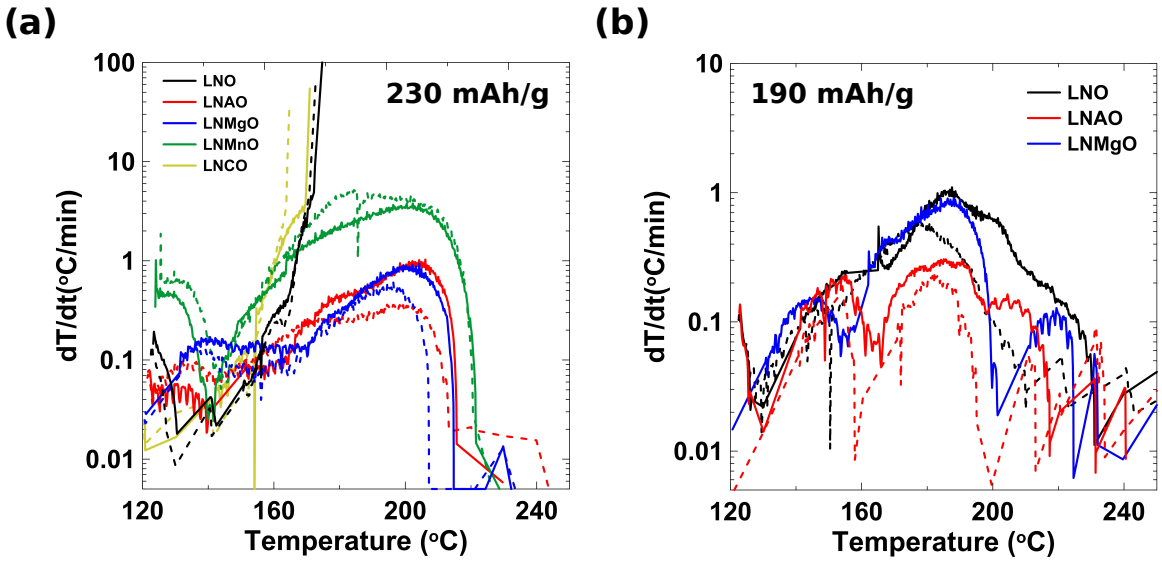

Figure 5.6: Accelerating rate calorimetry (ARC) for $LiNiO_2$ (LNO, black), $LiNi_{0.95}M_{0.05}O_2$, M = Al (LNAO, red), Mg (LNMgO, blue), Mn (LNMnO, green), Co (LNCO, yellow) charged to (a) 230 mAh/g ($\sim$ 16% remaining Li) or (b) 190 mAh/g ($\sim$ 30 remaining Li).

5.2 Li kinetics and Cobalt

Thermodynamics is not the only important factor to consider for electrode materials used in Li-ion batteries; cycling is inherently an out-of-equilibrium process, thus dynamics can play an important role. The load on a Li-ion cell together with Li

kinetics determine how far from equilibrium a material is operating. In laboratory environments, cells are typically cycled at constant current within a specified voltage interval; for example, from 3.0 to 4.3 V at a "C-rate" of C/2. In this case, the current is chosen so that the cell is charged in 2 hours and discharged in 2 hours. Expressing the load on a cell in terms of "C-rates" normalizes for the total capacity of the cell because the specific current needs to be the same for a given material in order to charge it in a given amount of time, no matter how much material there is. The motion of Li ions within the electrode particles and through the electrolyte as a cell is charged and discharged is driven by the current. However, Li ion mobility is always limited, leading to concentration gradients in both the electrodes and the electrolyte. Larger currents, or higher C-rates, lead to more substantial concentration gradients that can lead to failure mechanisms on the material level; for example large stresses can develop between regions with different Li concentrations, causing intra-particle fracture, leading to capacity loss over time. On the other hand, single cycles are also affected by substantial Li concentration gradients within electrode particles; the total amount of Li inserted into the positive electrode up to a fixed voltage decreases as the rate increases (the capacity decreases with increasing rate). This occurs because the voltage of a cell is determined by the Li concentration at the surface of electrode particles. If there is a substantial Li concentration gradient within positive electrode particles during discharge (as Li atoms are inserted into the material), for example, the surface concentration will be greater than the average bulk concentration, leading to a voltage that is lower than the one corresponding to the average Li concentration. The result is that more severe Li concentration gradients within electrode particles lead to smaller achieved capacities.

Figure 5.7 shows an example voltage versus specific capacity curve for various C-rates during discharge of a real Li-ion cell. As the C-rate increases from C/20 to 3C, the achieved specific capacity decreases by about 55 mAh/g; more than a 25 % decrease from the C/20 capacity. Even the capacity at the nominal 1C rate is appreciably reduced, which highlights practical considerations for both power delivery and charge times. There are two fundamental ways to improve Li kinetics in positive electrode materials; improve the lattice diffusivity of Li in the host material, or reduce the size of particles. Lattice diffusivity is a material property that depends on

structure and composition while particle size is a morphological property that can be controlled, at least to a certain extent, with synthesis conditions. Smaller particles are typically less desirable because of greater total surface area for the same amount of material, leading to increased reactivity with electrolyte components and decreased thermal stability. The ability to maximize particle size for a particular material in a particular use-case can be beneficial to cell manufacturers. Li kinetics presents yet another cell design property to optimize. It is then important to characterize Li diffusivity in positive electrode materials so that particle sizes can be carefully tuned for various cell use conditions and cells can adequately meet their performance needs.

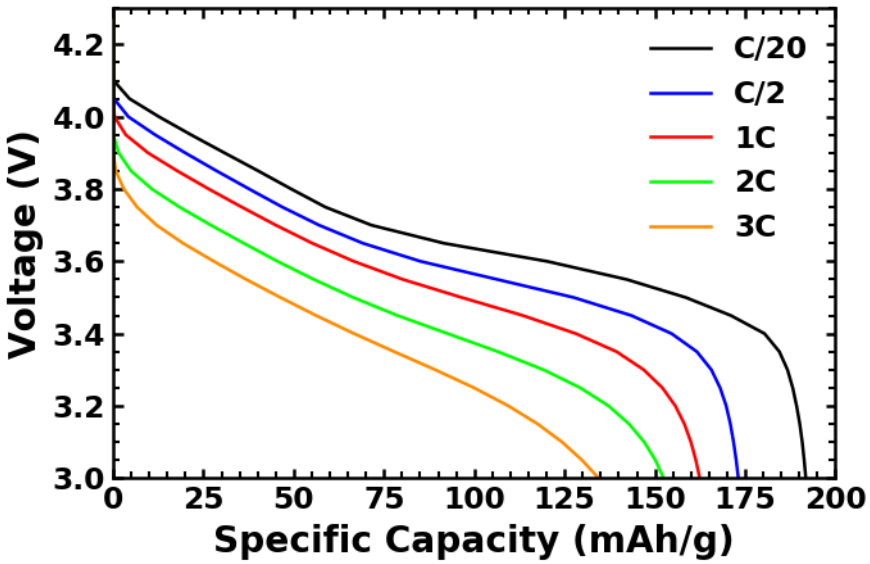

Figure 5.7: Specific capacity achieved during discharge at C/20 (black), C/2 (blue), 1C (red), 2C (green), 3C (orange). These data are unpublished but were measured by members of our lab and correspond to a real Li-ion cell.

This section presents the development of a reinvented approach for measuring Li diffusivity (Li chemical diffusion coefficient, D_c) and discusses consequences of increasing the Ni content, while reducing the Co content, in Ni-rich positive electrode materials. Prevailing methods to quantify Li kinetics include extracting Li chemical diffusion coefficients, D_c, from galvanostatic intermittent titration technique (GITT) or electrochemical impedance spectroscopy (EIS) measurements. Ref. [61] compared various models that are used in the literature to fit to GITT data and found that values of D_c can differ by several orders of magnitude. Additionally, GITT and EIS

measurements from different groups have reported D_c values differing by several orders of magnitude for the same material.[2, 16, 18, 61] It is then of great importance to develop a reliable method to measure D_c in order undertake systematic comparisons of Li diffusivity across a broad range of materials. This section describes a new method for extracting D_c from measured data — the Atlung method for intercalant diffusion (AMID), and covers an example application of the method. In fact, D_c measurements on Li_xNiO_2 show a maximum value on the order of 10^{-13} cm^2s^{-1}, while reference [16] measured a maximum D_c on the order of 10^{-7} cm^2s^{-1} using EIS. Additionally, relevant atomistic computations to inform studies of Li kinetics are also discussed. Results presented in this section have been published in [69].

5.2.1 Li migration pathway

In layered TM oxides, the dominant Li diffusion pathway between octahedral sites has been shown to take place via an intermediate tetrahedral site, and coined the "tetrahedral site hop" (TSH) by Van der Ven and Ceder. [81, 80] Figure 5.8 has been adapted from [82] and shows the Li migration pathway. Figure 5.8 (a) shows TM layers above and below a Li layer. The brown octahedron encompass TM sites and could be any TM that substitutes into the layered structure (Ni, Co, Mn, etc). The yellow circles represent O atoms while the red circle represents the migrating Li atom. Li octahedra are shaded in green and the intermediate tetrahedral site is bounded with red lines. The black arrow depicts the migration path from an initial octahedral site, into the intermediate tetrahedral site, through to the final octahedral site. This pathway is shown in Figure 5.8 (b) for two different local Li environments; one where there is only one available octahedral site (single-vacancy), the other where two adjacent octahedral site are vacant (di-vacancy). In this case, the Li plane is projected in two dimensions so that the octahedral sites are at the vertices of the triangular lattice, and the tetrahedral sites are indicated with small green triangles. The red arrow shows the path taken by a migrating Li atom. Figure 5.8 (c) shows the computed energies along each of the two migration pathways. The green circles show pathway energies for the single-vacancy migration while the red circles show the energies along the di-vacancy pathway. The energy of the tetrahedral site is strongly influenced by the local Li environment; if the intermediate tetrahedron shares

a face with an occupied Li octahedron, as is the case for the single-vacancy pathway, there is a strong electrostatic repulsion that raises the tetrahedral site energy. On the other hand, the intermediate tetrahedron in the di-vacancy pathway shares all three faces with empty octahedra, giving a tetrahedral site energy nearly 400 meV lower in comparison to the single-vacancy. There exist another possible pathway for Li migration that is not shown here; the so-called "oxygen dumbbell hop" (ODH), where a Li atom occupying an octahedral site follows the shortest distance path to a neighbouring octahedral site. However, the energy barrier associated with ODH is generally at least at large as the single-vacancy TSH. [81]

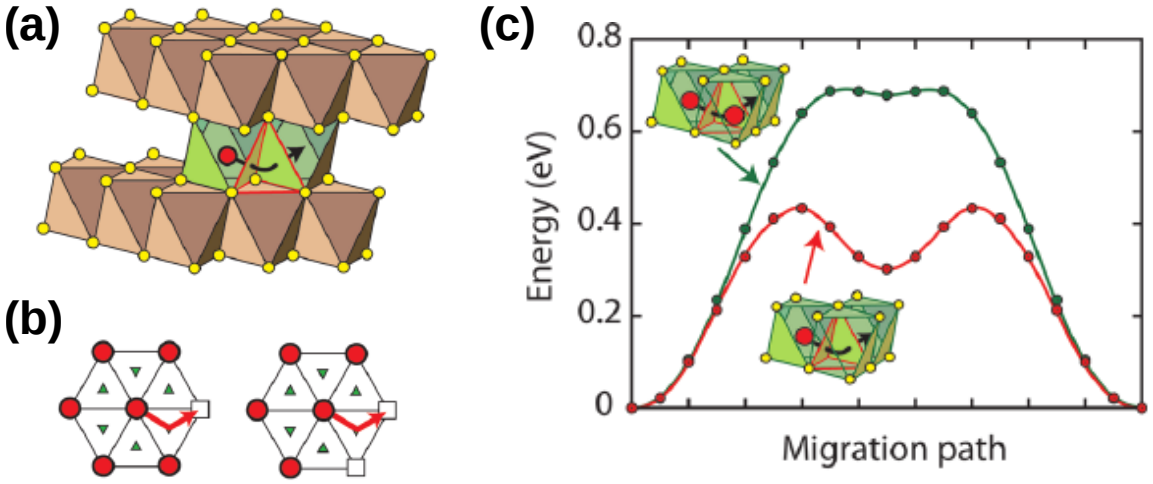

Figure 5.8: Reproduced from Van der Ven *et* al. [82]. Showing the pathway taken by a migrating Li atom. (a) Two transition metal (TM) oxide slabs, with TM site encompassed by brown octahedra and O atoms represented by yellow circles, with a Li atom (red circle) migrating from one octahedral site (green octahedra) to another through an intermediate tetrahedral site (red lines). The black arrow shows the path taken by the Li atom. (b) A two dimensional projection of the Li plane, showing the octahedral Li sites with red circles, Li vacancies with hollow squares, and tetrahedral sites with green triangles. The red arrows show the path taken by the migrating Li atom. The diagram on the left corresponds to a single vacancy path while the diagram on the right to a di-vacancy path. (c) Showing the energy along the migration path for a single vacancy path (green circles) and a di-vacancy path (red circles).

5.2.2 Diffusion measurements from a reinvented approach

Problems of diffusion become equivalent to Fourier's heat conduction law if the diffusion coefficient is assumed to be constant (i.e., independent of concentration). Diffusion is then described by Fick's laws. In this case, the concentration of diffusing species in a solid as a function of time and position is governed by two coupled partial differential equations:

$$\mathbf{j} = -D_c \nabla c \tag{5.1}$$

$$\frac{\partial c}{\partial t} = D_c \nabla^2 c \tag{5.2}$$

where, c is the concentration of the diffusing species and is a function of position and time, $\mathbf{j}$ is the flux arising from spatially dependent concentration changing in time, and D_c is the chemical diffusion coefficient.

General solutions to equations 5.1 and 5.2 can be obtained for various classes of boundary and initial conditions. In the case of constant current charge or discharge of an intercalation material, the electrochemically active species flux (e.g., Li ions) at the surface of electrode particles is assumed to be constant (of course there may be small fluctuations on the atomic scale, but these are averaged out over the surface of each particle). In 1979, Atlung *et* al. [5] presented the diffusion equivalent of Carslaw and Jaeger's solution to the conduction of heat [17] for spherical, cylindrical and planar particle geometries with a constant prescribed flux at their surfaces. In all three cases, diffusion is reduced to a one-dimensional problem.

With a constant intercalant flux at the particle surfaces (constant current discharge), the general expression for the intercalant concentration, c, with diffusion coefficient D_c, as a function of position and time is:

$$c(z,t) = \frac{j_0 r}{D_c}\left[a\frac{D_c t}{r^2} + \frac{z^2}{2} - b - \frac{2}{z}\sum_i \frac{\exp(-\alpha_i^2 D_c t/r^2)}{\alpha_i^2} C(\alpha_i z)\right] \tag{5.3}$$

here r is the bounding spatial extent of the geometry (e.g., the radius of a spherical particle, or 1/2 the thickness of a slab, etc ...), $z = x/r$ is the normalized diffusion coordinate, and all other quantities are geometry dependent. For spherical electrode

particles, the constants a and b equal 3 and 3/10, respectively; the expansion coefficients are given by the roots of the generating equation $\alpha_i \cot(\alpha_i) - 1 = 0$; and the functions $C(\alpha_i z) = \sin(\alpha_i z)/\sin(\alpha_i)$. The exact solution requires infinitely many α_i's, but in practice the summation must be truncated, thus the summation index, i, labels the unique α_i's that satisfy the generating equation. j_0 is the flux density and hence depends on the surface area of the electrode particles. Spherical particles with average volume, V, have average surface area $S = 3V/r$. If T is the expected discharge time at constant current demanded by the load on the cell, and n is the average number of intercalant atoms inserted into each particle over the course of the discharge process, then the flux density for spherical particles is $j_0 = (n/T)(1/S) = nr/(3TV)$. Defining $X = cV/n$ as the average fractional intercalant content, $\tau = t/T$ as the average fractional capacity (the ratio of time elapsed to the expected discharge time at constant current), and $Q = T/(r^2/D_c)$ (the ratio of the expected discharge time to the characteristic diffusion time, i.e., fractional time) leads to a dimensionless expression relating fractional capacity to fractional time:

$$X = \tau + \frac{1}{3Q}\left[\frac{z^2}{2} - \frac{3}{10} - \frac{2}{z}\sum_i \frac{\exp(-\alpha_i^2 Q\tau)}{\alpha_i^2}\frac{\sin(\alpha_i z)}{\sin(\alpha_i)}\right] \tag{5.4}$$

The quantity of particular interest is τ^*, the average fractional capacity when the particle surfaces reach their saturation value corresponding to a particular target potential, $X(z = 1) = X^* = 1$. This yields an implicit equation relating the average fractional capacity, τ^*, to the discharge time (embedded in Q):

$$X^* = 1 = \tau^* + \frac{1}{3Q}\left[\frac{1}{5} - 2\sum_i \frac{\exp(-\alpha_i^2 Q\tau^*)}{\alpha_i^2}\right] \tag{5.5}$$

The expected discharge time, T, can be expressed, in seconds, as $T = 3600n$, where n is the discharge time in hours (as in the so-called "C-rate", C/n, that indicates the charge or discharge time in hours), thus $Q = 3600nD_c/r^2$. The fractional capacity can be written as $\tau^* = q/q_{max}$, where q is the average capacity achieved at a particular expected discharge time, n, in hours, and q_{max} is the capacity that would be achieved in the limit of infinitely slow rate (i.e, if discharge were to occur in equilibrium, without concentration gradients). This finally yields an expression that relates capacity to

discharge time, given the average spherical particle radius and the intercalant chemical diffusion coefficient, D_c:

$$\frac{q}{q_{max}} + \frac{r^2}{3 \cdot 3600 n D_c} \left(\frac{1}{5} - 2 \sum_i \frac{\exp(-(q/q_{max}) 3600 n D_c \alpha_i^2 / r^2}{\alpha_i^2} \right) = 1 \qquad (5.6)$$

Measured data can be fit directly to Equation 5.6; providing the means to extract D_c from experimental measurements. The average particle radius, r, can be obtained from Scanning Electron Microscope (SEM) images, and capacities can be measured as a function of rates (currents). With these data, D_c and q_{max} can be treated as fitting parameters in a least squares regression fit. This approach to extract D_c maps experimental data onto phenomenological solid-state diffusion.

It is important to realize that other than particle geometry, equations 5.4 and 5.5 are universal expressions; within the dimensionless variables X, τ, and Q, the particular properties of the electrode are divided out. These equations hold true for *any* intercalation electrode with spherical particles within which diffusion can be appropriately described by equations 5.1 and 5.2. Equation 5.5 can be numerically solved for a finite number of expansion coefficients, α_i, to obtain universal curves relating τ^* and Q that depend only on the particle geometry. Figure 5.9 shows this curve for $\alpha_i,\ i = 1, ..., 150$. Once a value for D_c is obtained for a particular material, measured data can overlay onto this universal curve to visually assess how well diffusion may be described by equations 5.1 and 5.2. The striking aspect of this procedure is that measured capacity-rate data from any electrode chemistry, provided particles are spherical, that obey 5.1 and 5.2 will overlay well on this curve. This fact will be used later to quantify fit quality.

It is important to recall that equations 5.1 and 5.2 assume D_c to be constant. In the case of Li intercalation materials, such as $LiNiO_2$, kinetic issues typically arise at low voltage (fractional Li content close to 1), and at high voltage (fractional Li content close to 0) [51] which suggests a concentration dependent D_c. In order for the procedure outlined thus far to be applicable, capacity versus rate data must be obtained within sufficiently small voltage (or state of charge) intervals so that D_c is nearly constant.

Reference [24] describes an efficient method for obtaining capacity versus rate

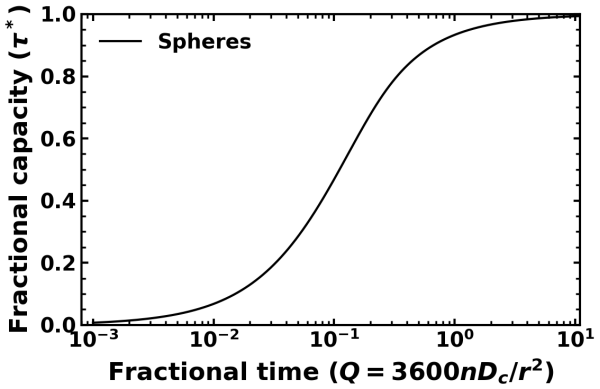

Figure 5.9: Universal capacity versus rate curve for spherical electrode particles assuming classical diffusion. The fractional capacity is the capacity reached at the specified cut-off voltage divided by the corresponding total available capacity, and the fractional time is the discharge time divided by the characteristic diffusion time. Both of these quantities are dimensionless.

data within specified voltage intervals; so-called "signature curves". The general procedure involves sequentially slower discharges (can also be done with charge) each separated by an open-circuit voltage (OCV) relaxation period. The assumption is that the cumulative capacity achieved at a particular rate following faster discharges is identical to the capacity that would have been achieved with a single discharge at the corresponding lower rate.

Figure 5.10 has been adapted from [69] and demonstrates the procedure of extracting capacity versus rate data from a "signature curve" within a specified voltage interval. Figure 5.10 (a) shows an example "signature curve" between 3.6 - 3.0 V where the red and black colors show data from pair cells. The sequential discharges employed C-rates from 1C to C/160 as calculated using the full theoretical capacity of the electrode. Separating each discharge step is an OCV period where the voltage rises as the Li concentration gradient within each electrode particle relaxes, lowering the Li concentration at the particle surfaces.

An important caveat of the "signature curve" method performed within small voltage intervals is the influence of IR contributions to the voltage, particularly at high rates. Consider the highest rate discharge in Figure 5.10 (a) (1C protocol rate on the far left); the voltage begins at 3.6 V but the capacity is only apparently increasing below 3.4 V. This voltage drop is due to a combination of internal cell

resistance (Ohmic resistance, IR) and diffusion related resistance. The problem is that at present the contribution from each cannot be quantitatively differentiated, and the measured capacities at high rate could be significantly influenced. For this reason, the data are weighted according to the magnitude of their voltage drops in the first step of each discharge within a particular "signature curve". This will be elaborated in the discussion relating to Figure 5.14.

Figure 5.10 (b) shows the cumulative capacity versus rate extracted from the "signature curve". At the fastest rate, on the far left, the capacity is simply the same as the measured capacity. For each successive rate, the corresponding capacity is the sum of the capacities of each preceding rate. Notice that Figure 5.10 (b) plots cumulative capacity versus effective rates, not versus protocol rates; the load on the cell when discharging within the 3.6-3.0 V interval is not represented by rates calculated using the full theoretical capacity. The actual load is determined from the discharge current and the total available capacity within the voltage interval, which together yield an effective rate. The total available capacity within a voltage interval is approximated using the total capacity from the "signature curve" (i.e., the cumulative capacity corresponding to the slowest rate).

Figure 5.10 (c) shows the measured capacity versus rate data (red and black circles) after extracting D_c overlaid on the universal curve (dashed) corresponding to equation 5.4. The agreement between the fitted experimental data and the theoretical curve is excellent! In this regard, it is imperative that readers recognize that D_c is the only fitted material property in this case; it seems somewhat astonishing that with a single parameter, agreement between phenomenology and measurement can be this good. It should of course be noted that not all fits show such good agreement; quality of fit metrics will be discussed after presenting the advanced signature curve protocol. The general procedure of fitting capacity versus rate data to the diffusion equation solutions presented by Atlung *et* al. [5] has been aptly coined the "Atlung Method for Intercalant Diffusion" (AMID).

In order to obtain state-of-charge dependent diffusion coefficients, "signature curves" within successive voltage intervals can be performed. Figure 5.11 shows the cycler protocol from which extracted data can be fit, showing both voltage versus time (left panel) and voltage versus specific capacity (right panel). In this graph, a fresh cell

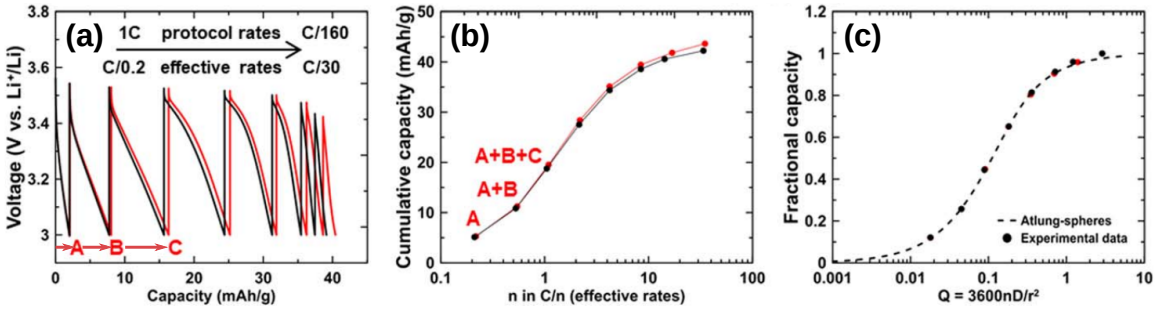

Figure 5.10: Taken from Ref. [69]. (a) A "signature curve" within the 3.6-3.0 V interval. Progressively higher rates are separated by an OCV period. The protocol rates are computed before the measurement using the theoretical capacity of the electrode while the effective rates are computed after the measurement using the total capacity achieved during the "signature curve". (b) The cumulative capacity as a function of effective rate, extracted from the "signature curve". (c) Capacity versus effective rate data mapped onto the universal theoretical curve from Ref. [5] after obtaining D_c from a numerical fit (see text for details). This shows a visual measure of fit quality.

first underwent one C/20 cycle followed by a C/40 charge and a short OCV period (this OCV should technically not be included since the voltage drops slightly prior to starting the first "signature curve"; in future protocols it will be replaced with a constant voltage hold). "Signature curves" were then performed in 0.1 V intervals from 4.4 to 3.6 V, and then in a larger 0.6 V interval from 3.6-3.0 V, due to the limited available capacity below 3.5 V.

Each voltage interval has its own capacity versus rate data, shown in Figure 5.12, for which effective rates are determined. Figure 5.12 (a) shows the cumulative capacity extracted from each "signature curve", while Figure 5.12 (b) shows the corresponding capacity normalized to total achieved capacity for each voltage interval. The general shape of the theoretical curve can be seen in these data, particularly in those voltage intervals where the capacity saturated at low rate, from a flat plateau as the rate is decreased. The capacity versus rate data for each voltage interval can be fit to equation 5.6, yielding $D_c(V)$, shown in Figure 5.14(a). After the final "signature curve", the cell is charged back to 4.4 V to ensure that the capacities measured during the sequence of "signature curves" were indeed real and not due to electrolyte reactions

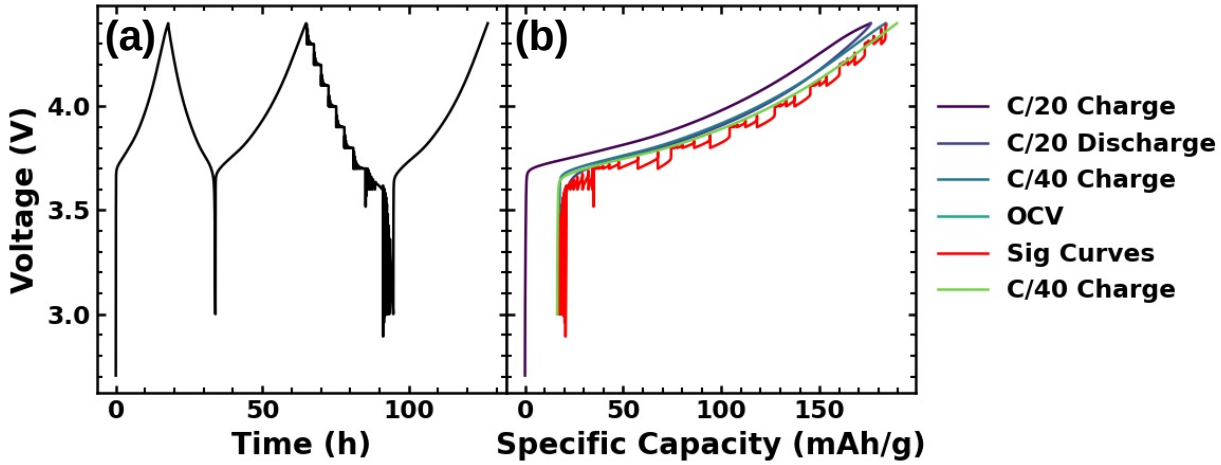

Figure 5.11: Cycler protocol from which state-of-charge dependent D_c can be obtained. (a) Voltage versus time. (b) Voltage versus specific capacity, showing the various protocol steps with different colors. The entire sequence of "signature curves", performed in 0.1 V intervals from 4.4 to 3.6 V, and in one 0.6 V interval from 3.6 to 3.0 V, is shown in red.

at the electrode surfaces or capacitive effects. By recovering all of the capacity extracted during the sequence of "signature curves" in the following charge, one can trust that the measured capacities within each voltage interval are representative. However, as already mentioned, capacity versus rate data obtained from "signature curves" within small voltage intervals can be skewed due to impedance effects; the following discussion addresses fit and data quality checks.

The first and clearest way of judging fit quality is by visually inspecting how well the fitted data (red circles), mapped onto the dimensionless fractional capacity (τ) — fractional time (Q) space, overlay on the universal theoretical curve (black line) shown in Figure 5.9. Figure 5.13 shows two extreme cases; Figure 5.13 (a) shows data that fit poorly while Figure 5.13 (b) shows data that fit excellently. In the first case, the curvature in the measured data is positive and resembles only the region of the theoretical curve where Q is small. In this case, the apparent maximum achievable capacity, if the data were to follow the theoretical curve, should be much larger than the capacity achieved at the lowest rate (right-most red circle), which was erroneously deemed as the maximum achievable capacity, q_{max}, during the fitting procedure. Conversely, Figure 5.13 (b) shows data starting near mid-way along the

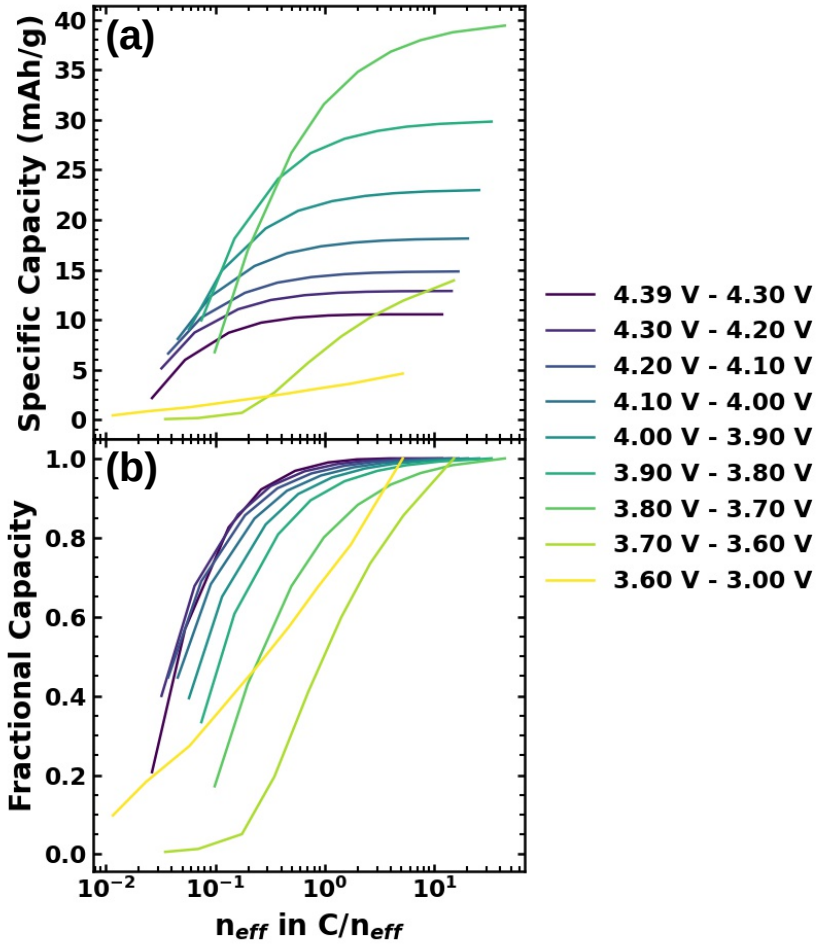

Figure 5.12: Capacity versus effective rate data extracted from the "signature curve" sequence shown in Figure 5.11. (a) Specific capacity versus effective rate. (b) Fractional capacity, normalized using the total achieved capacity within the corresponding voltage interval, versus effective rate.

theoretical curve with negative curvature and fully saturating capacity at large Q (low rate). Obtaining data that follows the upper part of the theoretical curve, where capacity saturates, is the clearest indication that the measured data, and resulting fits, are reliable. Plots such as those shown in Figure 5.13 are always generated so that fits can be visually inspected.

Figure 5.14 summarizes the fitting procedure for data extracted from the advanced signature curve protocol shown in Figure 5.11. Panel (a) shows the fitted Li chemical diffusion coefficient, D_c, as a function of the voltage. In this example, the point centered at 3.3 V, corresponding to the 3.0 - 3.6 V interval, seems like an outlier;

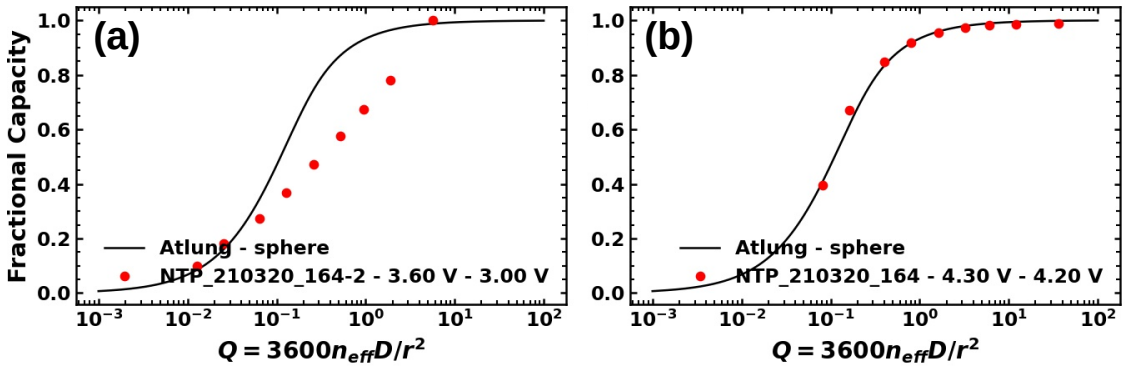

Figure 5.13: Fitted data extracted from the protocol shown in Figure 5.11, mapped into the universal theoretical curve from Ref. [5], demonstrating (a) a poor fit and (b) a good fit. The red circles correspond to measured data that have fit to equation 5.6, while the black line shows the universal theoretical curve.

the trend in D_c as the voltage increases from 3.6 to 4.4 V is otherwise very smooth. Indeed, the fit error shown in Figure 5.14 (b) for this voltage range is at least three times larger than the other points. The fit error is calculated as the average of the absolute difference between the fitted data and the theoretical curve, shown in Figure 5.13, (i.e. the difference between the red points and the black line) weighted by their respective IR voltage drops.

The least-squares optimization to obtain best fit parameters D_c and q_{max} is also weighted by the relative magnitudes of the IR voltage drops. For example, imagine that a "signature curve" was performed with n discharge currents within a particular voltage interval. Each discharge current has a corresponding IR contribution to the voltage, $(IR)_i$, as soon as the current is turned on following an OCV period. Each capacity-rate pair, $1, .., N$, is then assigned a weight,

$$\begin{aligned} w_i &= \frac{\sum_j (IR)_j - (IR)_i}{\sum_k \left[\left(\sum_j (IR)_j \right) - (IR)_k \right]} \\ &= \frac{1 - (IR)_i / \sum_j (IR)_j}{N - 1} \end{aligned} \tag{5.7}$$

for $j, k = 1, .., N$. This places more importance on data where IR voltage drops are small, and penalizes data where IR voltage drops are large and measured capacities may be most influenced by cell resistance beyond that of diffusion alone.

Figure 5.14 (e) shows a representation of the IR voltage drops for each "signature curve". For each voltage interval, the lightest grey, tallest bar corresponds to the largest current, or highest rate, and the successively darker grey bars correspond to subsequent smaller currents. The IR contributions to the voltage are scaled by the size of the interval; a fractional IR value of 1.0 would mean that the IR voltage drop was the same as the width of the voltage interval. For this reason, the fractional IR values for the 3.0-3.6 V interval are smaller than all other voltage intervals only because this interval width is 6 times larger. Of course, the voltage interval width must be considered when interpreting these data, but they provide a nice visual for assessing how IR contributions to the voltage may have affected capacity measurements.

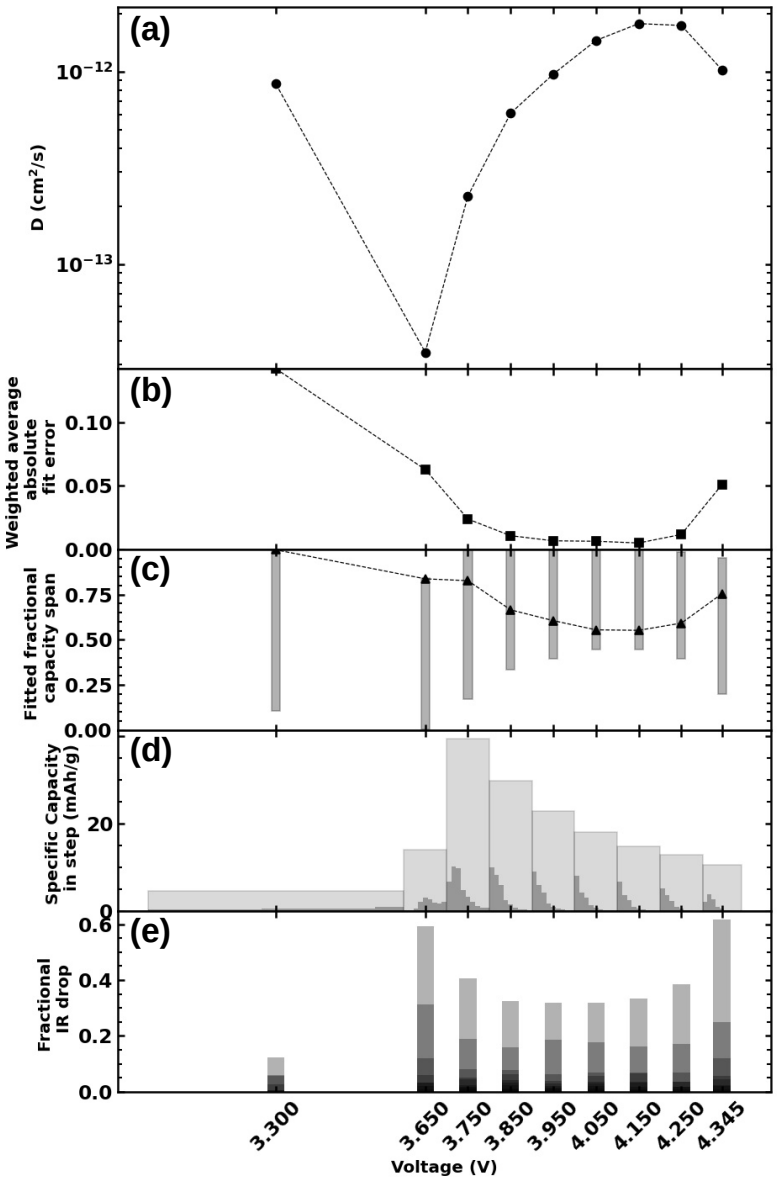

Figure 5.14: $D_c(V)$ summary graph, showing various quantities related to the numerical fits versus voltage. (a) Fitted Li chemical diffusion coefficient. (b) Fit error measured as the difference between the fitted data and the universal theoretical curve shown in Figure 5.13, weighted by the normalized magnitudes of IR contributions to the voltage. (c) The fractional capacity span of the fitted data. The grey bars span the minimum and maximum values of the fitted data while the black triangles show the length of the grey bars. (d) Visualization of the measured capacities during the "signature curve" sequence. The thin dark grey bars show the capacity obtained at each rate within each voltage interval, while the tall light grey bars show the total cumulative capacity achieved during each voltage interval. For each voltage interval, the sum of each of the dark grey bars gives the value of their corresponding light grey bar. (e) The IR contributions to the voltage normalized by the size the voltage interval. The lightest grey bar corresponds to the highest rate, and progressively darker bars correspond to progressively lower rates. Taken together, quality of fits can be judged from these data.

Figure 5.14 (c) shows the fractional capacity spanned according to the fitted parameter q_{max}; the grey bars show which portion of the capacity range is covered, with 1 corresponding to the top of the theoretical curve, and 0 to the bottom, while the black triangles correspond to the length of the grey bars — in other words to the fraction of the fractional capacity covered by the fitted data. It was previously mentioned that in general it is important for the capacity to saturate at the lowest rates, which translates to the grey bars touching the top of this graph, where the fractional capacity equals 1.

Figure 5.14 (d) shows raw data; the measured specific capacities in each step. The wider light grey bars show the total cumulative capacity achieved after the final, slowest discharge step for each voltage interval. Contained within the wider bars are thin, dark grey bars, that show the measured capacities for each rate (or current) within their respective voltage intervals. Stacking each thin dark grey bar on top of each other gives the height of the light grey bar for that voltage interval. The general shape of the capacity versus rate data can be gleaned from these data; if the dark grey bars taper off from left to right (high to low rate), then the capacity saturated and the upper part of the theoretical curve from Figure 5.9 should be matched well.

Figure 5.14 shows a general trend; the fit error (b) is smaller in those voltage intervals where the fitted fractional capacity span (c) reaches 1 and the IR contribution to the voltage (e) is smallest. Overall, Figure 5.14 provides a quantitative and qualitative summary of the fitted data, providing interpretability for users.

5.2.3 Cation mixing and Li diffusion

Figure 5.15 has been adapted from Zhang *et* al. [89] to demonstrate the potential impact on Li kinetics of Ni atoms in the Li layers of Ni-rich NMC materials. Three series of NMC materials were considered: $LiNi_{0.6}Mn_{0.4-x}Co_xO_2$ for $x = 0, 0.1, 0.2$ (red, left panels), $LiNi_{0.9-x}Mn_xCo_{0.1}O_2$ for $x = 0.1, 0.2, 0.25$ (blue, center panels), and $LiNi_{0.8}Mn_{0.2-x}Co_xO_2$ for $x = 0, 0.1, 0.2$ (green, right panels). The top row shows the first discharge specific capacity (1^{st} DC), the second row shows the first cycle irreversible capacity (1^{st} IRC) — defined as the difference between the first charge and discharge capacities, the third row shows the 1^{st} IRC percentage, and the last row shows the percentage of Ni atoms occupying sites in the Li layers ($\%Ni_{Li}$) —

generally called cation mixing because some Li atoms also occupy TM sites in order to maintain electro-neutrality. This quantity is obtained from diffraction measurements and varies depending on material composition. The trend in $\%Ni_{Li}$ is clear: as the Co content increases, the $\%Ni_{Li}$ dereases. Panels (a4) and (c4) have Co content increasing from left to right, while panel (b4) has Co content increasing from right to left. In all three cases, the $\%Ni_{Li}$ decreases as the Co content increases. Interestingly, the 1st IRC also decreases as the Co content increases. There appears to be a nice correlation between 1st IRC% and $\%Ni_{Li}$, seen between panels (a3)-(a4), (b3)-(b4), and (c3)-(c4). It has been shown that the name "IRC" is misleading; the difference between the first charge and discharge capacities can often be partially recovered by either cycling at lower rate, or at higher temperature [51, 60], meaning that it is not irreversible at all, rather, that is due to kinetic limitations. Consequently, the correlation between 1st IRC and $\%Ni_{Li}$ clearly seen in Figure 5.15 suggests that Ni atoms in the Li layers worsen Li kinetics. The work presented in this section employed the AMID to understand how $\%Ni_{Li}$ influences Li kinetics. The experimental components of the work presented in this section (material synthesis, coin cell builds, and AMID measurements) were performed by colleagues Nutthaphon Phattharasukapun and Erin Lyle and was published in Ref. [69].

$LiNiO_2$ is always off-stoichiometric; there is some mixing between the Ni and Li layers where the Ni content is typically greater than the Li content. In NMC and NCA materials, whose parent material is $LiNiO_2$, the $\%Ni_{Li}$ varies depending on the amount of substituents. For example, substituting Mn for Ni causes more cation mixing, while substituting Co for Ni reduces the amount of cation mixing, particularly if Mn is also substituted for Ni, as shown in Figure 5.15. In this section, Li chemical diffusion coefficient measurements are presented for a series of Li-deficient $LiNiO_2$ materials; $Li_{1-x}Ni_{1+x}O_2$ for $x = 0.0, 0.01, 0.02, 0.03, 0.04, 0.05, 0.6$. During synthesis, the corresponding Li/Ni ratios were 1.02, 0.98, 0.96, 0.94, 0.92, 0.9, 0.88, leading to 1.5, 1.9, 2.5, 2.9, 4.3, 5.5, 5.8 $\%Ni_{Li}$, respectively. Due to Li-deficiency during synthesis, except for the Li/Ni 1.02 material, a negligible number of Li atoms could occupy Ni sites, so the excess Ni must occupy Li sites — this has been shown in the literature. [49] This series of materials provides an opportunity to systematically investigate the role of Ni atoms occupying Li sites.

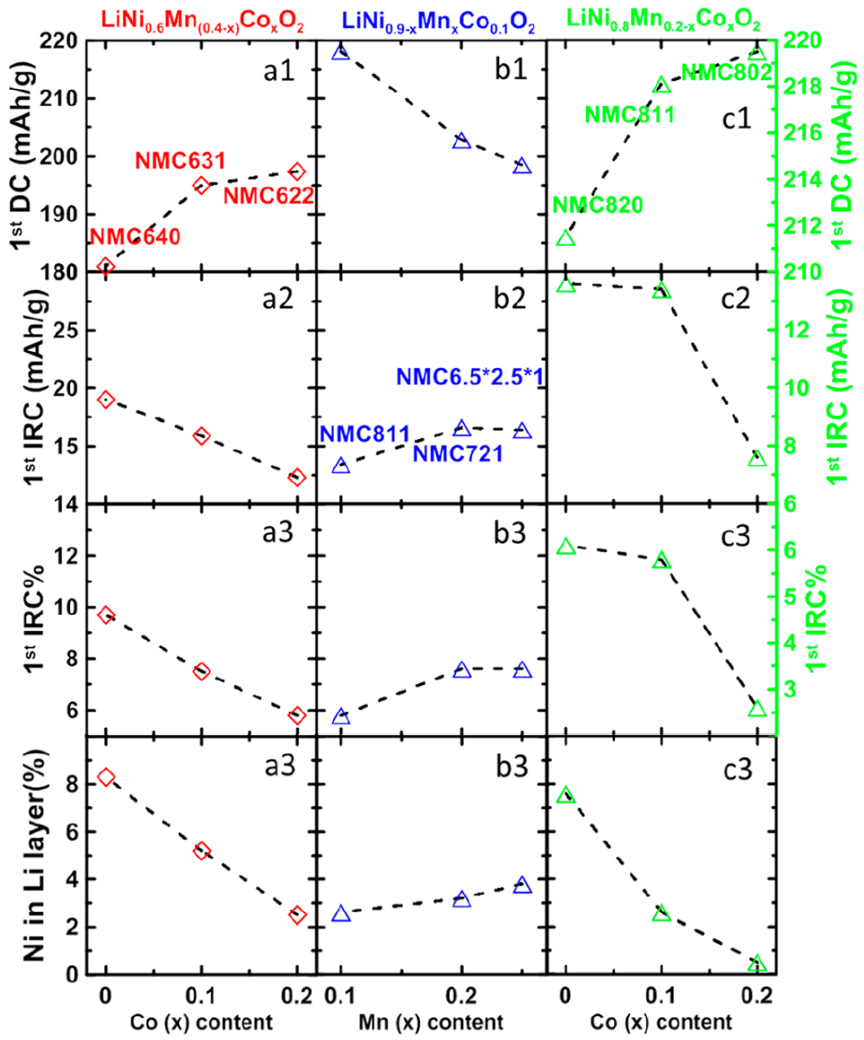

Figure 5.15: Adapted from Ref. [89]. Showing the relationship between the percentage of Ni atoms in the Li layers ($\%Ni_{Li}$), and the apparent irreversible capacity (IRC) for three series of $LiNi_xMn_yCo_zO_2$ ($x + y + z = 1$) materials. The (a) column shows a fixed fractional Ni content of 0.6 with Mn progressively substituted for Co, the (b) column shows a fixed fractional Co content of 0.1 while Ni is progressively substituted for Mn, and the (c) column shows a fixed Ni content of 0.8 while Mn is progressively substituted for Co.

To maintain electro-neutrality as additional Ni atoms occupy Li sites, a corresponding amount of Ni^{3+} is reduced to Ni^{2+}, according to the formula $Li_{1-y}Ni^{2+}_{y}[Ni^{3+}_{1-y}Ni^{2+}_{y}]O_2$. If Ni^{3+} is the only electrochemically active species, then the capacity of a material with y $\%Ni_{Li}$ should be diminished by $2y$ %. Figure 5.16 is taken from Ref. [69] and shows the voltage versus specific capacity profiles for the entire series of materials. In each panel, the LNO material synthesized with a Li/Ni ratio of 1.02 is shown with a black line, for reference, while the Li-deficient material, denoted by its Li/Ni ratio, is shown with a red line. Pair cells are shown with solid and dashed lines in all cases. Firstly, observe the monotonic decrease in specific capacity as the Li/Ni ratio decreases, or, equivalently, as the $\%Ni_{Li}$ increases. The amount by which the specific capacity is decreased follows closely the relationship expected by charge balance; the percent capacity decrease is roughly twice the $\%Ni_{Li}$. Secondly, observe the increasing 1st IRC as the $\%Ni_{Li}$ increases; from Figure 5.16(a)-(f), the difference between the charge and discharge capacities increases. This point is illustrated in Figure 5.17 (adapted from [69]) where the 1st IRC% and $\%Ni_{Li}$ are plotted together against the Li/Ni ratios. Both quantities follow each other closely as the Li/Ni decreases; the 1st IRC% clearly increases as more Ni atoms occupy Li sites, suggesting increasing kinetic limitations and motivating a quantitative investigation of Li kinetics using the AMID.

Figure 5.18 shows the Li ion chemical diffusion coefficient, D_c, as a function of voltage at 20, 30, and 40 °C, obtained from the AMID. Voltage intervals of 0.1 V were used from 4.3 to 3.6 V, while a 0.6 V interval was used from 3.6 to 3.0 V. Data is shown with black circles for the LNO material with a Li/Ni ratio of 1.02 (1.5 $\%Ni_{Li}$), green squares for Li/Ni 0.98 (1.9 $\%Ni_{Li}$), green circles for Li/Ni 0.96 (2.5 $\%Ni_{Li}$), blue squares for Li/Ni 0.94 (2.9 $\%Ni_{Li}$), blue circles for Li/Ni 0.92 (4.3 $\%Ni_{Li}$), red squares for Li/Ni 0.9 (5.5 $\%Ni_{Li}$), and red circles for Li/Ni 0.88 (5.8 $\%Ni_{Li}$). The trend is clear, as the $\%Ni_{Li}$ increases, D_c decreases across the entire voltage range. The most substantial difference in D_c appears to be above 3.6 V. Below 3.6 V, the fractional Li content is close to 1 and the available number of di-vacancies for TSH approaches 0, slowing down diffusion greatly. In this regime, the presence of Ni atoms on Li sites does not hinder Li diffusion as much compared to regions where an appreciable number of di-vacancies may exist. Above 4.2 V, D_c falls by at least one order of magnitude

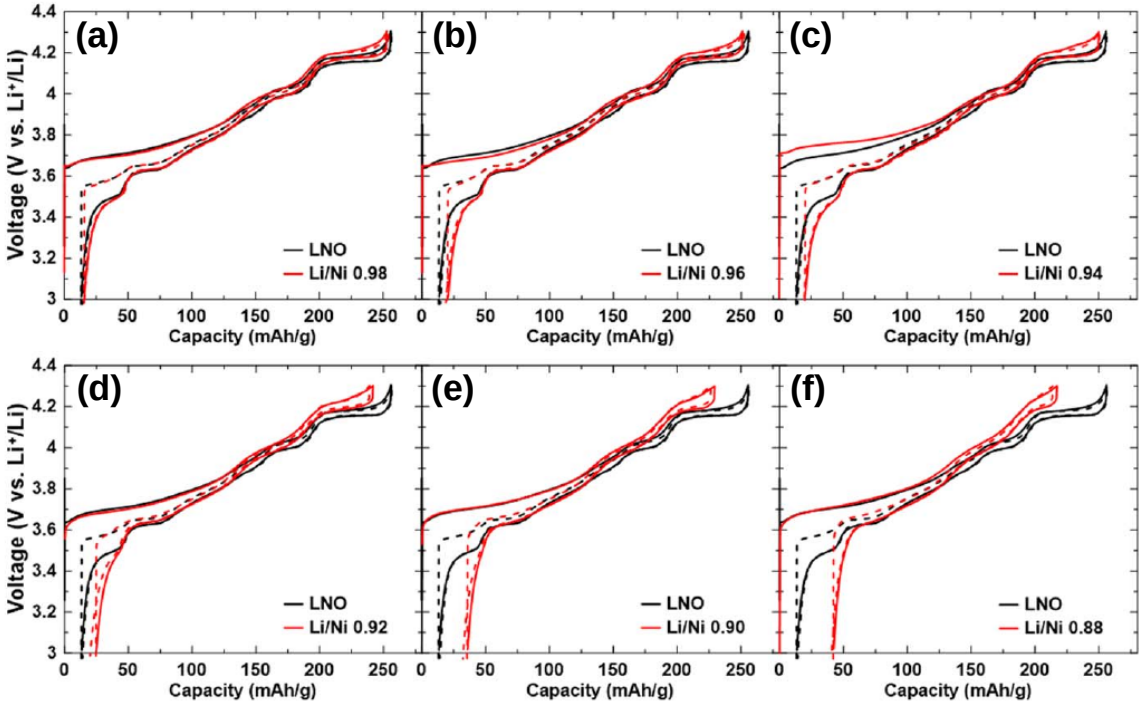

Figure 5.16: Taken from Ref. [69]. Voltage versus specific capacity for a Li-deficient series of materials where the Li/Ni ratio used during synthesis was varied. A smaller Li/Ni ratio implies more Li deficiency, leading to a larger percentage of Ni atoms in the Li layers ($\%Ni_{Li}$). In all panels, the black line corresponds to a typical $LiNiO_2$ (LNO) material. (a) Li/Ni 0.98, 1.9 $\%Ni_{Li}$, (b) Li/Ni 0.96, 2.5 $\%Ni_{Li}$, (c) Li/Ni 0.94, 2.9 $\%Ni_{Li}$, (d) Li/Ni 0.92, 4.3 $\%Ni_{Li}$, (e) Li/Ni 0.90, 5.5 $\%Ni_{Li}$, Li/Ni 0.88, 5.8 $\%Ni_{Li}$.

(this data is not shown at 20 °C because the fits were not reliable). This behaviour has been previously observed and has been attributed to the contraction of the out-of-plane lattice parameter, squeezing the Li layers and increasing the electrostatic repulsion between Li atoms occupying tetrahedral sites and the nearest TM layer. [41] Interestingly, despite a large concentration of di-vacancies at high voltage, the presence of Ni atoms on Li sites hinders diffusion appreciably. Figure 5.19 shows voltage slices of data from Figure 5.18; D_c is plotted against $\%Ni_{Li}$ within various voltage intervals, from 4.2-4.1 V (a) to 3.7-3.6 V (f), measured at 20 (blue), 30 (black), and 40 (red) °C. The influence of the $\%Ni_{Li}$ is most severe in panels (c), (d), and (e) where D_c is decreased by more than one order of magnitude as the $\%Ni_{Li}$ goes from 1.5 to 6; a mere 4.5% increase of Ni atoms on Li sites leads to a drastic hindrance in Li diffusion. If it is assumed that Ni atoms are uniformly distributed on Li sites, the

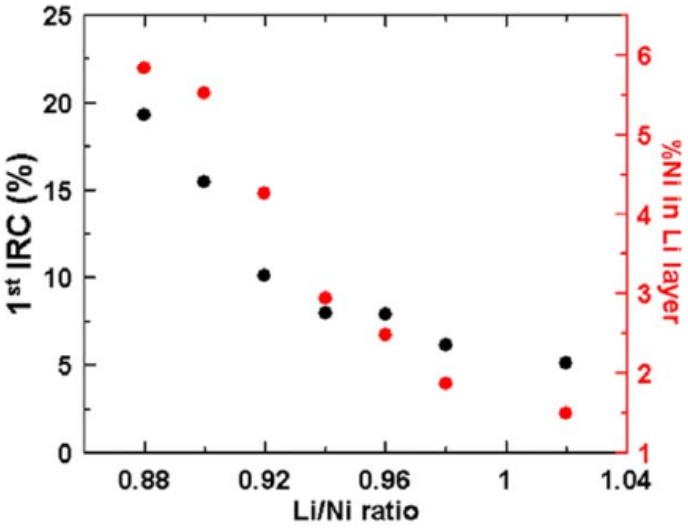

Figure 5.17: Adapted from Ref. [69]. The relationship between the first cycle irreversible capacity (difference between charge and discharge capacities) percentage, and the percentage of Ni atoms in the Li layers.

average number of lattice vectors a Li atom would need to move before encountering a Ni atom will be the fraction of occupied Li by Ni atomx divided by 6; there are 6 directions for Li atoms to travel on a triangular lattice. This means that at 2% occupation, Li atoms would encounter a Ni atom every ~ 8 lattice vectors, whereas at 6% occupation Li atoms would encounter a Ni atom every ~ 2.5 lattice vectors; less than a fourfold difference. The way in which Ni atoms in Li layers alter the site energy landscape must also play a role in hindering diffusion.

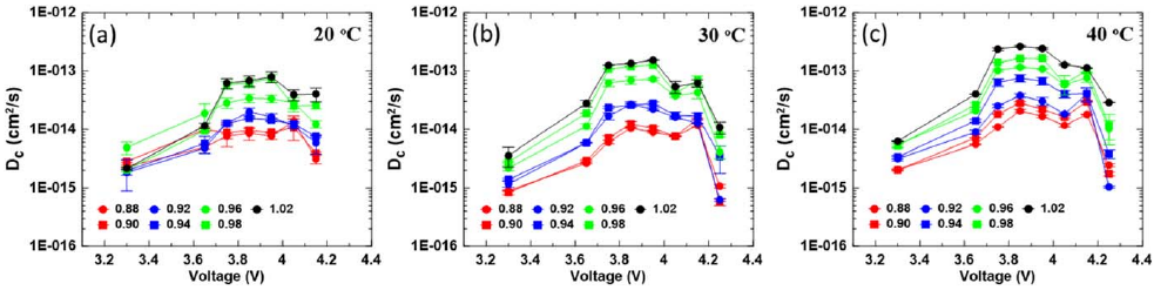

Figure 5.18: Reproduced from Ref. [69]. Measured Li chemical diffusion coefficients, D_c, as a function of voltage for the Li-deficient series of $LiNiO_2$ materials at (a) 20 °C, (b) 30 °C, (c) 40 °C. The Li/Ni ratios for each material are indicated in the legends. A smaller Li/Ni ratio contains a larger percentage of Ni atoms in the Li layers.

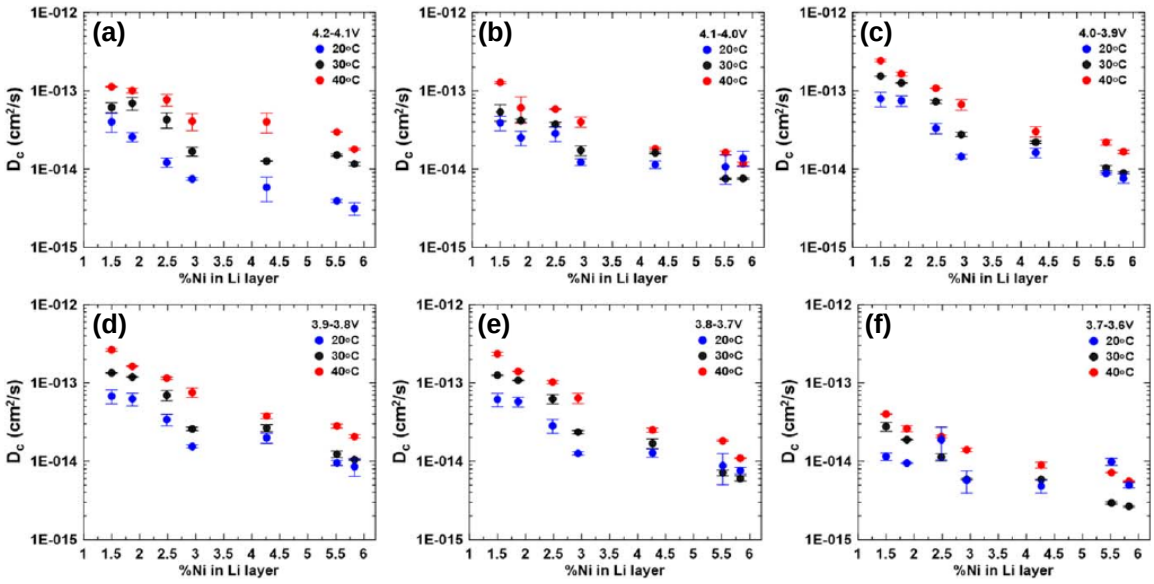

Figure 5.19: Reproduced from Ref. [69]. Measured Li chemical diffusion coefficient, D_c, data from Figure 5.18 plotted versus the percentage of Ni atoms in the Li layers ($\%Ni_{Li}$) for each temperature, within various voltage intervals; (a) 4.2-4.1 V, (b) 4.1-4.0 V, (c) 4.0-3.9 V, (d) 3.9-3.8 V, (e) 3.8-3.7 V, (f) 3.7-3.6 V.

The results of Figures 5.18 and 5.19 are convincing; the presence of Ni atoms in the Li layers of $LiNiO_2$ hinders Li diffusion and will worsen the rate capability of the material. However, Li-deficient LNO materials are not of practical use. In order to validate the observations from Li-deficient materials, Li diffusion measurements using the AMID were also performed on Li-rich $Ni_{0.5}Mn_{0.5}$ materials. This class of material is commercially relevant because it is Co-free and contains a large percentage of Mn, thus is much cheaper than NMC materials.

Figure 5.15 already demonstrated that as the Mn content is increased, so does the $\%Ni_{Li}$. This can be explained using a simple charge balance argument; Mn is preferentially oxidized to 4+ in layered TM oxides, thus reduces a corresponding amount of Ni to 2+, which preferentially occupies Li sites. When excess Li is introduced into the structure, for example in $Li_{1+x}(Ni_{0.5}Mn_{0.5})_{1-x}O_2$, a minimum fraction of x TM sites must be occupied by Li atoms. In this case, for each Li atom occupying a TM site, two Ni^{2+} atoms must be oxidized to Ni^{3+} in order to maintain charge balance. The increased percentage of Ni^{3+}, along with the increased stoichiometric Li content, reduces the $\%Ni_{Li}$.

Figure 5.20(a) shows measured values of D_c versus voltage, from 3.6 to 4.4 V in 0.1 V intervals, for $Li_{1+x}(Ni_{0.5}Mn_{0.5})_{1-x}O_2$ for $x = 0.0$ (red), 0.04 (blue), 0.08 (black), 0.12 (green) measured at 30 °C. It is immediately apparent that as the fraction of excess Li, x, increases, D_c also increases. The largest improvement in D_c is seen as x goes from 0.0 to 0.04, while D_c appears to plateau beyond $x = 0.08$. Figure 5.20 (b) plots the same data as panel (a) versus the $\%Ni_{Li}$ for various voltage intervals — 4.2-4.1 V (red), 4.1-4.0 V (blue), 4.0-3.9 V (black), and 3.8-3.9 V (green). As x goes from 0.12 to 0.0, the $\%Ni_{Li}$ ranges from $\sim 5\%$ to $\sim 10\%$ and D_c varies by about one order of magnitude for all voltages above 3.8 V. This result is very similar to the one observed for Li-deficient materials; approximately one order of magnitude increase in D_c is obtained for a $\sim 5\%$ decrease in Ni atoms in the Li layers. This is a striking result that should be taken seriously by cell and material manufacturers alike who employ the cost reduction strategy of removing Co and increasing the Mn content.

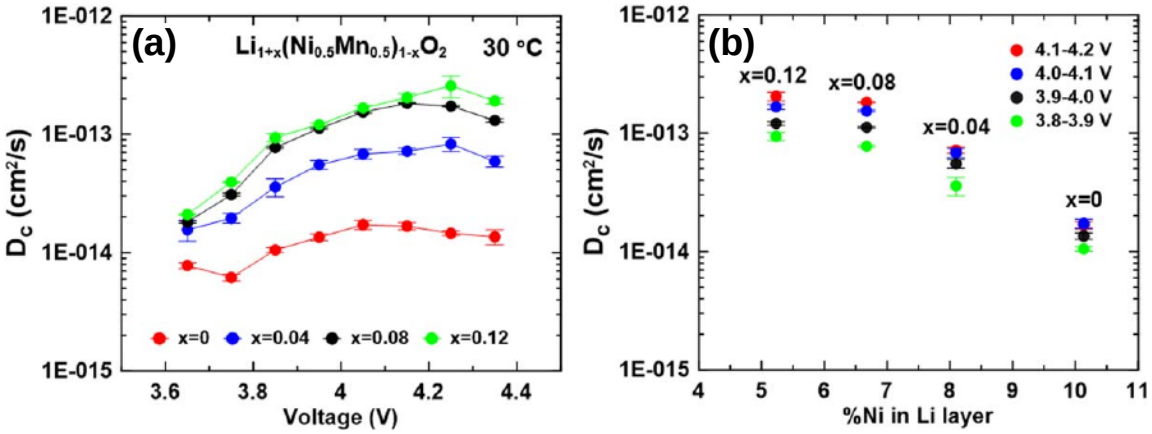

Figure 5.20: Taken from Ref. [69]. (a) Measured Li chemical diffusion coefficient, D_c, data versus voltage for the Li-excess, $Li_{1+x}(Ni_{0.5}Mn_{0.5})_{1-x}O_2$, series of materials. The various amounts of Li excess, x, are shown in the legend. (b) D_c versus the percentage of Ni atoms in the Li layers ($\%Ni_{Li}$) corresponding to different amounts of Li excess, x (labelled points), for various votlages indicated in the legend. These measurements were performed at 30 °C.

There remains one peculiar observation; the magnitude of D_c for the case of $x = 0$, with ~ 10 $\%Ni_{Li}$, is close to that of the Li-deficient material Li/Ni 0.88, with ~ 6 $\%Ni_{Li}$. Even though $Li(Ni_{0.5}Mn_{0.5})O_2$ does not contain excess Li, the stoichiometric ratios during synthesis enforce that as Ni atoms occupy Li site, Li atoms must occupy

Ni sites — the cations must mix. Comparatively, the Li-deficient materials contain a negligible number of Li atoms on Ni sites. There are then two main differences between the Li-rich and Li-deficient series of materials; the presence of Li in the TM layers, and the presence of Mn in the TM layers. It is conceivable that TM sites occupied by Li atoms could provide inter-layer diffusion pathways that would partially alleviate the diffusion hindrance due to Ni atoms in Li layers. However, an appreciable lowering of the energy barrier associated with Li migration could have a more significant impact.

To investigate this possibility, Li TSH energies were computed from first-principles for various local environments. Computations were carried out using $3 \times 3 \times 1$ repetitions of the hexagonal LNO unit cell, removing two Li atoms from one layer to create a di-vacancy, amounting to 54 O atoms, 26 (or 27) Ni atoms, 1 substituent atom (Ni, Co, Mn, or Li), and 25 additional Li atoms. PAW datasets for Li, O, Ni, Co, and Mn included 1, 6, 10, 9, and 7 valence electrons, respectively. The SCAN+rvv10 exchange and correlation functional was used. A plane-wave energy cut-off of 600 eV and a reciprocal space sampling using 50 **k**-points were sufficient for well converged energies and forces. In all computations, full cell relaxation was performed, allowing lattice vectors and atomic coordinates to relax to the energy minimum.

Figure 5.21 shows computed octahedral and tetrahedral site energies for a di-vacancy TSH in $LiNiO_2$ (black circle) with Co (blue square), Mn (red triangle), or Li (green star) substituted into the TM site that is face sharing with the Li tetrahedron. Below the horizontal axis are depictions that show the migration pathway; the sites occupied by a migrating Li atom are shown in brown, the green octahedra have Li atoms occupying their center, the grey octahedra have Ni atoms occupying their center, the red spheres represent O atoms, and the blue octahedron in each depiction corresponds to the substitutive site. The presence of Co or Mn decreases the energy difference between the tetrahedral and octahedral sites by more than 150 meV, while the presence Li reduces is it by more than 300 meV. At room temperature, these values translate to ~ 6 and ~ 12 k_BT; magnitudes that would appreciably influence hopping rates. The migration path energy is taken relative to the octahedral site energy in this case because the initial and final states are symmetrically equivalent, thus have exactly the same energy. In general, the way in which substituents alter the Li site

energy landscape will also influence Li kinetics. It is thus possible that substitution in TM sites that are vertex sharing could alter the migration path energy. Consequently, this computation set serves merely as an example to highlight that Li migration path energies may be appreciably influenced by various substituents occupying TM sites.

The reduction in migration path energy provided by both Mn and Li could explain the discrepancy observed between Li-deficient Li/Ni 0.88 and $Li(Ni_{0.5}Mn_{0.5})O_2$, where, despite having $\%Ni_{Li}$ different by $\sim 4\%$, similar D_c values were measured. The presence of Mn and Li atoms in the TM layers, according to the simple picture presented in Figure 5.21, would improve Li diffusion. In fact, the $Li_{1.12}(Ni_{0.5}Mn_{0.5})O_2$ material, with 5 $\%Ni_{Li}$, has D_c values as large, and even larger at low and high voltage, as LNO with merely 1.5 $\%Ni_{Li}$. Clearly the presence of Li and Mn in the TM layers is favourable for Li diffusion while the presence of Ni in the Li layers is not.

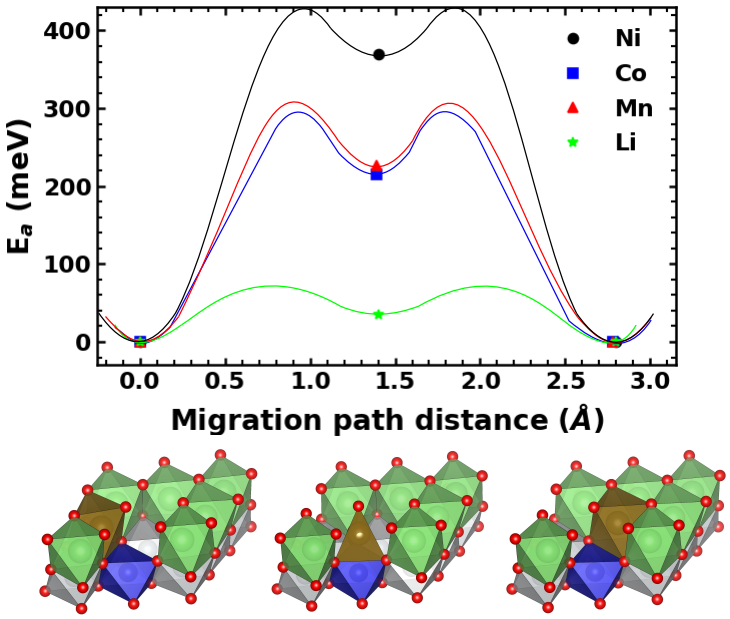

Figure 5.21: Tetrahedral site hop energy barrier for substitutive metals in the transition metal site nearest neighbour to the Li tetrahedral site. The local Li configuration at each step is shown below the graph. The light grey and green octahedra encompass Ni and Li atoms, respectively; the red spheres represent O atoms; and the blue octahedra encompasses the substitutive site that is occupied by either Ni, Co, Mn, or Li. The brown octahedra and tetrahedron encompass the migrating Li atom. The points correspond to energies computed with DFT while the lines were drawn to suggest the energy pathway based on existing literature. [80]

The application of the AMID to quantify the impact of $\%Ni_{Li}$ on Li diffusivity

on both Li-deficient and Li-excess type of materials is a clear example of its utility. Many more similar studies would be of great interest; for example, measurements of D_c throughout cell lifetime for various material compositions could prove valuable for electric vehicle fast charging and high power applications that require long-lived cells.

5.3 Conclusion

In this Chapter, it was shown that Co substitution brings minimal to no benefit to the near-equilibrium electrochemical properties of Ni-rich positive electrode materials. However, Co substitution clearly benefits Li kinetics by reducing the percentage of Ni atoms in the Li layers and lowering the Li migration path energy. A desirable approach to lower the cost of Ni-rich materials is to increase the Mn content, however, Mn substitution promotes cation mixing, leading to a larger $\%Ni_{Li}$ and poor Li kinetics. By adding Co, cation mixing is alleviated, and Li kinetics are substantially improved. This Chapter then demonstrates a practical challenge for eliminating Co from Ni-rich positive electrode materials, particularly in cases where fast charge and/or high power are needed. Further studies on Li diffusivity in Li-excess, Mn containing, Ni-rich materials would prove valuable to understand how the presence of Li in the transition metal layers may improve Li kinetics, providing a potential pathway to Co-free Ni-rich materials with good rate capability.

Chapter 6

Development of cycler data analysis software

Two sets of tools for analysis of experimental cycling data have been developed during the course of this degree: Section 6.1; an application programming interface (API) to automate the analysis of AMID experiments, and Section 6.2; an API that gives access to standard cycling data from various cycler types and enables the development of a graphical user interface (GUI) that can be a "one-stop-shop" for most common analyses of cell data. In order to facilitate discussions around code, examples are given in the form of Jupyter Notebooks which can be thought of as interactive documents made up of blocks, or cells, that blend text (markdown) and computer code execution. Context and instructions can be included using text and code execution can be separated into blocks, facilitating interactivity.

Section 6.1 aims to give the reader a feel for the analysis workflow associated with obtaining Li ion chemical diffusion coefficients from measured data. The code execution requires minimal user input beyond locating the data files to be analyzed, and the functions are amenable to added flexibility in the future.

To parse means to analyze a string of characters or text into its components. Parsing a data file involves separating the data into relevant categories so that operations on that data are facilitated. Section 6.2 presents what began simply as a flexible data file parser that was made into an API to give fine-grained control over data from cells cycled on Neware systems. This API has evolved to handle data from other cyclers by transforming raw data into a common format on-the-fly. This has enabled the development of a GUI that handles multiple file types and, as a result of unifying analyses in one place, is destined to replace existing tools that currently must be used separately.

6.1 The AMID API

Section 5.2.2 described in detail the Atlung Method for Intercalant Diffusion (AMID). In particular, Figure 5.11 offered a visualization of the cycler protocol that enables extraction of Li ion chemical diffusion coefficients, D_c. The general software problem is to automate the data processing workflow as much as possible, without obscuring the underlying electrochemistry. To this end, the developed software automatically parses the measured data into a format that can easily be manipulated, and provides functions to which users must supply inputs in order to obtain D_c as a function of voltage. The code discussed in this section can be found in the GitHub repository https://github.com/mmemcormier/amid.

The AMID API accomplishes three tasks: i) automatically parse the capacity versus rate data from the raw data file output by the cycler, ii) generate plots related to both the measured and fitted data (such as Figures 5.11, 5.12, and 5.14), and iii) fit the extracted capacity versus rate data to equation 5.6.

The data files output by the ultra-high precision coulometry systems (UHPC) are simple comma-separated values with a header containing some information related to the cell. The problem is that the protocol is generally different depending on the cell chemistry. For example, the Li-deficient $Li_{1-x}Ni_{1+x}O_2$ and the Li-rich $Li_{1+x}(Ni_{0.5}Mn_{0.5})_{1-x}O_2$ chemistries discussed in section 5.2.3 had signature curves starting at 4.3 V and 4.4 V, respectively, so the starting voltage were different. Additionally, they each had voltage intervals of 0.1 V down to 3.6 V, and a single 0.6 V interval from 3.6 to 3.0 V, and so each had a different number of voltage intervals. In general, the voltage intervals may even be of different spans, and may not be uniform. The AMID API parser flexibly deals with these issues by inferring the voltage intervals from the raw data. Users do not need to input any information whatsoever about the protocol; the parser does all the work. Additionally, it does not matter whether the sequence of signature curves was performed during charge or discharge, the data are properly parsed in both cases.

Once a data file is parsed, D_c can be extracted for each voltage interval by fitting to equation 5.13. In this case, the user must supply the average primary particle radius of the electrode material. Thus far during the development of the AMID, the primary particle radii have been determined using SEM images and an image processing tool

such as ImageJ. To obtain best fit parameters, a bounded least-squares optimization is performed using the Scipy Python library. [85] As an option, users can specify bounds for D_c that are different from the defaults.

Lastly, there are three graphs that are easily generated with API function calls: i) the protocol visualization, ii) capacity versus effective rates, and iii) the fitting summary graph. At present, the AMID API is most easily used within a Jupyter Notebook. Quite simply, Jupyter Notebooks allow users to interactively run segments of code, called cells, providing output in text, graphs, or other formats. Cells can also be converted to "markdown", a way of writing simple text, to give a Notebook more of a document feel.

Below is an example "amid-analysis" Jupyter Notebook, converted to PDF, that highlights the workflow enabled by the AMID API. Notebook cells that are executing code are highlighted in a grey box with a number in square brackets (e.g., `[1]` — note the different font compared to citations) to its left. The headings here do not have section numbers because the Notebook is inserted as it would appear to a user. As such, the text that appears before and after certain code cells is visible to users and acts as some lightweight documentation, offering some instructions for API calls.

The code cell `[1]` is simply importing the code to enable its use. Preceding code cell `[2]`, a list of the required variables is given, with an explanation as to their purpose. This is where the data file to be analyzed is specified and the location where the analysis output will be saved. Code cell `[3]` instantiates the AMID object; the data file is parsed and all resulting data is organized in memory so it is readily accessible by other functions, and the extracted capacity versus rate data is saved to an excel file, by default, for plotting using other software. Additionally, some text output is printed so that users can check that the protocol and related quantities were inferred correctly. The following two code cells demonstrate how easily the protocol visualization and capacity versus rate plots can be generated. Note that these figures are not numbered and captioned because they are part of the Notebook; in fact, all three figures appearing in the Notebook below are identical to Figures 5.11, 5.12, 5.14. In theory, these function calls are not necessarily needed; they could automatically be called when the AMID object is instantiated (code cell `[3]`), but the implementation shown below makes it easy to add flexibility to the appearance

of each graph via arguments to the functions called in code cells [4] and [5]. At the moment, such functionality has not yet been implemented. Code cell [6] executes a fit of the capacity versus rate data for each voltage interval to equation 5.13. The user must specify the average primary particle radius, in cm, as the first argument to the function; in the case of this example it is 0.5×10^{-4} cm. Optional arguments to the function call are described in the preceding text cell. After executing code cell [6], the fitted values of D_c for each voltage interval are printed, along with the standard deviations calculated from the covariance matrix and the fit error that combines both fitting parameters. The call to the "fit_atlung()" function returns data that must be passed to the "make_summary_graph()" function in code cell [7] in order to create the summary graph. The contents of the summary graph were discussed in detail in relation to Figure 5.14, and serves to provide a summary of important quantities needed to assess fit quality.

It is important to emphasize that obtaining fits and relevant plots for data from AMID measurements requires only typing a few lines and hitting "enter" a few times. Without this software, researchers would need to manually compute the capacities for each step of each signature curve directly from the data files and input into a spreadsheet or similar — there can be more than 80 steps in total; they would need to manually specify the voltage intervals to label corresponding data on graphs; they would need to make each graph, for each cell, every time, using their preferred graphing method. The amount of time this would have taken would have been a near insurmountable hurdle for the development of the AMID, let alone its applications thus far. The AMID API has been used to analyze hundreds of cells in a few minutes each; without it, this analysis may have taken more than a year!

AMID Analysis

Welcome to the AMID analysis Notebook!

The next few blocks, each with very little code, allow easy analysis of AMID data (from Dal and Novonix UHPC files only, for now) with some flexibility for naming files and creating directories without the need to copy the original datafile anywhere.

The text preceeding each cell gives some information on the arguments that can be supplied to the function calls.

Reminder: to run a block press "shift+enter". All blocks with text, like this one, can be run or skipped over.

[1]:
```
from amid import AMID
import matplotlib.pyplot as plt
import numpy as np
import pandas as pd
import warnings
warnings.filterwarnings(action='ignore')
```

Directory structure

dstpath: the location on your computer that will serve as the base directory to save things. On Windows, if it does not start with "C:" then the directory where this notebook is located is used as base.

srcpath: the location on your computer (or remote server if connected via VPN) where the UHPC AMID file is located.

uhpc_file: the name of the AMID UHPC file. Be sure to include the .csv file extension.

cell_label: an identifier for your analysis. If a directory [dstpath]\[cell_label] does not exist, one is created. *cell_label* is also used when saving figures and in legends. This allows users to perform different analyses on the same AMID UHPC file without having to make new directories or copy the datafile anywhere. No matter which operating system (Win, Mac, Linux), use the "/" for separating directories - differences between operating systems are handled internally.

[2]:
```
dstpath = "/home/mcormier/projects/diffusion/analysis/amid-dev-2021/
 ↪Li-rich_Ni50Mn50/"
srcpath = "/home/mcormier/projects/diffusion/analysis/amid-dev-2021/
 ↪Li-rich_Ni50Mn50/"
```

```
uhpc_file = 'NTP.210320.164.csv'
cell_label = 'NTP164_for-thesis'
```

The AMID object

Instantiating the AMID object is easy! The resulting variable (in this case *amid_data*) contains parsed data from the AMID protocol. You should read the output to be sure it is giving the information you expect!

[3]:
```
amid_data = AMID(dstpath, srcpath, uhpc_file, cell_label, export_data=True,␣
↪use_input_cap=True)
```

```
Working on cell: NTP.210320.164
Positive electrode active mass: 0.0011172 g
Input cell capacity: 0.00022344 Ah
Indices being removed to time non-monotonicity: [3528 3576]
First signature curve step: 4
Last signature curve step: 164
Specific Capacity achieved in advanced protocol: 167.18 mAh/g
Using 0.00022344 Ah to compute rates.
Starting voltage: 4.390 V
Ending voltage: 3.000
Found 81 charge or discharge steps in sig curve sequences.
Found 9 signature curves.
Cutoff voltages: [4.3 4.2 4.1 4.  3.9 3.8 3.7 3.6 3. ]
Midpoint voltages: [4.345 4.25  4.15  4.05  3.95  3.85  3.75  3.65  3.3  ]
Voltage intervals widths: [0.09 0.1  0.1  0.1  0.1  0.1  0.1  0.1  0.6 ]
Voltage interval labels: ['4.39 V - 4.30 V', '4.30 V - 4.20 V', '4.20 V - 4.10
V', '4.10 V - 4.00 V', '4.00 V - 3.90 V', '3.90 V - 3.80 V', '3.80 V - 3.70 V',
'3.70 V - 3.60 V', '3.60 V - 3.00 V']
Found 9 voltage intervals.
Done parsing signature curves.
```

Make some plots!

You can now make the standard plots. For each plotting method, figures are saved by default. If you would prefer to not have them saved automatically, you can pass *save=False*. e.g. amid_data.plot_protocol(save=False). All figures get saved in the directory [*dstpath*]\[*cell_label*].

NOTE: in this particular example, there is an OCV step after the discharge step preceeding the signature curves.

ylims: an optional argument to fix y-axis plot bounds. A list with the min and max values for the y-axis bounds. e.g., ylims=[2.95, 4.35].

[4]:
```
amid_data.plot_protocol()
```

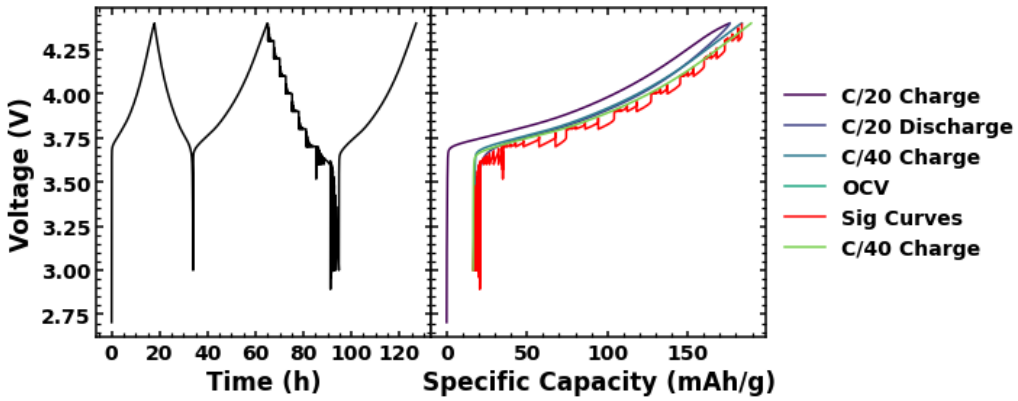

[5]:
```
amid_data.plot_caps()
```

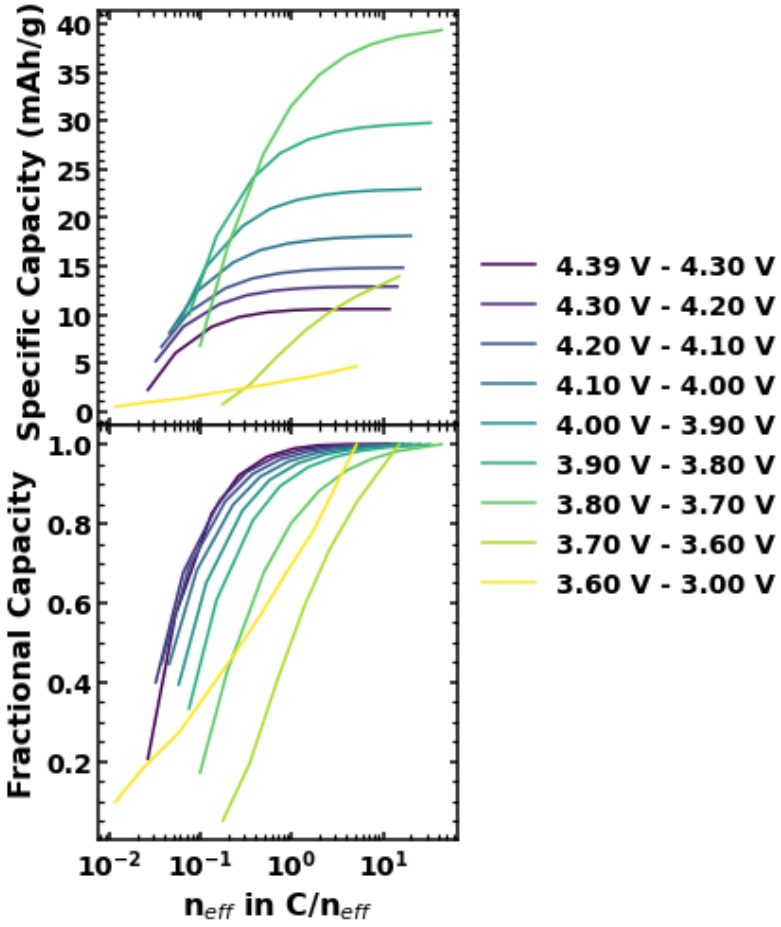

It's time to fit the data!

You must pass the *PARTICLE RADIUS IN CM* to the *fit_atlung()* method. In this example, $r = 0.5\ \mu$m is passed.

Optional arguments:

ftol: the tolerance criteria for the fits. If fits are poor, try making smaller. If a RuntimeWarning is raised, try making larger. You may still get a good fit despite a RuntimeWarning being raised. Defaults to 5e-14.

D_bounds: bounds for D_c. Needs to be a list with the lower and upper bound.

shape: particle geometry. Currently supports "sphere" and "plane". Defaults to "sphere".

nalpha: the number of expansion coefficients to use in the Atlung expression. Default to 150.

nQ : the number of Q values (on a log scale) to use in the theorical Atlung curve, τ vs Q, for comparing fit quality. Default is 2000. There is normally no reason to change this.

save: whether or not to save figures comparing theory to fitted values for each voltage interval. Default is True.

label: an additional label that can be used for saving figures and data. For example, perhaps one wishes to use different particle sizes, then "label=r1" and "label=r2" could be used in 2 separate calls to fit_atlung() and each set of plots would be saved to same directory but each with their corresponding label.

Returns: data needed to make summary graph.

[6]:
```
fit_data = amid_data.fit_atlung(0.5e-4, nalpha=200, ftol=5e-14, save=True,␣
↪D_bounds=[1e-15, 1e-10], label='r-0.5um')
```

```
Fitted Dc: [3.74128018e-12 3.08548990e-12 2.62765342e-12 2.33809606e-12
 1.41181876e-12 4.57943075e-13 4.91434560e-13 6.13358491e-13]
Standard deviations from fit: [0.19537615 0.2042114  0.21897727 0.22795527
0.22495612 0.08928506
 0.18485019 0.06456398]
Atlung fit error: [0.05273032 0.05204843 0.04917678 0.04575091 0.03775727
0.0394653
 0.04966086 0.01679896]
```

Make the summary graph!

Need to pass the returned values from fit_atlung() to this method as the first argument.

Optional arguments:

label: An additional label to saving the figure in case multiple of these are to be generated. Is passed, the same label as when calling fit_atlung() should be used. Default is None.

save: whether or not to save the figure. Default is True

[7]:
```
amid_data.make_summary_graph(fit_data, label='r-2.1um')
```

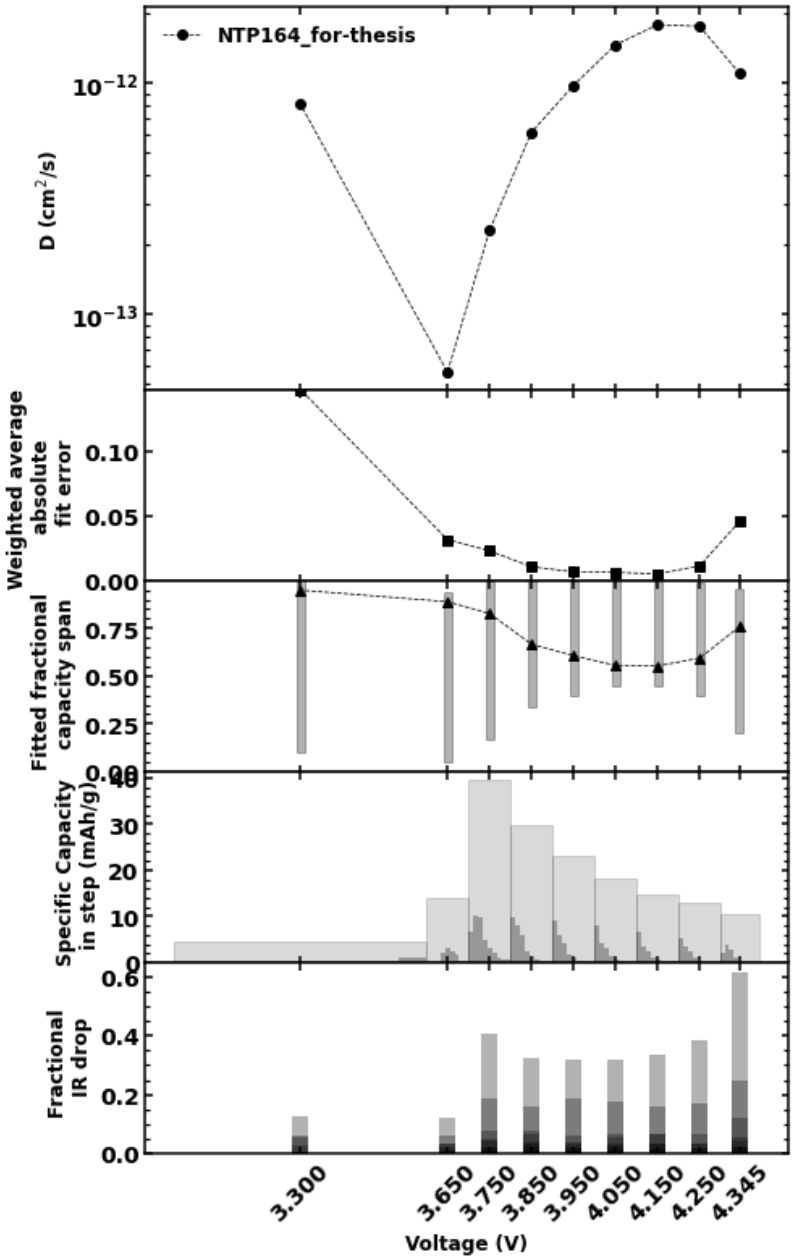

6.2 Cycler Data API and DiVAn

The software development described in this section has laid the foundation for what will hopefully become very useful tools for all members of the Dahn lab and beyond. The basic data problem for any battery research group is as follows: there are a variety of cyclers that each require a local computer to operate its control software and temporarily hold data; these cyclers each have their own data format outputted to some flavour of text file; and text files must be parsed to retrieve data relevant to cell performance. How then should data from various cyclers be unified? The best solution is one that involves hosting a database on a remote server, where cycler data is converted to a common format before being stored in the database. However, without an active maintainer this is not a viable option. The solution taken here is to preserve the native text file format from each cycler, but build parsers for each one that convert the data to a common format on-the-fly each time the code is run. This is clearly not as efficient, but has the advantage of not needing database hosting and maintenance, and a graphical user interface (GUI) can still be built on top of the API. The code base discussed in this section can be found in two GitHub repositories: https://github.com/mmemcormier/cell-explorer and https://github.com/mmemcormier/divan, where the former will be deprecated in favour of the latter.

Yet, there is a problem within the problem; cyclers made by the company Neware are by far the most common in the Dahn lab because they are used for long-term cycling experiments, but they each have a slightly different file format. The entire undertaking laid out in this section is due to a flexible parser that operates on all Neware files without any user input. Some functions to retrieve data and compute quantities commonly used to compare cells were added, forming an API, and the Neware data explorer, in the form of a Jupyter Notebook, was born. Of course this implies that users must run some Python code, or more beneficially, would be able to write some basic Python code themselves, which, for many, is not as convenient as a GUI. However, formulating Neware data as an API allows maximum flexibility for anyone willing and/or able to use it in code. It is important to note that this is not an entirely new problem; there already exists a GUI in the Dahn lab that is used to explore data from Neware cyclers. It also parses all Neware file format types but

the logic employed to do it is hard-coded in a such a way that adapting it for future file formats will be more difficult. The new implementation first parses the header which contains a hierarchy of column labels, then uses those labels to identify which column corresponds to which data. Different files formats have different labels for the same quantities, thus a mapping to convert column labels to a standard set is all that is needed to accommodate new formats. The existing tool is limited in functionality and is written in Visual Basic, thus is poorly amenable to ongoing development. The following discussion will go over an example use-case of the Neware data API within a Jupyter Notebook. A primitive version of a GUI is already implemented and will be discussed afterwards. Section 6.3 will describe ongoing developments.

The example Notebook below serves to show how, with some basic Python programming, a researcher can easily access data from multiple cells, has the flexibility to select specific cycles, has access to common cycling data, and can compute properties related to cell perfomance. This Notebook can also serve as a template, such that minor changes can yield a completely different set of data. The data shown are from cells made and tested by fellow lab member Ahmed Eldesoky. Efforts will not be made to make any sort of inference from the data; the point of the following discussion is to simply give an example of how the API may be used.

The structure of Jupyter Notebooks was introduced in section 6.1 and is followed here. Code cell `[1]` imports standard Python libraries to locate files (pathlib and glob), manipulate data (numpy), and make graphs (matplotlib). The Neware parser with associated functions are contained within the "ParseNeware" object. As in the previous section, each code cell is preceded by a short description of its various components, in order to give an unfamiliar user some instructions. In code cell `[2]`, the data set is defined; the location on the computer where data files are located, the unique cell identifiers, and labels used to annotate figures and label exported figure names are all declared. In this example, six cells are arranged in a 3×2 matrix. Notice that the explicit filenames need not be given; they are retrieved using the Python package "glob", in the following code cell. Code cell `[3]` instantiates the "ParseNeware" object, parsing each data file into memory. The outputted number of cycles and rates can be checked by the user to ensure the code is working properly. The following three code cells show example graphs that can be made. In each case,

a multi-panel figure is setup before invoking function calls to obtain the desired data. Cell `[4]` creates a 3 × 2 panel figure, one panel for each cell, containing voltage versus capacity curves for every 20th C/3 cycle. Notice that the labels defined in code cell `[2]` are annotated in each panel. In this example, the labels correspond to the electrolyte composition and the cycling upper cut-off voltage. A perceptually uniform color scheme is used so that the progression from earlier (purple) to later (yellow) cycles is smooth. The very last line of cell `[4]` is commentted ("#"), but would serve to save the figure. With minimal programming experience, users could easily modify code blocks such as this one. For example, passing `sharey=False` to `plt.subplots()` would turn off sharing of y-axis. Code cell `[5]` creates a figure with the corresponding differential capacities, dQ/dV, versus voltage, but for C/20 cycles only. Any properties of individual figure panels can easily be specified in an $(n \times m)$ array, where n is the number of rows and m is the number of columns in the figure, and used at each iteration. For example, the upper and lower y-limits for each panel could each be stored in $(n \times m)$ arrays and the corresponding elements passed to `set_ylim()` at each iteration. Lastly, code cell `[6]` creates a standard figure that summarizes cell cycling data; capacity, normalized capacity, and normalized ΔV versus cycle number.

Cycle Selector

Welcome to the Neware data explorer!

[1]:
```
import numpy as np
from glob import glob
from pathlib import Path
from reader import ParseNeware
import matplotlib.pyplot as plt
import warnings
warnings.filterwarnings(action='ignore')
```

Setup the data

Set the path to the data files.

Define the cell IDs which appear in the filenames (they are all that is needed to identify the file) in the arrangement wanted - the example below has 3 rows and 2 columns.

cell_labels will be annotated on each panel of the figure later.

comp_label can be appended to figure names when saved.

[2]:
```
p = Path('/home/mcormier/git/cell-expl/data_to_debug/AE_neware_data')

cell_ids = np.array([[143880, 143881],
                     [143882, 143883],
                     [143884, 143885]])

cell_labels = np.array([['2VC + 1DTD 4.06 V', '2VC + 1DTD 4.06 V (pair)'],
                        ['2FEC + 1LFO 4.06 V', '2FEC + 1LFO 4.06 V (pair)'],
                        ['2VC + 1DTD 4.2 V', '2VC + 1DTD 4.2 V (pair)']])

comp_label = 'comparison_for-thesis'

dims = np.shape(cell_ids)
print(dims)
```

```
(3, 2)
```

Load parsed data into memory

The *ParseNeware* object contains parsed data from the Neware text file. For each cell defined in the cell above, the Neware object is added to a list to be used later.

ParseNeware must be supplied the path and name of a Neware file. Optionally, a reference capacity, *ref_cap*, can be supplied to compute the correct rates.

[3]:
```
nd_list = []
for i in range(dims[0]):
    nd_list.append([])
    for j in range(dims[1]):
        fpath = p / '*{}*.txt'.format(cell_ids[i,j])
        pstr = fpath.absolute().as_posix()
        fname = glob(pstr)[0]
        print('Loading Neware file {}'.format(fname))
        nd = ParseNeware(fname, ref_cap=220)
        nd_list[i].append(nd)
```

```
Loading Neware file /home/mcormier/git/cell-expl/data_to_debug/AE_neware_data/AE
_CYC_143880_Nw_c0_406V_20C_C3C3_201002_BTR_A_127.0.0.1_240047_1_1.txt
Found 1138 cycles.
Found charge C-rates: ['C/3', 'C/20']
Found discharge C-rates: ['C/3', 'C/20']
Loading Neware file /home/mcormier/git/cell-expl/data_to_debug/AE_neware_data/AE
_CYC_143881_Nw_c0_406V_20C_C3C3_201002_BTR_A_127.0.0.1_240047_1_3.txt
Found 1141 cycles.
Found charge C-rates: ['C/3', 'C/20']
Found discharge C-rates: ['C/3', 'C/20']
Loading Neware file /home/mcormier/git/cell-expl/data_to_debug/AE_neware_data/AE
_CYC_143882_Nw_c0_406V_20C_C3C3_201002_BTR_A_127.0.0.1_240047_1_6.txt
Found 1129 cycles.
Found charge C-rates: ['C/3', 'C/20']
Found discharge C-rates: ['C/3', 'C/20']
Loading Neware file /home/mcormier/git/cell-expl/data_to_debug/AE_neware_data/AE
_CYC_143883_Nw_c0_406V_20C_C3C3_201002_BTR_A_127.0.0.1_240047_1_8.txt
Found 1112 cycles.
Found charge C-rates: ['C/3', 'C/20']
Found discharge C-rates: ['C/3', 'C/20']
Loading Neware file /home/mcormier/git/cell-expl/data_to_debug/AE_neware_data/AE
_CYC_143884_Nw_c0_42V_20C_C3C3_201002_BTR_A_127.0.0.1_240047_2_1.txt
Found 923 cycles.
Found charge C-rates: ['C/3', 'C/20']
Found discharge C-rates: ['C/3', 'C/20']
Loading Neware file /home/mcormier/git/cell-expl/data_to_debug/AE_neware_data/AE
_CYC_143885_Nw_c0_42V_20C_C3C3_201002_BTR_A_127.0.0.1_240047_2_4.txt
Found 906 cycles.
Found charge C-rates: ['C/3', 'C/20']
Found discharge C-rates: ['C/3', 'C/20']
```

Make a Voltage versus Capacity figure

In this example, every 20th C/3 cycle is shown. This is captured in the variable *cycnums*.

Note the function calls:

select_by_rate: selects only the cycles with the specified rate.

get_vcurve: obtains the capacity and voltage for a particular cycle number.

[4]:
```
fig, axs = plt.subplots(nrows=dims[0], ncols=dims[1], sharex=True, sharey=True,
                        figsize=(3*dims[1], 3*dims[0]),
                        gridspec_kw={'hspace':0.0, 'wspace':0.0})

for i in range(dims[0]):
    for j in range(dims[1]):

        nd = nd_list[i][j]

        selected_cycs = nd.select_by_rate('C/3', cyctype='cycle')
        cycnums = selected_cycs[3::20]
        colors = plt.get_cmap('viridis')(np.linspace(0,1,len(cycnums)))
        for n in range(len(cycnums)):
            # V-Q curves
            cap, volt = nd.get_vcurve(cycnum=cycnums[n], cyctype='cycle')
            axs[i,j].plot(cap, volt, color=colors[n], label='cycle {}'.
 ↪format(cycnums[n]))

        # Figure params for V-Q
        axs[-1,j].set_xlabel('Capacity (mAh)')
        axs[i,0].set_ylabel('Voltage (V)')

        axs[i,j].annotate('{}'.format(cell_labels[i,j]), xy=(0.12, 0.1),␣
 ↪xycoords='axes fraction', fontsize=11)
        axs[i,j].tick_params(direction='in', top=True, right=True)
#plt.savefig(p / 'V-Q_{}.jpg'.format(comp_label), bbox_inches='tight')
```

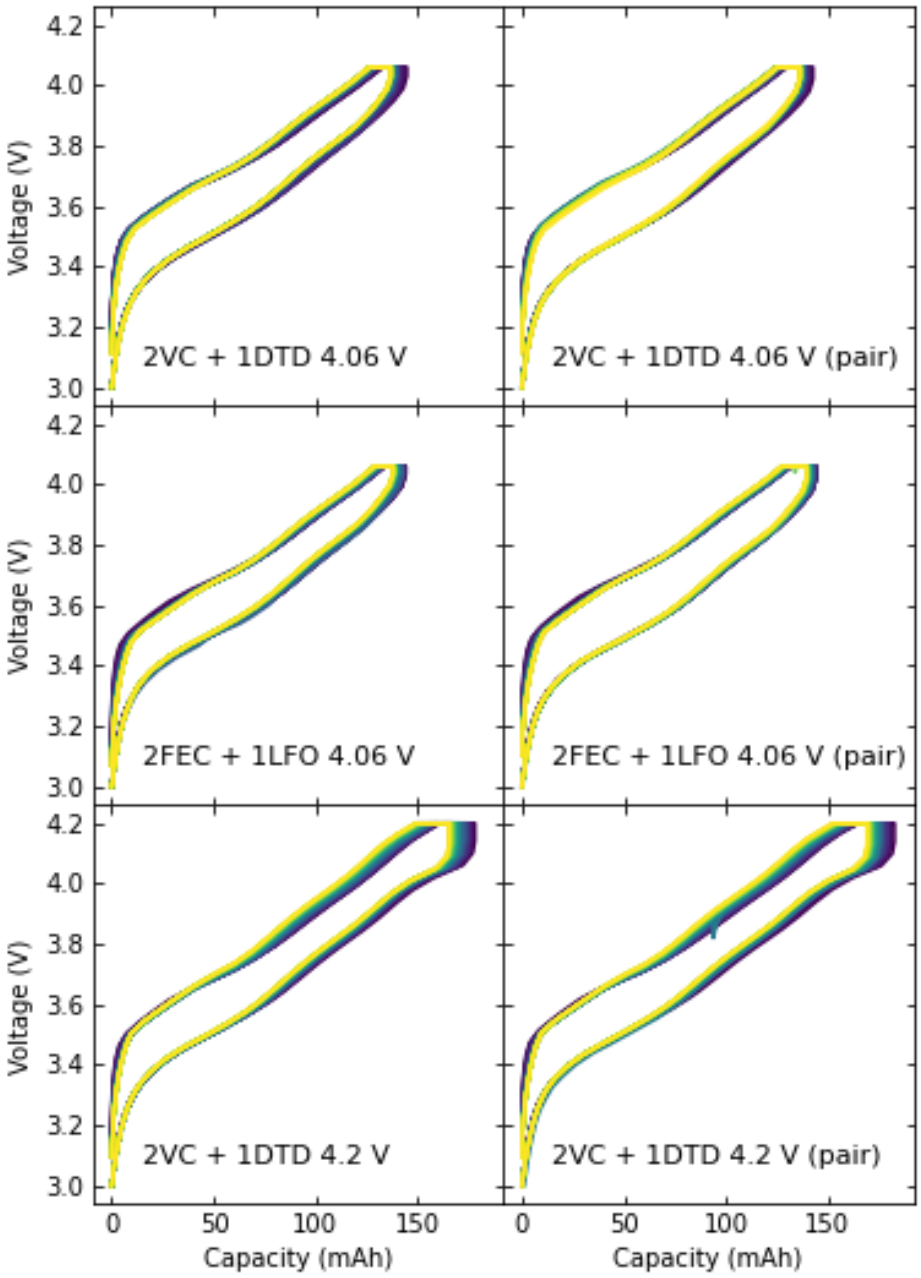

Make corresponding dQ/dV versus Voltage figure.

In this case, only the C/20 cycles are selected for dQ/dV. Note the function calls:

select_by_rate: selects the C/20 cycles.

get_dQdV: computes the numerical derivative of Capacity versus Voltage. It optionally smooths the results with a running average of width "avgstride".

[5]:
```
fig, axs = plt.subplots(nrows=dims[0], ncols=dims[1], sharex=True, sharey=True,
                        figsize=(3*dims[1], 3*dims[0]),
                        gridspec_kw={'hspace':0.0, 'wspace':0.0})


for i in range(dims[0]):
    for j in range(dims[1]):

        nd = nd_list[i][j]

        selected_cycs = nd.select_by_rate('C/20', cyctype='cycle')
        cycnums = selected_cycs[:-1]
        colors = plt.get_cmap('viridis')(np.linspace(0,1,len(cycnums)))
        for n in range(len(cycnums)):

            # dQ/dV
            voltage, dQdV = nd.get_dQdV(cycnum=cycnums[n], avgstride=5)
            axs[i,j].plot(voltage, dQdV, color=colors[n], label='cycle {}'.
 ↪format(cycnums[n]))

        # Figure params for dQ/dV
        axs[-1,j].set_xlabel('Voltage (V)')
        axs[i,0].set_ylabel('dQ/dV (mAh/V)')
        axs[i,j].set_ylim(-490, 490)

        axs[i,j].annotate('{}'.format(cell_labels[i,j]), xy=(0.12, 0.1),␣
 ↪xycoords='axes fraction', fontsize=11)
        axs[i,j].tick_params(direction='in', top=True, right=True)
#plt.savefig(p / 'dQdV_{}.jpg'.format(comp_label), bbox_inches='tight')
```

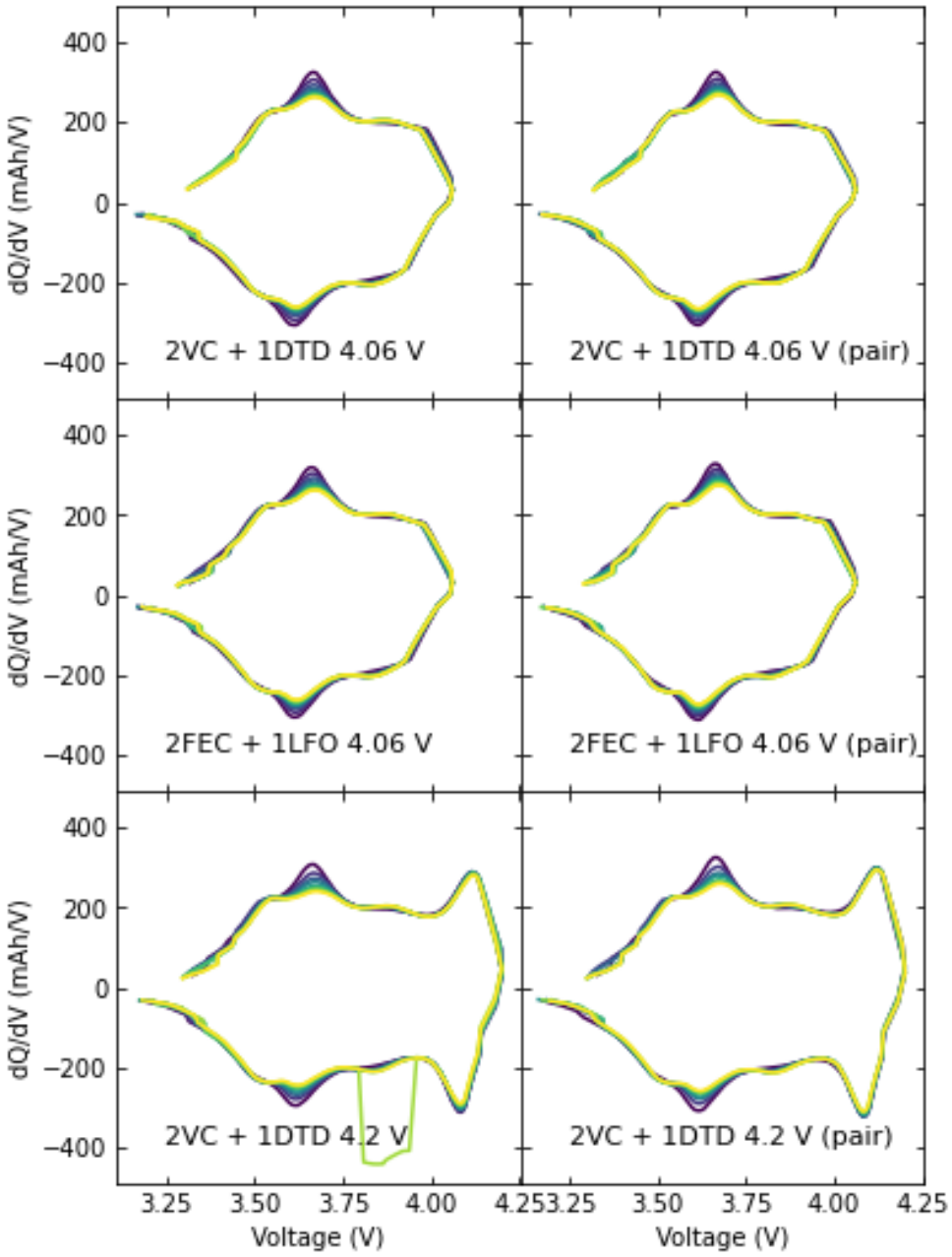

Make the standard Capacity, Normalized Capacity, and ΔV versus cycle number figure.

Note the function calls:

get_discap: is called twice: i) to get the absolute capacity, and ii) to normalize by the 5th cycle.

get_deltaV: computes ΔV as the difference between the charge and discharge average voltages as determined from the mean value theorem (integrated V-Q) and, in this case, normalizes to the 10th cycle.

[6]:
```
fig, axs = plt.subplots(nrows=3, ncols=1, sharex=True,
                        figsize=(4, 10),
                        gridspec_kw={'hspace':0.0, 'wspace':0.0})
ids = cell_ids.flatten()
nds = [n for ndl in nd_list for n in ndl]
labels = cell_labels.flatten()


colors = plt.get_cmap('rainbow')(np.linspace(0,1,len(ids)))
markers = ['o', 's', '^', '*', 'd', '+']
for i in range(len(ids)):

    nd = nds[i]

    # Capacity curves
    cyc_id, dcap = nd.get_discap()
    axs[0].plot(cyc_id, dcap, '{}'.format(markers[i]), color=colors[i],␣
 ↪label=labels[i], markersize=4.0)
    cyc_id, dcap = nd.get_discap(normcyc=5)
    axs[1].plot(cyc_id, dcap, '{}'.format(markers[i]), color=colors[i],␣
 ↪label=labels[i], markersize=4.0)

    # Delta V
    selected_cycs = nd.select_by_rate("C/3", cyctype='cycle')
    cyc_id, dV = nd.get_deltaV(normcyc=10, cycnums=selected_cycs)
    axs[2].plot(cyc_id, dV, '{}'.format(markers[i]), color=colors[i],
                label='{0}'.format(labels[i]), markersize=4.0)

# Figure params for capacity curves
axs[0].set_ylabel('Capacity (mAh)')
axs[1].set_ylabel('Normalized Capacity (mAh)')
axs[2].set_ylabel(r'$\Delta V / \Delta V_{10}$')

axs[-1].set_xlabel('Cycle number')

axs[1].set_ylim(0.8, 1.1)
axs[2].set_ylim(0.8,1.3)

axs[0].legend(frameon=False)
for i in range(3):
    axs[i].tick_params(direction='in', top=True, right=True)

#plt.savefig(p / 'cap-dV_{}.jpg'.format(comp_label), bbox_inches='tight')
```

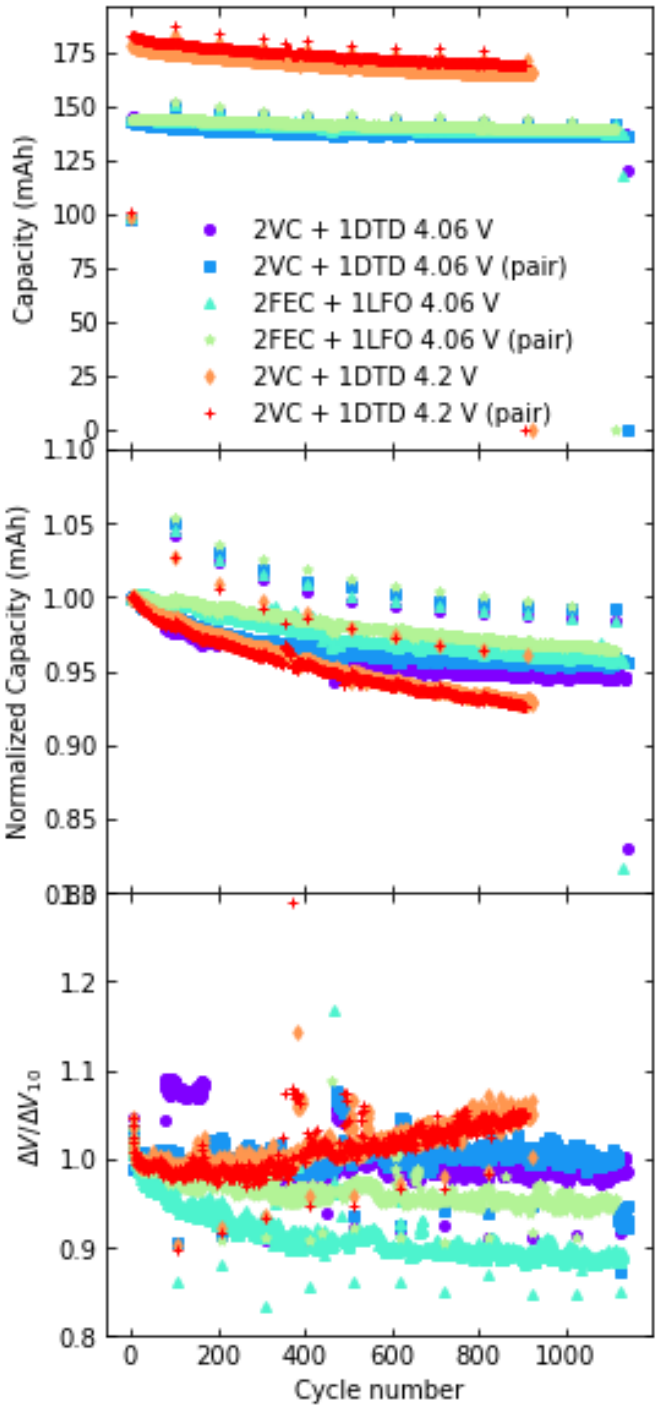
Capacity (mAh)
Normalized Capacity (mAh)
$\Delta V/\Delta V_{10}$
Cycle number
2VC + 1DTD 4.06 V
2VC + 1DTD 4.06 V (pair)
2FEC + 1LFO 4.06 V
2FEC + 1LFO 4.06 V (pair)
2VC + 1DTD 4.2 V
2VC + 1DTD 4.2 V (pair)

The NewareParser object used in this Notebook gives users access to the raw data from every Neware cycler in the Dahn lab. Hopefully the Notebook presented here demonstrated to the reader the flexibility of the API. Of course, Neware is not the only company that makes cyclers; in the Dahn lab, there are cyclers from MACCOR, Moli, NOVONIX, and even custom built ones. The discussion that follows presents the beginnings of work that aims to develop a unified API that handles data files from every cycler in the Dahn lab and a GUI built on top of it, to enable convenient, widespread access. At present, a common data format has been developed, into which raw data from Neware, NOVONIX, and Dal built UHPC systems are translated. All of the functionality presented in the above Jupyter Notebook has been preserved through the transition to this common data format. In fact, additional functionality is currently being developed with the help of undergraduate student John Corsten, along with a web-based GUI. The following discussion uses screen shots from the GUI to facilitate descriptions of new developments and future work.

The GUI that is currently being developed uses a web-based Python framework called Streamlit. This simply means that the GUI runs within an internet browser window, but no internet connection is required. A benefit of this framework is that the GUI is compatible on Windows, Mac, and Linux operating systems. Figure 6.1 shows a snapshot of the browser window a user would see when the GUI is launched. Navigation options show up on the far left, with "File Selection" selected by default. This is where users can load data files. At present, only one cycler data file can be analyzed at a time. Once a data file is loaded, the "Cell Explorer" option in the Navigation bar allows a user to examine, or "explore", the data. Figure 6.2 shows a snapshot where the user would have selected to plot voltage versus capacity for all C/20 cycles. The other quantities plotted in the Jupyter Notebook discussed previously, dQ/dV versus voltage, and ΔV and capacity versus cycle number or time, are accessible via the drop-down bar "What would you like to plot?". Since more than one cycler data file cannot be explored simultaneously, there is at present no capability to create multi-panel figures. This is a feature that is currently under development.

The most significant development thus far enabled by the new cycler data API is differential voltage, dV/dQ, analysis. This is a technique where different cell degradation mechanisms are decoupled. The details of this technique will not be covered here

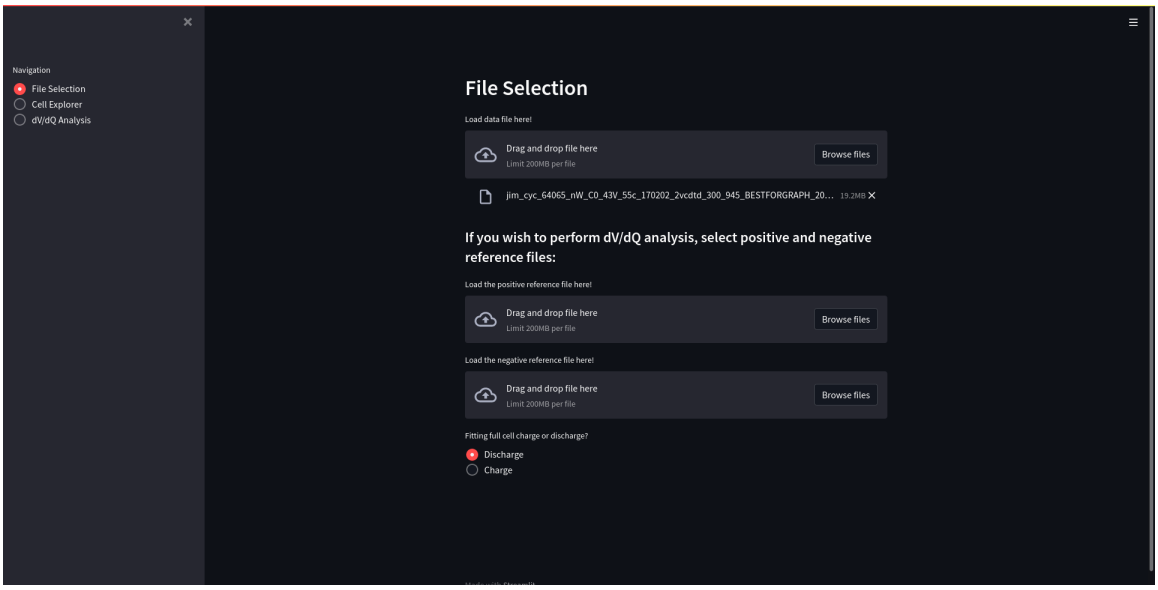

Figure 6.1: A screenshot of the "File Selection" component of the GUI. This is where cycler data files to explore or analyze and reference data used for dV/dQ Analysis are loaded. The parsers developed as part of this thesis are used to read the data into a common format.

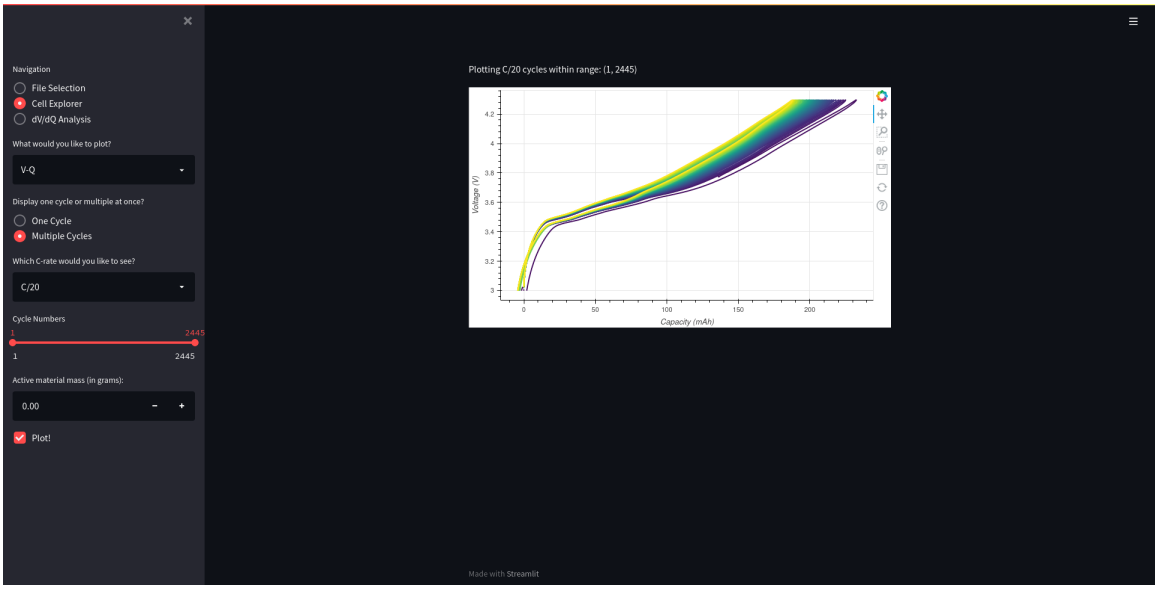

Figure 6.2: A screenshot of the "Cell Explorer" component of the GUI. The Neware data API developed as part of this thesis was modified to accomodate the common data format and is called to explore cell data.

since the goal of this Chapter is to give an overview of the software that has been developed. References [20, 73] discuss this procedure in-depth for the interested reader. It suffices to recognize that dV/dQ analysis has been extensively used in the Dahn lab and in the literature to characterize cell degradation. [4, 11, 13, 27, 34, 35, 63, 78, 79] The general procedure involves numerically fitting the derivative of the voltage versus capacity curve, dV/dQ, to reference data. Typically, this analysis is performed using data from Ultra-high precision coulometry (UHPC) cyclers which are not typically used for long-term cycling. The general procedure for dV/dQ analysis then usually involves putting cells on a UHPC system for a few cycle at the beginning-of-life, switching them to a Neware system for long-term cycling (e.g, 2 years), then moving them back onto a UHPC system for one cycle at the end-of-life. A GUI for performing dV/dQ fitting already exists in the Dahn lab but requires data to be in a column format.

A fellow lab member, Roby Gauthier, developed a brute force approach to dV/dQ fitting on Neware data, saving the transfer to/from a UHPC system.[27] Unfortunately, the workflow was not very transferable to other students; for each cell, a currently existing, separate GUI had to be used to export Neware data into a specific format, then a MATLAB program, without a GUI and little flexibility, had to be run. Instead, the newly developed Neware parser, along with the common data format API, easily enabled the development of a new GUI, that incorporates the features of the existing dV/dQ GUI and the brute force method developed by Roby Gauthier, with the added benefit that data files from both Neware and UHPC systems can be used seamlessly. Researchers can track the dV/dQ parameters as a function of cycle number during long-term cycling, and can additionally compare to the UHPC measurements, if available.

Figure 6.3 shows a snapshot of the new dV/dQ analysis GUI, called DiVAn for "DIfferential Voltage ANalysis" (a divan is a sort of sofa bed; the hope is that this software will help researchers relax!). The displayed graph shows a sample dV/dQ curve from reference data in blue, and the measured dV/dQ curve for a single cycle, not yet fit to the reference data, in red. The left column provides users with manual control over fit parameters, brute force and least squares fitting options, the ability to fit a single cycle or automatically fit all cycles, to specify a capacity range over

which to perform the fits, and data smoothing options. The functionality is extensive and researchers in the Dahn lab are beginning to make use of this wonderful tool. It is interesting how what began as a simple file parser to give researchers more control over data exploration enabled a much larger effort that will hopefully see widespread use, and maybe, just maybe, will facilitate more relaxed research!

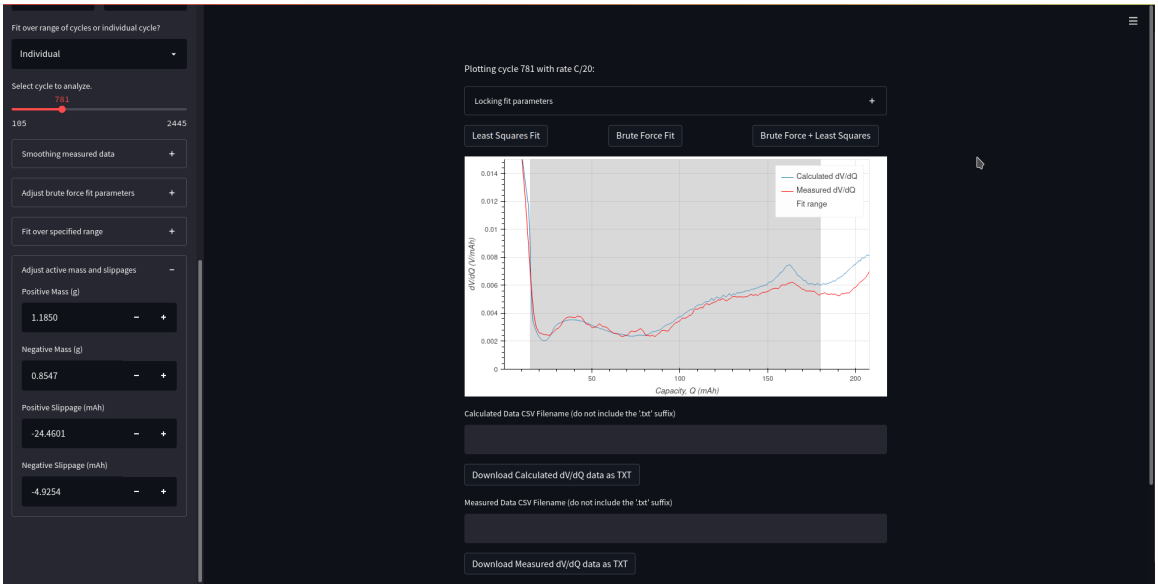

Figure 6.3: A screenshot of the "dV/dQ Analysis" component of the web application. Fitting controls appear on the left side and displayed plots with execution buttons appear in the main screen area. Files to analyze are loaded using the "File Selection" component shown in Figure 6.1.

It is important to emphasize that a dV/dQ fit for a single cycle takes several minutes since some manual work is required to setup initial guesses for the least squares optimization. Even more time is required if a user wishes to fit multiple cycles from long-term cycling data because each cycle to be fit must be extracted manually from the data file. With the new GUI, users need only setup initial guesses and/or a brute-force parameter matrix for the first cycle to be fit, as the optimal parameters returned from a fit a passed as initial guesses for the subsequent fit. This way, hundreds of cycles can be fit in several minutes, saving hours of time!

6.3 Summary of ongoing and future developments

Section 6.1 described the API that enables analysis of AMID measurements. A GUI is currently being developed and will be incorporated within the "Navigation" options of the GUI shown in Figures 6.1-6.3. The general idea is that researchers would have a single GUI that can be used for most common cell analysis tasks. This is only feasible due to the data file parser that works for the various file types from different cyclers.

Of course, there remains unsupported file types, such as from Maccor and Moli cyclers. A high level of priority is currently given to develop parsers that will convert data from those cyclers into the common format, so that users have access to data from all cyclers currently in the Dahn lab.

The "Cell Explorer" component of the GUI is currently quite primitive; it is limited to a single cell at a time and does not have functionality to search for data files. The two primary areas of development here address both of those limitations. Every cycler data file contains a unique barcode identifier that is attached to the cell in question. A search tool where users need only supply this barcode is currently being developed. As a bonus, Streamlit has a way of securely storing user passwords, so, in theory, the GUI could be run locally on personal laptops and users could still have access to the data files stored on the lab server. Lastly, allowing users to load multiple files, create multi-panel graphs, and include data from several cells on the same set of axes are the next most important developments.

Chapter 7

Conclusion

This thesis has been concerned with connecting theory and computation with experiment. The general delineation of ideas have been as follows: Chapter 4 presented a critical analysis on the applicability of the GGA+U approximation for transition metal oxide (TMO) positive electrode materials; Chapter 5 paired computation, theory, and experiment to provide a comprehensive analysis on the role of Co in Ni-rich transition metal oxide positive electrode materials; and Chapter 6 offered an overview of software developed to facilitate and expedite the analysis of experimental data. Maintaining close ties with experiments provided perspective to critically approach computations.

The primary aim of Chapter 4 was to provide a comprehensive analysis of structural, electronic, and electrochemical properties of representative TMO materials with respect to the choice of U in the GGA+U approximation within density functional theory (DFT). [26] GGA+U is by far the most widespread approach to compute TMO positive electrode properties from first principles. However, discussions seldom appear on the potential consequences of the particular choice of U. The hope is that the computations and analyses carried out in this Chapter will serve to increase awareness when choosing U, particularly for TMO materials.

Ni, Co, and Mn containing TMO materials were considered representative materials for positive electrode oxides. Considering both the Li-containing and de-lithiated materials, computation sets were carried out for six structures: (Li)NiO_2 (LNO), (Li)CoO_2 (LCO), and (Li)Mn_2O_4 (LMO). Lattice parameters and TM-O distances were obtained for values of U ranging from 0 to 8 eV in 0.5 eV increments. Electronic structures were analyzed for selected U values by interpreting projected densities of states (pDOS), crystal orbital Hamilton populations (pCOHP), and magnetizations in the context of Ligand Field Theory. [30] The average voltage with respect to Li was computed as a function of U to compare with experiment.

Changes in the electronic structures were correlated with structural and electrochemical variations. Sensitivity to the choice of U depended on the particular occupations of crystal field bands; larger values of U lead to greater spin polarization and, in some cases, changes in TM spin state. As U was increased for Ni in LNO, structural, electronic, and electrochemical properties varied smoothly with no change in TM spin state. The average voltage increased as U increased and $U \sim 6.4$ eV gave best agreement with experiment. However, the resulting ordering of crystal field bands was non-intuitive, perhaps suggesting that agreement with experiment is achieved for the wrong reasons. Changes to TM spin states were observed in $LiCoO_2$, CoO_2, and $LiMn_2O_4$ at particular U values. CoO_2 additionally underwent transitions from metallic to semi-conducting. The sensitivity to the choice of U in (Li)Co_2 suggests that it may not be appropriate for Co in layered oxides.

Performing similar analyses on other TM-containing positive electrode materials, such as $LiFePO_4$ and $LiMnPO_4$, would be valuable to paint a more complete picture. Analyzing properties of mixed-TM materials is more difficult if the TM ordering is not known, nevertheless investigations on how the choice of U may influence properties of materials such as $LiNi_{1/3}Mn_{1/3}Co_{1/3}O_2$ and $LiMn_{3/2}Ni_{1/2}O_4$ could also be useful. Probably the most important next step in this endeavour is to compare the electronic structures obtained with GGA+U to those from methods with higher fidelity, such as the random phase approximation (RPA) or hybrid functionals, for example. This may help better understand the non-intuitive crystal field band orderings and the increasing local spin polarizations with larger U values, providing better understanding on the suitability of the GGA+U approximation for TM-containing positive electrode materials.

In Chapter 5, DFT computations were carried out to understand the role of substituents in Ni-rich layered oxides. This was framed in the context of eliminating Co from these materials due to its high, volatile cost, and human rights issues. The computations did not employ the GGA+U approximation, rather the SCAN+rvv10 exchange and correlation functional. In Chapter 4, structural properties and average voltages were additionally computed using SCAN+rvv10 and acceptable agreement with experiment for the Ni and Mn oxides was achieved, while excellent agreement was obtained for the Co oxide. In retrospect, perhaps adding a small U to SCAN+rvv10

for Ni and Mn would have improved matters. Nevertheless, important conclusions were made from these computations that provided a better understanding of experimental data. Though the first part of Chapter 5 considered thermodynamics, and suggested that Co may be disposed of in Ni-rich layered oxides, a careful examination of kinetics in the latter part of the Chapter revealed the benefits of Co.

Computations on $Li_{1/9}Ni_{0.95}M_{0.05}O_2$ (M = Ni, Mg, Al, Mn, Co) provided insight into how the Li site energy landscape was modified by the various metals considered, in the dilute limit, and how that altered the observed electrochemistry, particularly at high states of charge (low Li content). The influence of the same metals on the O binding energy was also investigated to correlate with the thermal stability of the materials. The results of these computations were used to interpret differences in differential capacities (dQ/dV) and Accelerating Rate Calorimetry (ARC) measurements between each composition. With dilute substitution, it was concluded that Co offers little-to-no benefit to the electrochemical behaviour and thermal stability of LNO.

In order to investigate kinetics, a method to measure the Li-ion chemical diffusion coefficient, D_c, was developed from a reinvented approach. Based on the work of Carslaw and Jaeger [17], and later Atlung, West, and Jacobsen [5], data from a new advanced cell cycling protocol were numerically fit directly to solutions of the phenomenological diffusion equations. The method, dubbed the Atlung Method for Intercalant Diffusion (AMID), was applied to Li-deficient $Li_{1-x}Ni_{1+x}O_2$ ($x = 0, 0.01, 0.02, 0.03, 0.04, 0.05, 0.06$) and Li-rich $Li_{1+x}(Ni_{0.5}Mn_{0.5})_{1-x}O_2$ ($x = 0, 4, 8, 12$) compositions in order to determine how the presence of Ni atoms in the Li layers may hinder Li diffusion. It was found that a $\sim 4\%$ increase in Ni atoms in the Li layers leads to an order of magnitude decrease in D_c. This correlation is invaluable for commercially relevant Ni-rich materials, $LiNi_{0.8}Mn_{0.1}Co_{0.1}O_2$ (NMC811) for example, where the presence of Co reduces the percentage of Ni atoms in the Li layers significantly.

The opposing conclusions in Chapter 5 on whether Co is dispensable in Ni-rich layered oxide positive electrode materials highlight inherent trade-offs in Li-ion battery material optimization. To this end, there are several areas where further work would be beneficial. Comparison of D_c between Li-deficient and Li-rich materials

suggested that the presence of excess Li and/or Mn atoms in the TM layers must provide diffusion enhancing mechanisms. Kinetic Monte Carlo simulations including Li and/or Mn atoms in the TM layers and Ni atoms in the Li layers could provide an atomistic understanding of diffusion pathways that could guide the design of Co-free Ni-rich layered oxides without sacrificing kinetics. The AMID could be applied to many more materials with great interest, however, the particular case of studying changes in D_c as cells age would be of significant benefit. In cases where aged cells have large impedance growth, it is possible that a significant contribution is caused by limited Li-ion diffusion. A thickening surface layer as electrode materials are cycled can have poor Li diffusivity which manifests as increased impedance in the measured data. Accounting for impedance within the AMID fitting procedure would yield more accurate values of D_c, especially in aged cells. Such a study could elucidate degradation mechanisms in Li-ion cells, providing insights that could be directly applied to fast-charge and power delivery protocols within the battery management systems of electric vehicles, for example.

Collaboration between computation and experiment has been an important aspect of the work presented in this thesis. Chapter 6 provided an overview of two software tools that were developed to analyze experimental data. One tool was developed as part of the AMID to automate the analysis of data from an advanced cycler protocol, while the other began as a data file parser to offer researchers more flexibility in visualizing data, but became a necessary building block for developing a new differential voltage analysis (dV/dQ) user interface. Both software tools have saved researchers enormous amounts of time and, in fact, have enabled research that otherwise would have never taken place.

The AMID application programming interface (API) was co-developed with the method itself. Without the software, the analysis would have been so cumbersome that the method would not have been developed — at least not to the extent that it is today. The flexible extraction of data from a rather complex cycler protocol paired with an automated fitting procedure, reduced the analysis time from hours to minutes. This enabled rapid iteration on various aspects of the method that eventually lead to a robust procedure.

The next step in the development of the AMID software is to design a Graphical

User Interface (GUI). Currently, running the software requires each user to install Python and use the API within a Jupyter Notebook. Despite offering a pre-written Notebook template with directions, users without programming experience can still encounter difficulties. The best solution is to have a clickable icon that launches a GUI within which all AMID analysis can be done. The structure of the AMID API is amenable to a GUI, thus using a framework such as Streamlit (this was used for DiVAn) should make this task relatively straightforward. In fact, incorporating an AMID GUI within the same one as DiVAn would give researchers a "one-stop-shop" for all their analysis needs!

The second software component presented in Chapter 6 has at its core a parser and cycler data API that handles various data formats by converting cycler data into a common structure. Currently supported cycler file types are from Neware, NOVONIX, and in-house UHPC systems, while MACCOR and Moli cycler file types are unsupported. The easiest and most obvious next step is to include data files from other cyclers into the parser. This would immediately allow researchers access to data from any cycler currently in the lab, all in one place.

Built on top of the cycler data API is DiVAn and the "Cell Explorer" which both appear within the same GUI. The former enables dV/dQ analysis for any supported cycler data file type. Most of the desired functionality has already been implemented, so the remaining work in this case is mainly to obtain feedback from users in order to improve the user interface. One feature that is not yet implemented but would be of great benefit is the fitting of blended electrodes. The details of dV/dQ analysis are not the subject of this thesis, hence it suffices to mention that analyzing degradation of electrodes with mixed composition requires an adjustment to the numerical fitting procedure. Blended electrode dV/dQ fitting would be a good milestone for DiVAn. The "Cell Explorer" part of the GUI has much more room for improvement. There are three functions that would likely make the software ubiquitous in our lab: searching for cell data files by barcode, loading multiple files, and having control over multi-panel figures. The first feature is already partially implemented and only requires testing. The second feature is already available within the GUI framework but the code needs to be changed to accommodate the data from multiple files. The third feature requires the most work but also has the greatest benefit; the ability to create

multi-panel figures, with flexibility as to which data appear in each panel, could save many hours of work. The current workflow of most lab members involves exporting data to be plotted in a separate program. Exploring data and making decent figures all in one place would certainly help researchers relax, and the software would live up to its name!

Not to undermine the work of Chapter 4, but the most rewarding work presented in this thesis was the fruit of collaboration; from first-principles computations to interpret and guide experiments, to developing a method for measuring Li-ion diffusion by bridging theory and experiment, and, lastly, to developing software that facilitates analysis of experimental data. If nothing else, this thesis should stand as an example of the benefit of collaboration between people of differing skills and qualities.

Bibliography

[1] G. G. Amatucci, J. M. Tarascon, and L. C. Klein. CoO_2, The End Member of the Li_xCoO_2 Solid Solution. *Journal of The Electrochemical Society*, 143(3):1114–1123, 1996.

[2] Ruhul Amin and Yet-Ming Chiang. Characterization of Electronic and Ionic Transport in $Li_{1-x}Ni_{0.33}Mn_{0.33}Co_{0.33}O_2$ (NMC_{333}) and $Li_{1-x}Ni_{0.5}Mn_{0.2}Co_{0.3}O_2$ (NMC_{523}) as a Function of Li Content. *Journal of The Electrochemical Society*, 163(8):A1512–A1517, 2016.

[3] Amnesty International. This is what we die for: Human rights abuses in the democratic republic of the congo power the global trade in cobalt. *AFR 62/3183/2016*, 2016.

[4] Keisuke Ando, Tomoyuki Matsuda, and Daichi Imamura. Degradation diagnosis of lithium-ion batteries with a LiNi0.5Co0.2Mn0.3O2 and LiMn2O4 blended cathode using dV/dQ curve analysis. *Journal of Power Sources*, 390(March):278–285, 2018.

[5] S. Atlung and T. Jacobsen. Dynamic Aspects of Solid Solution Cathodes for Electrochemical Power. *Journal of The Electrochemical Society*, pages 1311–1321, 1979.

[6] Richard F. W. Bader. The zero-flux surface and the topological and quantum definitions of an atom in a molecule. *Theoretical Chemistry Accounts*, 105(4-5):276–283, 2001.

[7] Axel D. Becke. Molecular Bond Energies. *The Journal of chemical physics*, 84(January 1986):4524, 1986.

[8] Axel D. Becke and Erin R. Johnson. A density-functional model of the dispersion interaction. *Journal of Chemical Physics*, 123(15):0–9, 2005.

[9] Axel D. Becke and Erin R. Johnson. Exchange-hole dipole moment and the dispersion interaction. *Journal of Chemical Physics*, 122(15), 2005.

[10] Axel D. Becke and Erin R. Johnson. Exchange-hole dipole moment and the dispersion interaction: High-order dispersion coefficients. *Journal of Chemical Physics*, 124(1), 2006.

[11] Erik Björklund, Chao Xu, Wesley M. Dose, Christopher G. Sole, Pardeep K. Thakur, Tien-Lin Lee, Michael F. L. De Volder, Clare P. Grey, and Robert S. Weatherup. Cycle-Induced Interfacial Degradation and Transition-Metal Cross-Over in $LiNi_{0.8}Mn_{0.1}Co_{0.1}O_2$–Graphite Cells. *Chemistry of Materials*, 34(5):2034–2048, 2022.

[12] P. E. Blöchl. Projector augmented-wave method. *Physical Review B*, 50(24):17953–17979, 1994.

[13] Toby Bond, Roby Gauthier, A. Eldesoky, Jessie Harlow, and J. R. Dahn. In Situ Imaging of Electrode Thickness Growth and Electrolyte Depletion in Single-Crystal vs Polycrystalline $LiNi_xMn_yCo_zO_2$ /Graphite Pouch Cells using Multi-Scale Computed Tomography. *Journal of The Electrochemical Society*, 169(2):020501, 2022.

[14] M. Born and R. Oppenheimer. Zur Quantentheorie der Molekeln. *Annalen der Physik*, 389(20):457–484, 1927.

[15] Ortal Breuer, Arup Chakraborty, Jing Liu, Tatyana Kravchuk, Larisa Burstein, Judith Grinblat, Yaron Kauffman, Alexandr Gladkih, Prasant Nayak, Merav Tsubery, Anatoly I. Frenkel, Michael Talianker, Dan T. Major, Boris Markovsky, and Doron Aurbach. Understanding the Role of Minor Molybdenum Doping in $LiNi_{0.5}Co_{0.2}Mn_{0.3}O_2$ Electrodes: From Structural and Surface Analyses and Theoretical Modeling to Practical Electrochemical Cells. *ACS Applied Materials and Interfaces*, 10(35):29608–29621, 2018.

[16] P. G. Bruce, A. Lisowska-Oleksiak, M. Y. Saidi, and C. A. Vincent. Vacancy diffusion in the intercalation electrode $Li_{1-x}NiO_2$. *Solid State Ionics*, 57(3):353–358, 1992.

[17] H. S. Carslaw and J. C. Jaeger. *Conduction of Heat in Solids*. Oxford at the Clarendon Press, second edition, 1959.

[18] Young-Min Choi, Su-Il Pyun, Joon-Sung Bae, and Seong-In Moon. Effects of lithium content on the electrochemical lithium intercalation reaction into $LiNiO_2$ and $LiCoO_2$ electrodes. *Journal of Power Sources*, 56(1):25–30, 1995.

[19] Marc M. E. Cormier, Ning Zhang, Aaron Liu, Hongyang Li, Julie Inglis, and J. R. Dahn. Impact of Dopants (Al, Mg, Mn, Co) on the Reactivity of Li_xNiO_2 with the Electrolyte of Li-Ion Batteries. *Journal of The Electrochemical Society*, 166(13):A2826–A2833, 2019.

[20] Hannah M. Dahn, A. J. Smith, J. C. Burns, D. A. Stevens, and J. R. Dahn. User-Friendly Differential Voltage Analysis Freeware for the Analysis of Degradation Mechanisms in Li-Ion Batteries. *Journal of The Electrochemical Society*, 159(9):A1405–A1409, 2012.

[21] Lea de Biasi, Alexander Schiele, Maria Roca-Ayats, Grecia Garcia, Torsten Brezesinski, Pascal Hartmann, and Jürgen Janek. Phase Transformation Behavior and Stability of $LiNiO_2$ Cathode Material for Li-Ion Batteries Obtained from In Situ Gas Analysis and Operando X-Ray Diffraction. *ChemSusChem*, 12(10):2240–2250, 2019.

[22] Volker L. Deringer, Andrei L. Tchougréeff, and Richard Dronskowski. Crystal orbital Hamilton population (COHP) analysis as projected from plane-wave basis sets. *Journal of Physical Chemistry A*, 115(21):5461–5466, 2011.

[23] Mudit Dixit, Boris Markovsky, Florian Schipper, Doron Aurbach, and Dan T. Major. Origin of Structural Degradation during Cycling and Low Thermal Stability of Ni-Rich Layered Transition Metal-Based Electrode Materials. *Journal of Physical Chemistry C*, 121(41):22628–22636, 2017.

[24] Marc Doyle, John Newman, and Jan Reimers. A quick method of measuring the capacity versus discharge rate for a dual lithium-ion insertion cell undergoing cycling. *Journal of Power Sources*, 52(2):211–216, 1994.

[25] Richard Dronskowski and Peter E. Blöchl. Crystal orbital hamilton populations (COHP). Energy-resolved visualization of chemical bonding in solids based on density-functional calculations. *Journal of Physical Chemistry*, 97(33):8617–8624, 1993.

[26] S. Dudarev and G. Botton. Electron-energy-loss spectra and the structural stability of nickel oxide: An LSDA+U study. *Physical Review B - Condensed Matter and Materials Physics*, 57(3):1505–1509, 1998.

[27] Roby Gauthier, Aidan Luscombe, Toby Bond, Michael Bauer, Michel Johnson, Jessie Harlow, Alex Louli, and Jeff R Dahn. How do Depth of Discharge, C-rate and Calendar Age Affect Capacity Retention, Impedance Growth, the Electrodes, and the Electrolyte in Li-Ion Cells? *Journal of The Electrochemical Society*, 2022.

[28] Michael J. Gillan, Dario Alfè, and Angelos Michaelides. Perspective: How good is DFT for water? *Journal of Chemical Physics*, 144(13), 2016.

[29] J. E. Greedan, N. P. Raju, A. S. Wills, C. Morin, S. M. Shaw, and J. N. Reimers. Structure and Magnetism in λ-MnO2. Geometric Frustration in a Defect Spinel. *Chemistry of Materials*, 10(10):3058–3067, 1998.

[30] J S Griffith and L E Orgel. Ligand-field Theory. *Quarterly Review, Chemical Society*, (11):381–393, 1957.

[31] Stefan Grimme, Stephan Ehrlich, and Lars Goerigk. Effect of the Damping Function in Dispersion Corrected Density Functional Theory. *Journal of computational chemistry*, 32:1456–1465, 2011.

[32] Joshua Halpern. 3D Representation of Orbitals. In *https://chem.libretexts.org/@go/page/21733*. 2021.

[33] D. R. Hamann, M. Schlüter, and C. Chiang. Norm-Conserving Pseudopotentials. *Physical Review Letters*, 43(20):1494–1497, 1979.

[34] Xuebing Han, Minggao Ouyang, Languang Lu, Jianqiu Li, Yuejiu Zheng, and Zhe Li. A comparative study of commercial lithium ion battery cycle life in electrical vehicle: Aging mechanism identification. *Journal of Power Sources*, 251:38–54, 2014.

[35] J. E. Harlow, D. A. Stevens, J. C. Burns, J. N. Reimers, and J. R. Dahn. Ultra High Precision Study on High Capacity Cells for Large Scale Automotive Application. *Journal of The Electrochemical Society*, 160(11):A2306–A2310, 2013.

[36] Graeme Henkelman, Andri Arnaldsson, and Hannes Jónsson. A fast and robust algorithm for Bader decomposition of charge density. *Computational Materials Science*, 36(3):354–360, 2006.

[37] Roald Hoffmann and William N. Lipscomb. Theory of Polyhedral Molecules III. Population Analyses and Reactivities for the Carboranes. (36):3489, 1962.

[38] P. Hohenberg and W. Kohn. Inhomogeneous Electron Gas. *Phys. Rev.*, 136(3B):B864–B871, 1964.

[39] Timothy Hughbanks and Roald Hoffmann. Chains of Trans-Edge-Sharing Molybdenum Octahedra: Metal-Metal Bonding in Extended Systems. *Journal of the American Chemical Society*, 105(11):3528–3537, 1983.

[40] Anirudha Jena, Po Han Lee, Wei Kong Pang, Kuang Che Hsiao, Vanessa K. Peterson, Tamim Darwish, Nageshwar Yepuri, She Huang Wu, Ho Chang, and Ru Shi Liu. Monitoring the phase evolution in $LiCoO_2$ electrodes during battery cycles using in-situ neutron diffraction technique. *Journal of the Chinese Chemical Society*, 67(3):344–352, 2020.

[41] Kisuk Kang, Ying Shirley Meng, Julien Breger, Clare P. Grey, and Gerbrand Ceder. Electrodes with High Power. *Science*, 311(February):977–980, 2006.

[42] Walter Kohn and L. J. Sham. Self-Consistent Equations Including Exchange and Correlation Effects. *Physical Review Letters*, 140(4A):1133–1138, 1965.

[43] G Kresse and J Furthmiiller. Efficiency of ab-initio total energy calculations for metals and semiconductors using a plane-wave basis set. *Computational Materials Science*, 99(1):16–29, 2007.

[44] G. Kresse and J. Furthmüller. Efficient iterative schemes for ab initio total-energy calculations using a plane-wave basis set. *Physical Review B - Condensed Matter and Materials Physics*, 54(16):11169–11186, 1996.

[45] G. Kresse and J. Hafner. *Ab initio* molecular dynamics for liquid metals. *Physical Review B*, 47(1):558–561, 1993.

[46] G Kresse and D Joubert. From ultrasoft pseudopotentials to the projector augmented-wave method. *Physical Review B*, 59(3):11–19, 1999.

[47] Hongyang Li, Marc Cormier, Ning Zhang, Julie Inglis, Jing Li, and J. R. Dahn. Is Cobalt Needed in Ni-Rich Positive Electrode Materials for Lithium Ion Batteries? *Journal of The Electrochemical Society*, 166(4):A429–A439, 2019.

[48] Hongyang Li, Ning Zhang, Jing Li, and J. R. Dahn. Updating the Structure and Electrochemistry of Li_xNiO_2 for $0 \leq x \leq 1$. *Journal of The Electrochemical Society*, 165(13):A2985–A2993, 2018.

[49] Wu Li, J. N. Reimers, and J. R. Dahn. In situ X-ray diffraction and electrochemical studies of $Li_{1-x}NiO_2$. *Solid State Ionics*, 67:123–130, 1993.

[50] O Limn, E Levi, M D Levi, G Salitra, D Aurbach, R Oesten, U Heider, and L Heider. In situ XRD study of Li deintercalation from two different types of $LiMn_2O_4$. *Solid State Ionics*, 126:109–119, 1999.

[51] Aaron Liu, Nutthaphon Phattharasupakun, Marc M. E. Cormier, Eniko Zsoldos, Ning Zhang, Erin Lyle, Phillip Arab, Montree Sawangphruk, and J. R. Dahn. Factors that Affect Capacity in the Low Voltage Kinetic Hindrance Region of Ni-Rich Positive Electrode Materials and Diffusion Measurements from a Reinvented Approach. *Journal of The Electrochemical Society*, 168(7):070503, 2021.

[52] A. J. Louli, L. D. Ellis, and J. R. Dahn. Operando Pressure Measurements Reveal Solid Electrolyte Interphase Growth to Rank Li-Ion Cell Performance. *Joule*, 3(3):745–761, 2019.

[53] Per Olov Löwdin. On the non-orthogonality problem connected with the use of atomic wave functions in the theory of molecules and crystals. *The Journal of Chemical Physics*, 18(3):365–375, 1950.

[54] D. D. MacNeil and J. R. Dahn. The Reaction of Charged Cathodes with Nonaqueous Solvents and Electrolytes: I. $Li_{0.5}CoO_2$. *Journal of The Electrochemical Society*, 148(11):A1205, 2001.

[55] D. D. MacNeil and J. R. Dahn. The Reaction of Charged Cathodes with Nonaqueous Solvents and Electrolytes: II. $LiMn_2O_4$ charged to 4.2 V. *Journal of The Electrochemical Society*, 148(11):A1211, 2001.

[56] Stefan Maintz, Volker L. Deringer, Andrei L. Tchougréeff, and Richard Dronskowski. Analytic projection from plane-wave and PAW wavefunctions and application to chemical-bonding analysis in solids. *Journal of Computational Chemistry*, 34(29):2557–2567, 2013.

[57] Stefan Maintz, Volker L. Deringer, Andrei L. Tchougréeff, and Richard Dronskowski. LOBSTER: A tool to extract chemical bonding from plane-wave based DFT. *Journal of Computational Chemistry*, 37(11):1030–1035, 2016.

[58] Stefan Maintz, Marc Esser, and Richard Dronskowski. Efficient rotation of local basis functions using real spherical harmonics. *Acta Physica Polonica B*, 47(4):1165–1175, 2016.

[59] L A Montoro, M Abbate, E C Almeida, and J M Rosolen. Electronic structure of the transition metal ions in $LiCoO_2$ $LiNiO_2$ and $LiCo_{0.5}Ni_{0.5}O_2$. *Chemical Physics Letters*, 309(August):1999–2013, 1999.

[60] J.R. Mueller-Neuhaus, R.A. Dunlap, and J.R. Dahn. Understanding Irreversible Capacity in $Li_xNi_{1-y}Fe_yO_2$ Cathode Materials. *Journal of The Electrochemical Society*, 159(7):A924–A928, 2012.

[61] A. Nickol, T. Schied, C. Heubner, M. Schneider, A. Michaelis, M. Bobeth, and G. Cuniberti. GITT Analysis of Lithium Insertion Cathodes for Determining the Lithium Diffusion Coefficient at Low Temperature: Challenges and Pitfalls. *Journal of The Electrochemical Society*, 167(9):090546, 2020.

[62] Tsutomu Ohzuku, Atsushi Ueda, and Masatoshi Nagayama. Electrochemistry and Structural Chemistry of $LiNiO_2$ (R3m) for 4 Volt Secondary Lithium Cells. *Journal of The Electrochemical Society*, 140(7):1862–1870, 1993.

[63] M.R. Palacin and A de Guibert. Why do batteries fail? *Science*, 351(6273), 2016.

[64] M Payne, M Teter, D Allan, T Arias, and J Joannopoulos. Iterative minimisation techniques for ab inito total energy calculations MD and CG. *Reviews of Modern Physics*, 64(4):1045–, 1992.

[65] Haowei Peng, Zeng Hui Yang, John P. Perdew, and Jianwei Sun. Versatile van der Waals density functional based on a meta-generalized gradient approximation. *Physical Review X*, 6(4):1–15, 2016.

[66] Haowei Peng, Zeng-Hui Yang, Jianwei Sun, and John P. Perdew. SCAN+rVV10: A promising van der Waals density functional. pages 1–8, 2015.

[67] John P. Perdew, Kieron Burke, and Matthias Ernzerhof. Generalized Gradient Approximation Made Simple. *Physical Review Letters*, 77(18):3865–3868, 1996.

[68] Nutthaphon Phattharasupakun, Marc M. E. Cormier, Yulong Liu, Chenxi Geng, Eniko Zsoldos, Ines Hamam, Aaron Liu, Michel B. Johnson, Montree Sawangphruk, and J. R. Dahn. A Baseline Kinetic Study of Co-Free Layered $Li_{1+x}(Ni_{0.5}Mn_{0.5})_{1-x}O_2$ Positive Electrode Materials for Lithium-Ion Batteries. *Journal of The Electrochemical Society*, 168(11):110502, 2021.

[69] Nutthaphon Phattharasupakun, Marc Marcel Cormier, Erin Lyle, Eniko Zsoldos, Aaron Liu, Chenxi Geng, Yulong Liu, Hongyang Li, Montree Sawangphruk, and Jeff R Dahn. Correlating Cation Mixing with Li Kinetics: Electrochemical and Li Diffusion Measurements on Li-Deficient $LiNiO_2$ and Li-Excess $LiNi_{0.5}Mn_{0.5}O_2$. *Journal of The Electrochemical Society*, 2021.

[70] R. S. Mulliken. Electronic Population Analysis on LCAO. *J. Chem. Phys*, 23(January 1955):1833, 1955.

[71] Jan N Reimers and J R Dahn. Electrochemical and In-Situ X-Ray Diffraction Studies of Lithium Intercalation in Li_xCoO_2. 139(8), 1992.

[72] Edward Sanville, Steven D. Kenny, Roger Smith, and Graeme Henkelman. Improved Grid-Based Algorithm for Bader Charge Allocation. *Journal of computational chemistry*, 28(5):859–908, 2007.

[73] A. J. Smith, J. C. Burns, and J. R. Dahn. High-precision differential capacity analysis of $LiMn_2O_4$/graphite cells. *Electrochemical and Solid-State Letters*, 14(4):39–42, 2011.

[74] A. J. Smith, J. C. Burns, Xuemei Zhao, Deijun Xiong, and J. R. Dahn. A High Precision Coulometry Study of the SEI Growth in Li/Graphite Cells. *Journal of The Electrochemical Society*, 158(5):A447, 2011.

[75] Wentao Song, Jessie Harlow, Eric Logan, Helena Hebecker, Matthew Coon, Laurent Molino, Michel Johnson, Jeff Dahn, and Michael Metzger. A Systematic Study of Electrolyte Additives in Single Crystal and Bimodal $LiNi_{0.8}Mn_{0.1}Co_{0.1}O_2$ /Graphite Pouch Cells. *Journal of The Electrochemical Society*, 168(9):090503, 2021.

[76] Jianwei Sun, Richard C. Remsing, Yubo Zhang, Zhaoru Sun, Adrienn Ruzsinszky, Haowei Peng, Zenghui Yang, Arpita Paul, Umesh Waghmare, Xifan Wu, Michael L. Klein, and John P. Perdew. Accurate first-principles structures and energies of diversely bonded systems from an efficient density functional. *Nature Chemistry*, 8(9):831–836, 2016.

[77] Jianwei Sun, Adrienn Ruzsinszky, and Johnp Perdew. Strongly Constrained and Appropriately Normed Semilocal Density Functional. *Physical Review Letters*, 115(3):1–6, 2015.

[78] P. Teichert, H. Jahnke, and E. Figgemeier. Degradation Mechanism of Monocrystalline Ni-Rich $Li[Ni_xMn_yCo_z]O_2$ (NMC) Active Material in Lithium Ion Batteries. *Journal of The Electrochemical Society*, 168(9):090532, 2021.

[79] L. M. Thompson, J. E. Harlow, A. Eldesoky, M. K. G. Bauer, J. H. Cheng, W. S. Stone, T. Taskovic, C. R. M. McFarlane, and J. R. Dahn. Study of Electrolyte and Electrode Composition Changes vs Time in Aged Li-Ion Cells. *Journal of The Electrochemical Society*, 168(2):020532, 2021.

[80] A. Van der Ven and G. Ceder. Lithium diffusion mechanisms in layered intercalation compounds. *Journal of Power Sources*, 97-98(December 2000):529–531, 2001.

[81] A. Van der Ven, G. Ceder, M. Asta, and P. D. Tepesch. First-principles theory of ionic diffusion with nondilute carriers. *Physical Review B - Condensed Matter and Materials Physics*, 64(18):1–17, 2001.

[82] Anton Van Der Ven, Jishnu Bhattacharya, and Anna A. Belak. Understanding Li diffusion in Li-intercalation compounds. *Accounts of Chemical Research*, 46(5):1216–1225, 2013.

[83] David Vanderbilt. Soft self-consistent pseudopotentials in a generalized eigenvalue formalism. *Physical Review B*, 41(11):7892–7895, 1990.

[84] Pallavi Verma, Pascal Maire, and Petr Novák. A review of the features and analyses of the solid electrolyte interphase in Li-ion batteries. *Electrochimica Acta*, 55(22):6332–6341, 2010.

[85] Pauli Virtanen, Ralf Gommers, Travis E. Oliphant, Matt Haberland, Tyler Reddy, David Cournapeau, Evgeni Burovski, Pearu Peterson, Warren Weckesser, Jonathan Bright, Stéfan J. van der Walt, Matthew Brett, Joshua Wilson, K. Jarrod Millman, Nikolay Mayorov, Andrew R.J. Nelson, Eric Jones, Robert Kern, Eric Larson, C. J. Carey, İlhan Polat, Yu Feng, Eric W. Moore, Jake VanderPlas, Denis Laxalde, Josef Perktold, Robert Cimrman, Ian Henriksen, E. A. Quintero, Charles R. Harris, Anne M. Archibald, Antônio H. Ribeiro, Fabian Pedregosa, Paul van Mulbregt, Aditya Vijaykumar, Alessandro Pietro Bardelli, Alex Rothberg, Andreas Hilboll, Andreas Kloeckner, Anthony Scopatz, Antony Lee, Ariel Rokem, C. Nathan Woods, Chad Fulton, Charles Masson, Christian Häggström, Clark Fitzgerald, David A. Nicholson, David R. Hagen, Dmitrii V. Pasechnik, Emanuele Olivetti, Eric Martin, Eric Wieser, Fabrice Silva, Felix Lenders, Florian Wilhelm, G. Young, Gavin A. Price, Gert Ludwig Ingold, Gregory E. Allen, Gregory R. Lee, Hervé Audren, Irvin Probst, Jörg P. Dietrich, Jacob Silterra, James T. Webber, Janko Slavič, Joel Nothman, Johannes Buchner, Johannes Kulick, Johannes L. Schönberger, José Vinícius de Miranda Cardoso, Joscha Reimer, Joseph Harrington, Juan Luis Cano Rodríguez, Juan Nunez-Iglesias, Justin Kuczynski, Kevin Tritz, Martin Thoma, Matthew Newville, Matthias Kümmerer, Maximilian Bolingbroke, Michael Tartre, Mikhail Pak, Nathaniel J. Smith, Nikolai Nowaczyk, Nikolay Shebanov, Oleksandr Pavlyk, Per A. Brodtkorb, Perry Lee, Robert T. McGibbon, Roman Feldbauer, Sam Lewis, Sam Tygier, Scott Sievert, Sebastiano Vigna, Stefan Peterson, Surhud More, Tadeusz Pudlik, Takuya Oshima, Thomas J. Pingel, Thomas P. Robitaille, Thomas Spura, Thouis R. Jones, Tim Cera, Tim Leslie, Tiziano Zito, Tom Krauss, Utkarsh Upadhyay, Yaroslav O. Halchenko, and Yoshiki Vázquez-Baeza. SciPy 1.0: fundamental algorithms for scientific computing in Python. *Nature Methods*, 17(3):261–272, 2020.

[86] Lei Wang, Thomas Maxisch, and Gerbrand Ceder. Oxidation energies of transition metal oxides within the GGA+U framework. *Physical Review B - Condensed Matter and Materials Physics*, 73(19):1–6, 2006.

[87] Luning Wang, Anjali Menakath, Fudong Han, Yi Wang, Peter Y. Zavalij, Karen J. Gaskell, Oleg Borodin, Dinu Iuga, Steven P. Brown, Chunsheng Wang, Kang Xu, and Bryan W. Eichhorn. Identifying the components of the solid–electrolyte interphase in Li-ion batteries. *Nature Chemistry*, 11(9):789–796, 2019.

[88] Min Yu and Dallas R. Trinkle. Accurate and efficient algorithm for Bader charge integration. *Journal of Chemical Physics*, 134(6), 2011.

[89] Ning Zhang, Jing Li, Hongyang Li, Aaron Liu, Que Huang, Lin Ma, Ying Li, and Jeff R. Dahn. Structural, Electrochemical, and Thermal Properties of Nickel-Rich $LiNi_xMn_yCo_zO_2$ Materials. *Chemistry of Materials*, 30(24):8852–8860, 2018.